Master's thesis
Theoretical physics

Non-thermal dark matter from particle decays

Kalle Ala-Mattinen
2018

Advisors: Kimmo Tuominen
Matti Heikinheimo
Examiners: Kari Rummukainen
Matti Heikinheimo

UNIVERSITY OF HELSINKI
DEPARTMENT OF PHYSICS

PL 64 (Gustaf Hällströmin katu 2)
00014 University of Helsinki

HELSINGIN YLIOPISTO — HELSINGFORS UNIVERSITET — UNIVERSITY OF HELSINKI

Tiedekunta/Osasto — Fakultet/Sektion — Faculty	Laitos — Institution — Department
Faculty of Science	Department of Physics

Tekijä — Författare — Author
Kalle Ala-Mattinen

Työn nimi — Arbetets titel — Title

Non-thermal dark matter from particle decays

Oppiaine — Läroämne — Subject
Theoretical physics

Työn laji — Arbetets art — Level	Aika — Datum — Month and year	Sivumäärä — Sidoantal — Number of pages
Master's thesis	February 2018	84

Tiivistelmä — Referat — Abstract

We investigate a dark sector augmentation of the standard model with a keV-scale right-handed sterile neutrino field N and a TeV-scale singlet scalar field S. The ("warm") dark matter candidate of the model is the sterile neutrino, which is produced from decays of singlet scalars. The dark sector is coupled to the standard model via the Higgs portal coupling between the singlet scalar and Higgs H. The momentum distribution function, which contains the full information about the production process, is obtained for sterile neutrinos by solving a system of Boltzmann equations. For simplicity, we assume the effective number of relativistic degrees of freedom to be constant during the dark matter production. We take into account several constraints from structure formation and cosmology, and find that even this simple model gives rise to a rich phenomenology. In particular, we find that, in addition to offering a realistic dark matter candidate, the sterile neutrino can attain a highly non-thermal momentum distribution in the process. A direct consequence of this is the inability to assess the impact on the structure formation with the usual estimators that require a thermal momentum distribution, such as the free-streaming length. We rely on [72], which uses the linear power spectrum, instead of the free-streaming length, to estimate the impact on structure formation. This method also works for non-thermal momentum spectra. On the side, we discuss the evidence for dark matter, known problems of the ΛCDM, and the basic production mechanisms in the early universe. Also a comprehensive, analytical and numerical, reduction of necessary equations is presented.

Avainsanat — Nyckelord — Keywords
dark matter, warm dark matter, FIMP, WIMP, sterile neutrino, Higgs portal

Säilytyspaikka — Förvaringsställe — Where deposited

Muita tietoja — övriga uppgifter — Additional information

Contents

Chapter 1

INTRODUCTION

Throughout its known history, the universe has been expanding – and still is. This dynamical nature of the universe is the cornerstone of the modern cosmology alongside the general theory of relativity, which enabled a mathematically consistent way to model the universe. But to use general relativity in cosmology, several assumptions are needed - assumptions that will fix the equations to fit to our observed universe. This chapter gives a quick recap of these assumptions and their consequences.

1.1 Standard cosmology: FLRW-universe

The simplest way to formulate general relativity is by the action principle[1]. This was first done by David Hilbert in 1915 and is thus known as the Hilbert action [1]

$$S = \frac{1}{16\pi G} S_{\mathrm{H}} + S_{\mathrm{M}} = \int \mathrm{d}^4x \sqrt{-g} \left(\frac{R}{16\pi G} + \mathcal{L}_{\mathrm{M}} \right), \tag{1.1.1}$$

where we have already included the action for the matter S_{M} and farsightedly chosen a suitable normalisation for the Hilbert action S_{H}. In above equation $g_{\mu\nu}$ is the metric tensor and $g \equiv \det(g_{\mu\nu})$, R is the Ricci scalar, G is the Newton's gravitational constant and $\mathcal{L}_{\mathrm{M}}$ is the Lagrangian (density) of the matter fields of the universe.

Einstein's field equations are obtained by varying the action with respect to the metric $g_{\mu\nu}$, resulting in

$$R_{\mu\nu} - \frac{1}{2} R\, g_{\mu\nu} = 8\pi G\, T_{\mu\nu}\,, \tag{1.1.2}$$

where $R_{\mu\nu}$ is the Ricci tensor and the energy-momentum tensor $T_{\mu\nu}$ is defined from the variation of the matter part of the action as

$$T_{\mu\nu} \equiv -2 \frac{1}{\sqrt{-g}} \frac{\delta S_{\mathrm{M}}}{\delta g^{\mu\nu}}\,. \tag{1.1.3}$$

[1] This section closely follows the book by S. Carroll [1].

The Einstein's field equations govern how the metric responds to energy and momentum [1], but also determine the metric. But before going any further, we simplify the metric by taking into account its symmetries.

Models based upon the assumptions that the metric is spatially homogeneous and isotropic are called Friedmann-Lemaître-Robertson-Walker (FLRW) models and are a good approximation of the universe at cosmologically large scales [1,2]. This assumption embodies the fact that each point and direction in the universe looks the same spatially, but not temporally – as we know that the early universe has been hot and dense whereas now it is quite the opposite. Now the non-homogeneity of the time coordinate manifests itself as a universal scale factor $a(t)$ which tells how the different time-slices of homogeneous and isotropic universe are related to each other[2]. The metric of the FLRW model is called the Roberson-Walker (RW) metric, and it takes the form [3]

$$ds^2 = dt^2 - a(t)^2 \left(\frac{dr^2}{1 - Kr^2} + r^2 d\theta^2 + r^2 \sin^2 \theta d\phi^2 \right), \tag{1.1.4}$$

where $a(t)$ is the aforementioned scale factor and K is a parameter describing the spatial curvature. With an appropriate rescaling of the coordinates, K can be chosen to be $+1$ -1, or 0 corresponding to positive (open), negative (closed) or zero (flat) spatial curvature (universe) respectively [1,3].

Inserting the RW metric into the Einstein's equation (1.1.2) and assuming the energy-momentum tensor to take the form of the perfect fluid $T^{\mu}{}_{\nu} = \mathrm{diag}(-\rho, p, p, p)$, we get the Friedmann equations which govern the evolution of $a(t)$ [1]

$$\left(\frac{\dot{a}}{a}\right)^2 = \frac{8\pi G}{3}\rho - \frac{K}{a^2}, \qquad \frac{\ddot{a}}{a} = -\frac{4\pi G}{3}(\rho + 3p), \tag{1.1.5}$$

where ρ and p are, respectively, the energy density and the pressure of the perfect fluid and K is already assumed to be rescaled to get values $+1$, -1 or 0. The conservation of energy and the momentum then translates into the energy continuity equation

$$\frac{\dot{\rho}}{\rho} = -3(1 + \frac{p}{\rho})\frac{\dot{a}}{a}, \tag{1.1.6}$$

which can be solved from the Friedmann equations or straight away from the conservation of energy-momentum tensor by requiring $\nabla_{\mu} T^{\mu}{}_{0} = 0$.

As in any fluid dynamical system, we then need to impose an equation of state which tells how the pressure and the energy density of the fluid are correlated. Usually in cosmology a simple equation of state (compare to ideal gas law) is sufficient [1]

$$p = w\rho, \tag{1.1.7}$$

[2]In other words, how the maximally symmetric spatial bit of the metric at constant time t_0 is related to another maximally symmetric spatial bit of the metric at time $t_0 + \Delta t$. So the scale factor $a(t)$ can be thought of as an effective measure of time.

where $w = p/\rho$ is taken to be a constant parameter. Now the energy continuity equation can be solved to relate the energy density and the scale factor

$$\rho \sim a^{-3(1+w)} \,. \tag{1.1.8}$$

The energy content of the universe is formed by the matter, radiation and vacuum energy it contains. By matter we mean any non-relativistic matter component and by radiation any ultra-relativistic ($E \gg m$) matter component. Vacuum energy, or the cosmological constant, acts as a negative pressure and is responsible of the observed accelerating expansion of the universe. While this explains the current observations, not much more about the vacuum energy is known.

Matter, being non-relativistic, has $p \ll \rho$ so its pressure can be neglected resulting in $w = 0$. Hence the energy density of matter falls off as the universe expands $\rho_m \sim a^{-3}$. This is the consequence of each spatial dimension expanding by a factor of a so that the number density of the matter decreases as the new volume. Radiation on the other hand also possess a wavelength which, in addition to its decrease in number density as the universe expands, can red-shift. Hence the energy density of radiation falls like $\rho_r \sim a^{-4}$ resulting in $w = 1/3$. A constant vacuum energy $\rho_{\text{vac}} \sim a^0$, resulting in $w = -1$, is consistent with the current observations [2].

The basic observable quantity in cosmology is the expansion rate of the universe known as the Hubble parameter $H \equiv \dot{a}/a$. The present value of the Hubble parameter $H(t_0) \equiv H_0$ is called the Hubble constant and the strictest value of it has been determined indirectly by the Planck satellite $H_0 = 67.8 \pm 0.9\,\text{km/s/Mpc}$ [4]. Similar, but less strict, value was obtained from the recent observations of gravitational waves (standard sirens) $H_0 = 70.0^{+12.0}_{-8.0}\,\text{km/s/Mpc}$ [5] while the value obtained by using the cosmic distance ladder is $H_0 = 73.24 \pm 1.74\,\text{km/s/Mpc}$ [6]. The tension between the Planck and the cosmic distance ladder results (see Fig. 1.1) is hoped to be resolved as more standard siren data is gathered. Furthermore, as the standard siren measurements are independent of the expansion history of the universe while the Planck data does depend on the expansion history, thus their concordance measures the goodness of the ΛCDM model used in Planck data analysis. Due to experimental uncertainty, the Hubble parameter is often given as $H_0 = 100h\,\text{km/s/Mpc}$, where the scaled observable h is typically $h \approx 0.7$.

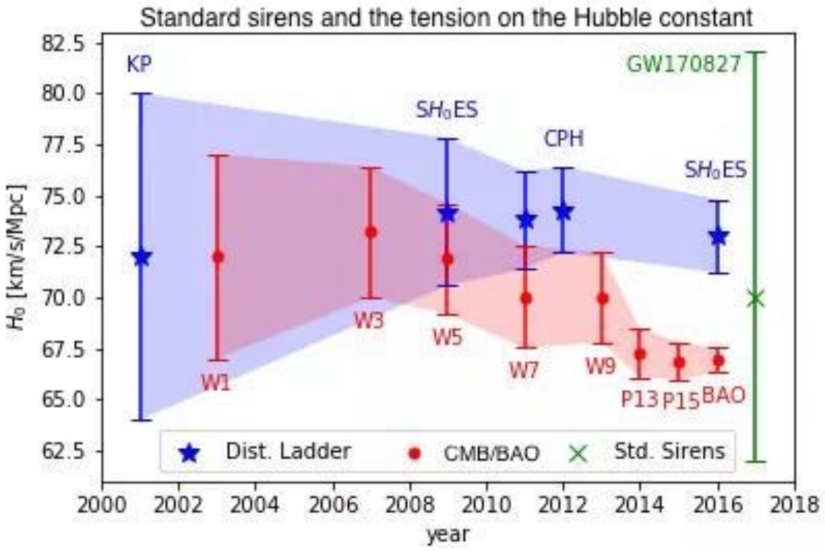

Figure 1.1: Determination of the Hubble constant from the cosmic microwave background (red), cosmic distance ladder (blue) and gravitational standard siren (green). Figure from [7].

Another feature of interest the spatial curvature of our universe, i.e. the parameter K in the equation (1.1.5). For this purpose, we define the critical energy density $\rho_{\text{crit}} \equiv \frac{3H^2}{8\pi G}$ as the total amount of energy density needed for universe to be flat. This is evident from the first Friedmann's equation in (1.1.5). Furthermore, we define the density parameter $\Omega \equiv \frac{\rho}{\rho_{\text{crit}}}$, which now allows us to write the first Friedmann's equation as

$$\Omega - 1 = \frac{K}{H^2 a^2} \,. \tag{1.1.9}$$

The universe is then flat, open or closed if, respectively, Ω is 1, less than 1 or larger than 1. The Planck collaboration has determined, with a good accuracy, the universe to be flat, i.e. they obtained $|\Omega_{\text{K}}| < 0.005$ [4], where $|\Omega_{\text{K}}| \equiv |\Omega - 1|$.

This model, where the universe is spatially homogeneous, isotropic and flat, is called the ΛCDM model, or the standard model of cosmology. Its name derives from its prediction of the existence of vacuum expectation value, or dark energy, and cold dark matter, which are abbreviated as Λ and CDM respectively. Despite the simplicity of the model, it gives a good narrative about the formation of the cosmic microwave background, the large-scale structure of the universe, primordial abundances of light elements (^{2}H, ^{3}He, ^{4}He, ^{7}Li) and the accelerating expansion of the universe. While doing so, the ΛCDM model also fits reasonably well to all cosmological observations.

1.2 Equilibrium thermodynamics

In addition to being homogeneous, the early universe was also hot and dense so that the standard model fields were in thermodynamical equilibrium with each other. This

equilibrium is well manifested by the spectrum of the cosmic microwave background (CMB) resembling the perfect blackbody distribution.

In thermodynamical equilibrium the distribution function can be written as [3]

$$f(\mathbf{p}) = \frac{1}{e^{(E-\mu)/T} \pm 1}\,, \tag{1.2.1}$$

where $+$ $(-)$ is for fermions (bosons), $E^2 = |\mathbf{p}|^2 + m^2$ is the energy of the particle and μ and T are the chemical potential and the temperature, respectively.

For a gas of particles with g internal degrees of freedom (DOF), the number density n, energy density ρ and pressure p are given in terms of the distribution function as

$$n = \frac{g}{(2\pi)^3}\int f(\mathbf{p})\,\mathrm{d}^3p\,, \tag{1.2.2}$$

$$\rho = \frac{g}{(2\pi)^3}\int E(\mathbf{p}) f(\mathbf{p})\,\mathrm{d}^3p\,, \tag{1.2.3}$$

$$p = \frac{g}{(2\pi)^3}\int \frac{|\mathbf{p}|^2}{3E} f(\mathbf{p})\,\mathrm{d}^3p\,. \tag{1.2.4}$$

Since the universe is not static, its local thermal equilibrium at one moment is not necessarily maintained to a later moment. This depends on the rate of expansion H and the rate of interactions Γ that keep the system equilibrated. If the time scale of interactions is much smaller than the time scale of expansion

$$t_\Gamma \equiv \frac{1}{\Gamma} \ll t_H \equiv \frac{1}{H}\,, \tag{1.2.5}$$

the local equilibrium is always reached before the expansion has had time to depart the system from it.

In the early universe particle species were relativistic, so the energy density is obtained from Eq. (1.2.3) to be

$$\rho(T) = \frac{\pi^2}{30} g_*(T) T^4\,, \tag{1.2.6}$$

where the effective number of degrees of freedom for energy density is

$$g_*(T) = \sum_{\text{bosons}} g_i \left(\frac{T_i}{T}\right)^4 + \frac{7}{8}\sum_{\text{fermions}} g_i \left(\frac{T_i}{T}\right)^4\,. \tag{1.2.7}$$

The entropy density $s \equiv S/V$ is obtained from $E = TS - pV + \sum \mu_i N_i$ to be

$$s = \frac{\rho + p}{T}\,, \tag{1.2.8}$$

where we used $|\mu|_i \ll T$. For relativistic particles the entropy density becomes

$$s(T) = \frac{2\pi^2}{45} g_{*s}(T) T^3\,, \tag{1.2.9}$$

where the effective number of degrees of freedom for entropy density is

$$g_{*s}(T) = \sum_{\text{bosons}} g_i \left(\frac{T_i}{T}\right)^3 + \frac{7}{8}\sum_{\text{fermions}} g_i \left(\frac{T_i}{T}\right)^3\,. \tag{1.2.10}$$

In the equations (1.2.7) and (1.2.10) we have explicitly shown the kinetic temperatures T_i of each relativistic particle species and T denotes temperature of those species in the thermal equilibrium. In the case of all species sharing the same temperature and the equation of state $p \approx \frac{1}{3}\rho$ holds, we have $g_* \approx g_{*s}$.

1.3 The standard model of particle physics

The standard model (SM) is a quantum field theory describing the strong, weak and electromagnetic interactions. A quantum field theory is specified by its Lagrangian density which encodes the field content and the symmetries of the theory. Interactions between the fields can be determined from the Lagrangian density, and are usually represented graphically as Feynman diagrams. This section presents an auxiliary overview of the structure of the SM. For more discussion about the symmetries, field content and interactions in the SM, see [2, 9, 10].

Besides the Poincaré group, the standard model is invariant under the gauge group $SU(3)_{\mathrm{C}} \times SU(2)_{\mathrm{L}} \times U(1)_{\mathrm{Y}}$. The factor $SU(3)_{\mathrm{C}}$ describes the strong interactions between the quarks and the eight gluons, where the latter are the gauge boson of this gauge group. The electromagnetic and the weak interactions are combined with the electroweak interactions described by the $SU(2)_{\mathrm{L}} \times U(1)_{\mathrm{Y}}$ gauge interactions, affecting leptons and quarks, and mediated by the gauge bosons $W^{\pm}, Z$ and γ. All SM particles, except for the photon, the neutrinos and the gluons, gain non-zero masses because $SU(2)_{\mathrm{L}} \times U(1)_{\mathrm{Y}}$ is spontaneously broken to $U(1)_{\mathrm{em}}$. This symmetry breaking is induced by the Higgs boson, which is the only elementary scalar in the theory. Most notably, this results in non-zero masses for the gauge bosons $W^{\pm}, Z$. Despite the fact that baryons are particles made up of three quarks, in the cosmological context the standard model particles are collectively referred to as "baryonic matter".

The standard model does not contain gravity, dark matter nor neutrino masses. Furthermore, it does not account for the observed baryon asymmetry nor the accelerating expansion of the universe.

1.4 Summary of the chapter

In this chapter we have introduced the mathematical framework underlying the following chapters. We described the derivation and the assumptions of the Friedmann's equations and discussed the main observable quantities related to it, namely the Hubble constant H_0 and the spatial curvature K. In passing, we mentioned the known tension in the observational value of the Hubble constant. The first section of the chapter was concluded by gathering the previous assumptions along with observed quantities under the single model called ΛCDM. The second section covers the basics of equilibrium thermodynamics needed in the following chapters. In the last section of the

chapter the standard model of particle physics is shortly described, as it is the model on top of which the dark matter physics in the following chapters is built on.

Chapter 2

DARK MATTER

All cosmological evidence seems to point to the existence of much more mass in the universe than the standard model of the particle physics can account for. The Planck satellite has observed the dark matter energy density to be $\Omega_{\rm DM}h^2 = 0.1188 \pm 0.0010$ [4] while the energy density of baryonic matter is $\Omega_{\rm b}h^2 = 0.02230 \pm 0.00014$ [4], making dark matter contribution to be over five times that of baryonic matter.

The dark matter particle, beyond the standard model, is the most promising and the most tested explanation for this missing mass problem. To seek this elusive unknown particle with the ever-diminishing parameter spaces would be absurd if not for high degree of observational evidence in its favour. For this reason yet another framework for dark matter particle is considered in this work. To summarise the presumed nature of the dark matter let us make the following dark matter hypothesis:

Dark Matter hypothesis. *There exists a new particle that is:*

1) Non-luminous (uncharged under electromagnetic force $U(1)_{\rm Y}$.

2) Non-relativistic at the time of structure formation.

3) Weakly (feebly)-interacting with the visible matter.

4) Stable on cosmological time scales.

Although the evidence for DM is compelling, the direct signal has not been observed, and this leaves room for speculation about the correctness of the dark matter hypothesis. The current runner-up is (some variation) of modified gravity. While the modification of gravity could explain some observations, it is unable to account for the observed Cosmic Microwave Background (CMB) power spectrum in early universe.

2.1 Evidence for dark matter

There exists a compelling amount of evidence supporting the DM hypothesis. This includes measurements from cosmologically small to large scales. The most important

piece of evidence comes from the early universe, namely the CMB power spectrum. Also an equally important evidence is the observed mass distribution of galaxy cluster mergers. These two observational evidence are hard to explain with the framework of modified gravity, but emerge naturally from the framework of particle dark matter.

2.1.1 Rotation curves

Among the first evidence of DM were the rotation curves of various galaxies [8, and references therein]. The rotation velocity of galaxy depends on its mass distribution so, by observing the rotation curve, the mass of the galaxy can be constrained.

An example of a rotation curve is given in the figure Fig. 2.1, where the amount of luminous matter within the galaxy is approximately known from telescope surveys. By using newtonian dynamics, we can solve the resulting rotation curve, which give the dashed line in Fig. 2.1. As expected, further away from the centre we are, the less mass there is, and $M(r)$ decreases, and hence $v(r)^2 \sim M(r)/r$ decreases. But when we measure the rotation velocity of the galaxy and plot it along with the predicted luminous curve, we find that as the radius r grows the rotation velocity $v(r)^2$ seems to approach a constant. The evident discrepancy between the predicted and observed curves cannot even be accounted for the addition of faint gas within the galaxy (dotted line in Fig. 2.1). This clearly speaks for the existence of a non-luminous matter component and, in fact, if we assume presence of a spherical dark matter halo around the spiral galaxy, we get the dash-dot line of Fig. 2.1. Fitting all three components together then gives the solid line which agrees well with observations. From this we conclude that galaxies are embedded in a halo of dark matter. Furthermore, let the mass distribution of dark matter scale as $\rho(r) \sim r^n$ at large radii, leading to additional mass contribution $m_{\mathrm{DM}}(r) = \int_V \rho(r)\mathrm{d}V \sim r^{n+3}$. Then $v(r)^2 \sim m_{\mathrm{DM}}(r)/r \sim r^{n+2}$ suggests that a constant value at large radii is reached if the dark matter halo's mass distribution scales as r^{-2} at large radii.

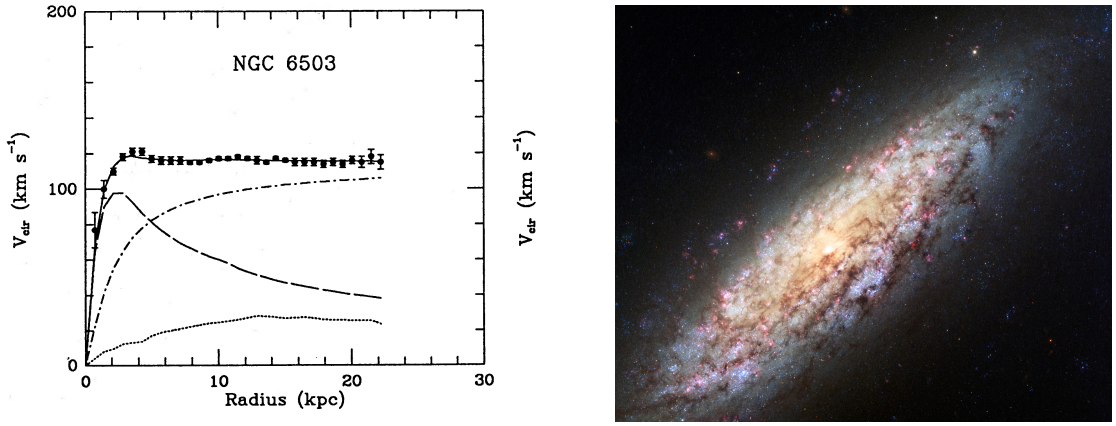

Figure 2.1: **Left panel**: Rotation curve of individual components of mass for dwarf spiral galaxy NGC 6503. The dashed curve accounts the luminous matter, the dotted curve is for the gas (not necessarily visible) present in the galaxy and the dash-dot curve comes by assuming the a dark matted halo around the spiral galaxy. Solid curve is the fitted result of the previous ones. Figure from [11]. **Right panel**: Hubble Space Telescope image of the spiral galaxy NGC 6503. Figure by NASA & ESA.

2.1.2 Galaxy cluster surveys

The more modern way to determine the amount of mass within e.g. galaxy clusters is by gravitational lensing [12]. The effect of lensing is caused by a mass curving space-time and thus bending the geodesics on which light propagates (see Fig. 2.2). From this bending of light rays we can accurately figure out the total mass of the lens. Surveys that probe masses of galaxy clusters this way consistently find much more mass than what can be accounted for by luminous matter [13–15].

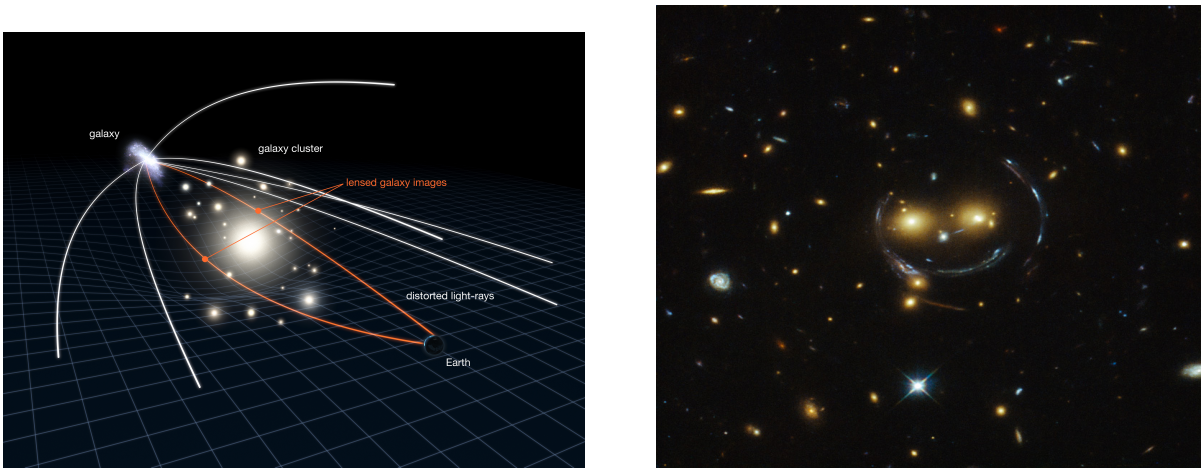

Figure 2.2: **Left panel**: an illustration of the concept of gravitational lensing. Figure by NASA, ESA & L. Calçada. **Right panel**: lensing effect seen by the Hubble Space Telescope. The two yellow galaxies in the middle are SDSSCGB 8842.3 and SDSSCGB 8842.4 and the arcs around them are caused by the strong gravitational lensing effect. Figure by NASA & ESA.

2.1.3 Galaxy mergers

One of the most intriguing pieces of evidence[1] for dark matter comes from galaxy mergers, which are intense collisions of two galaxy clusters. They are among the most energetic events in the universe with the highest shock velocities measured at $\sim 4500\,\mathrm{kms}^{-1}$ [39]. The shock velocities that high can be produced even if the infall velocity of the mass centroid is only $\sim 2600\,\mathrm{kms}^{-1}$ [40]. The Fig. 2.3 shows a particular galaxy merger known as the *bullet cluster*. It its evident that most of the luminous matter lies in the middle of the bullet cluster, still going through the collision process, whereas most of the mass of the bullet cluster is offset from the luminous matter lying in the outer regions of the newly formed cluster. This infers to a conclusion that the dark matter haloes of the initial clusters have passed through each others and the luminous matter without experiencing much of the ram pressure. The luminous matter, on the other hand, is left behind due to the drag of the ram pressure of oncoming luminous matter. For this to happen, the interactions of dark matter with itself and the luminous matter must be sufficiently weak.

[1] Although the galaxy mergers seem like adamant evidence for the existence of dark matter particles, they have also been used as evidence *against* the particle dark matter hypothesis. This will be discussed in more detail in Chapter 2.2.4.

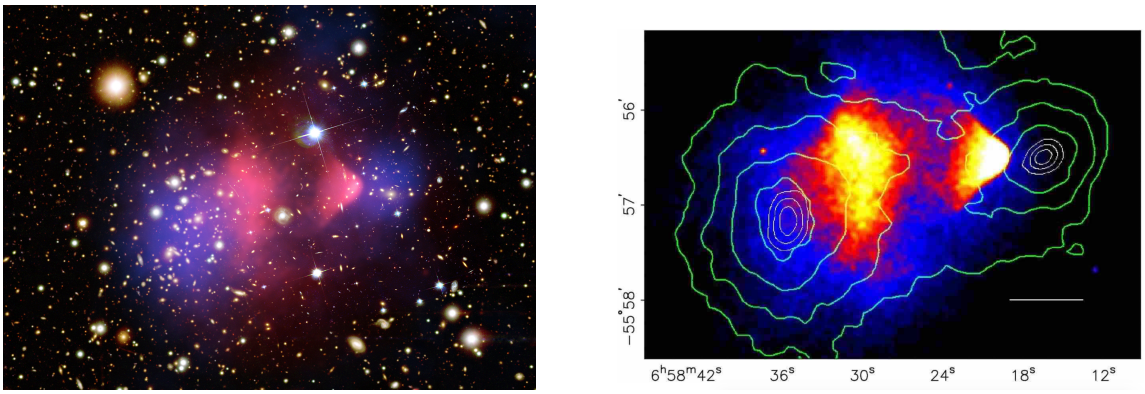

Figure 2.3: On the left: Multichannel composition image of galaxy cluster 1E 0657-556. Optical data showing stars and galaxies, X-ray data showing the distribution of hot gas coloured red, and gravitational lensing data showing the mass distribution coloured blue. Figure by NASA[2]. On the right: essentially the same image but now showing only the colour-coded X-ray intensity and a map of gravitational convergence from gravitational lensing. Figure from [15].

2.1.4 CMB temperature fluctuations

The cosmic microwave background offers a snapshot of the universe at the time of recombination i.e. when the photons could finally stream freely. The CMB pattern depends on the energy content of the universe at that moment and is seen to be isotropic to a high degree, see Fig. 2.4. From the small anisotropies in CMB we can deduce the energy content of the universe. More precisely, these anisotropies constrain the form of the angular power spectrum (see Fig. 2.5) in a way that depends discreetly on the magnitude of various energy densities in the universe. From the observed angular power spectrum, Fig. 2.6, the energy density of dark matter has been measured to be $\Omega_{\mathrm{DM}}h^2 = 0.1188 \pm 0.0010$ [4] and the energy density of baryonic matter to be $\Omega_{\mathrm{b}}h^2 = 0.02230 \pm 0.00014$ [4]. Thus, because $\Omega_{\mathrm{DM}}/\Omega_{\mathrm{b}} \approx 5.33$, there is over five times more dark matter than baryonic matter in the universe.

[2]**X-ray:** NASA/CXC/M.Markevitch et al.; **Optical:** NASA/STScI; Magellan/U.Arizona/D.Clowe et al.; **Lensing Map:** NASA/STScI; ESO WFI; Magellan/U.Arizona/D.Clowe et al.

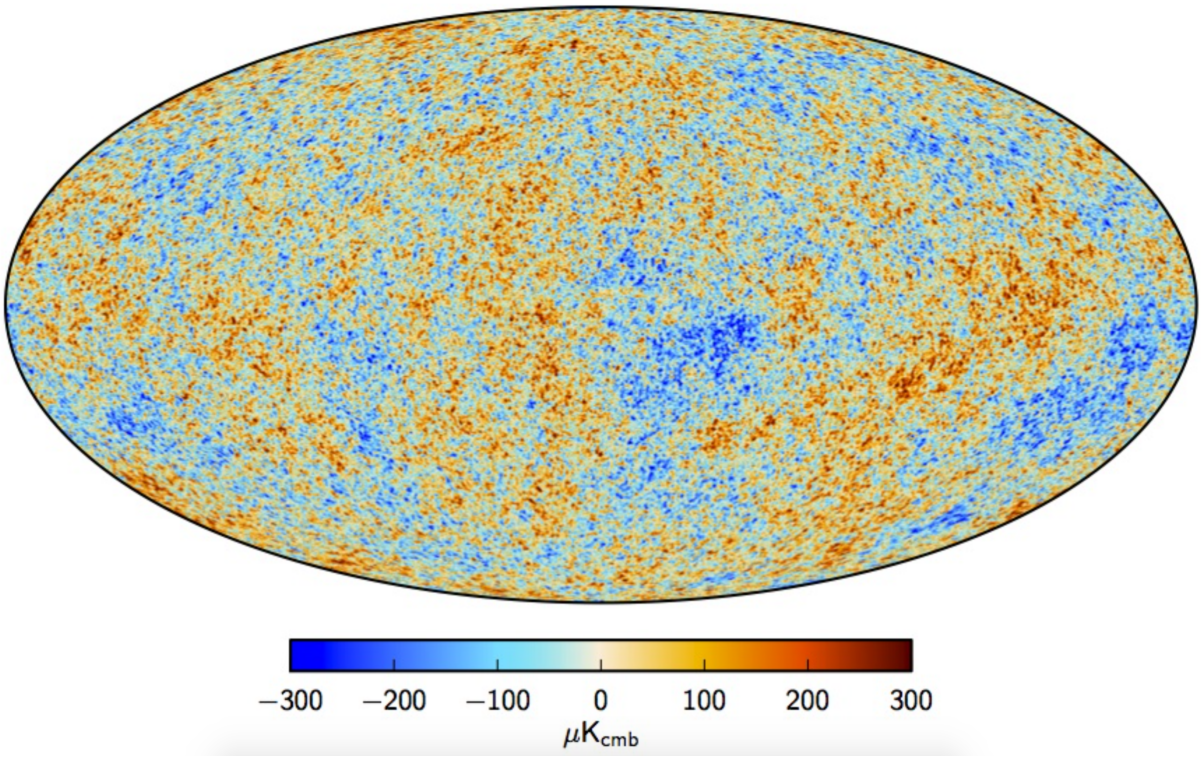

Figure 2.4: Anisotropy map of the CMB. The figure shows the temperature fluctuations around the mean temperature of the whole sky. The galactic foreground and its dipole caused by motion of our Local Group with respect Hubble flow have been subtracted. A small strip of the galactic plane, 1.6% of the sky in the centre, is filled in by a constrained realisation that has the same statistical properties as the rest of the sky. Figure by ESA/Planck Collaboration.

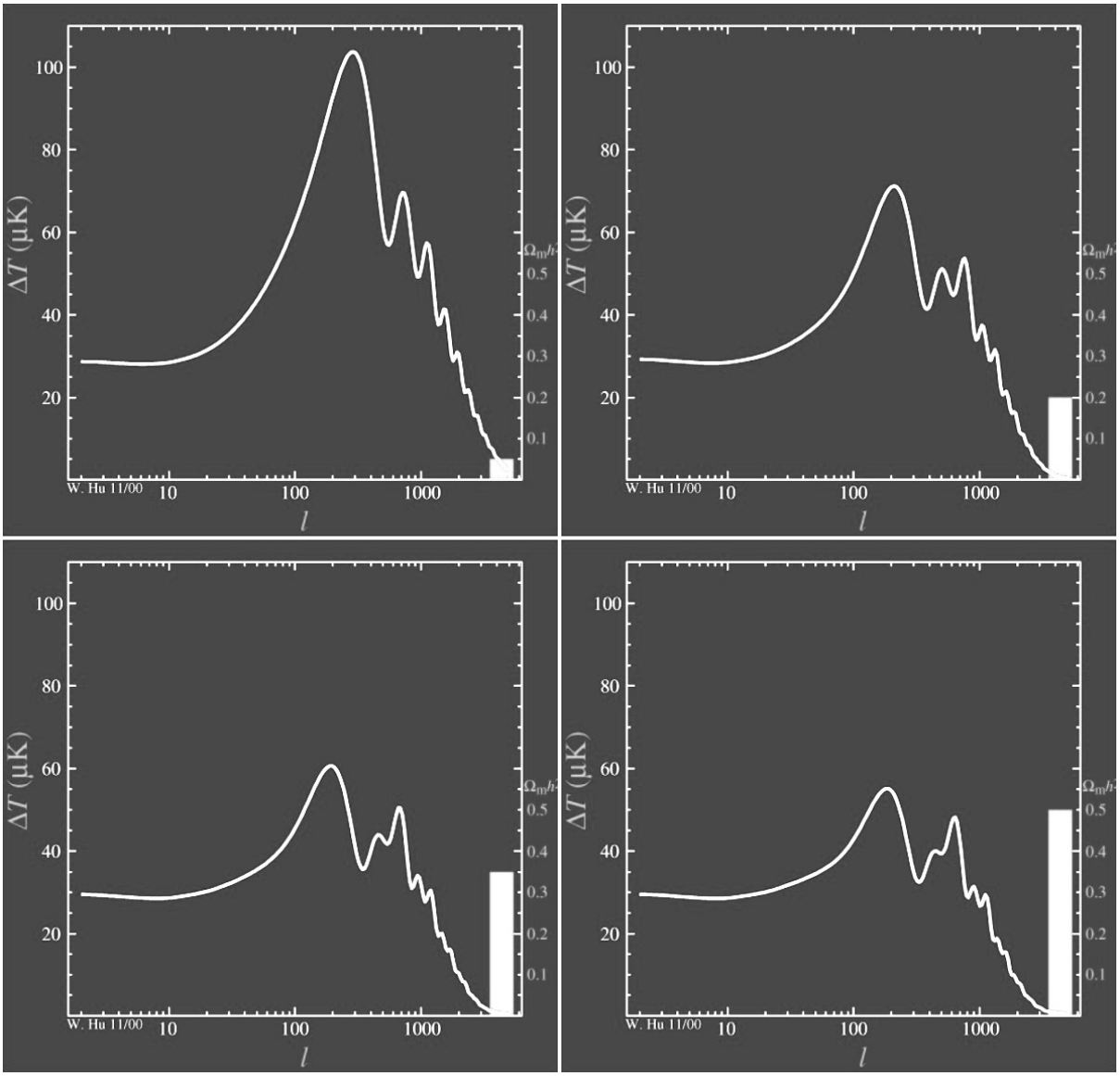

Figure 2.5: Angular power spectrum for different fractions of dark matter density (the white bar on the right). The acoustic peaks of the power spectrum are very sensitive to the amount of dark matter. Figures from http://background.uchicago.edu/~whu/intermediate/driving2.html

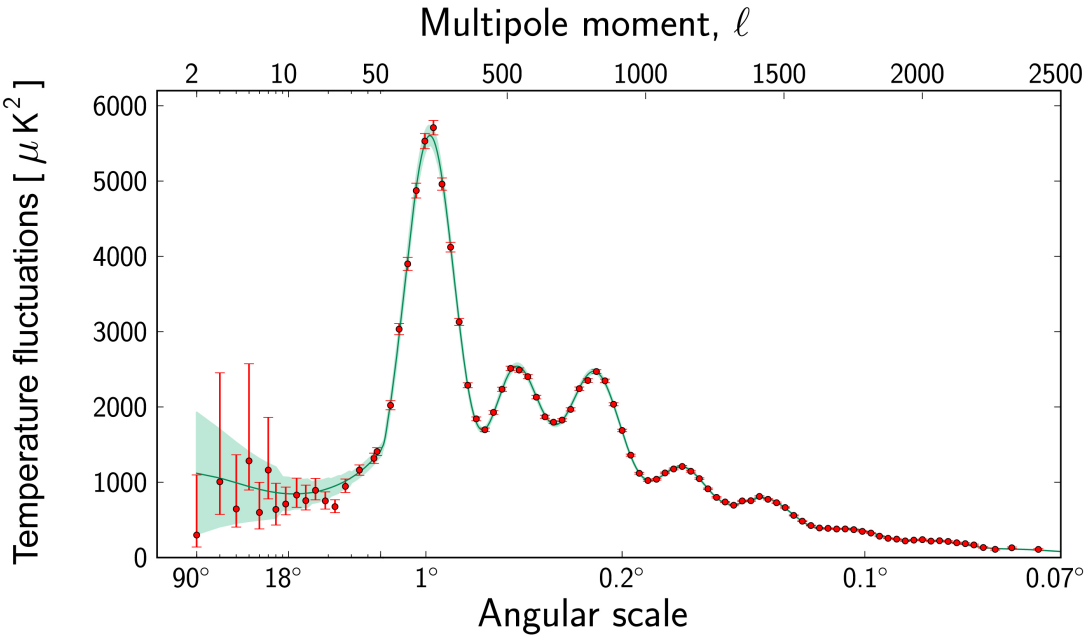

Figure 2.6: Measured and fitted angular power spectrum. The red dots are measurements made with Planck satellite and the green curve represents the best fit of the ΛCDM to the Planck data. Picture by ESA and Planck Collaboration.

2.2 Problems of the dark matter hypothesis

2.2.1 Missing satellites

Originally, in late 90's, it appeared that N-body simulations of dark matter done in the framework of ΛCDM predict more substructure, numbering in the 100s (for example [16] found ~ 500 satellites of the Milky Way), than what has been observed, numbering in ~ 10. This obvious discrepancy is called as the missing satellites problem (MSP) [17, 18]. Since then the observed satellite count has increased to ~ 50 [19] and other study even found the Sloan Digital Sky Survey data to be consistent with the simulations (e.g. [20]).

Since the MSP originates from DM simulations which do not contain baryonic matter, it has been also noted that adding the baryonic physics might resolve the problem [21, 22]. Furthermore even the precise prediction of ΛCDM might be off, since we do not know the true nature of DM. For example, replacing the cold dark matter with a warm dark matter model, e.g. keV sterile neutrino, would result to fewer satellites as some of the small scale structure would be "washed" away.

In the light of the significant uncertainties within the MSP, it is not regarded as an insurmountable dilemma for DM but rather as a result of incomplete analysis – which a decent DM model ultimately has to account for.

2.2.2 Too big to fail -problem

The "too big to fail" problem [23,24] highlights the fact that the same simulations that originate the MSP also predict these missing DM satellites to be massive enough to likely inhabit visible stars thus making them easy to detect. On the other hand, the smallest galaxies within the Milky Way seem to have a lot less dark matter than the simulations predict [25].

The too big to fail problem, like the MSP, could unravel by inclusion of baryonic physics into the simulations [22]. Also just having a warmer model of dark matter might be the solution [26]. Other suggested solutions to dilute the ΛCDM satellite density range from the relatively low mass of the dark matter halo of the Milky Way to the dark matter self-interactions, with a possibility of coupling to the radiation [27, and references therein].

2.2.3 Galactic Cusp vs. Core

The density profile of dark matter haloes at small radii have been observed to go like $\rho(r) \sim r^{\alpha}$, where $\alpha \sim 0$, resulting in flattening core-like profile, but in the meantime it is well established that in the ΛCDM simulations haloes of all masses develop profiles which have a central cusp $\rho \sim r^{-}\beta$, where $\beta \sim 1$. This failed prediction is known as the cusp vs. core problem [28–31].

Suggested solutions range from baryon physics [22,29,32,33] to (cold) dark matter self-interactions [34–36] and more recent proposals of warm dark matter [37,38].

2.2.4 Rarity of high velocity cluster mergers

Bullet-like cluster mergers are normally thought to be undisputed evidence for the existence of non-baryonic dark matter particle described by models like ΛCDM. Given the model of dark matter, we can ask how probable it is for the hydrodynamical and N-body dark matter simulations to produce events like bullet clusters and compare this to the actual observed occurrence in the universe.

The issue with bullet-like cluster mergers is that the observed shock velocities, $\sim 3000 \ldots 4500$km s^{-1}, seem to be too high to be reached in ΛCDM simulations [39]. In early works (for massive $\sim 10^{14} M_{\odot}$ haloes) the occurrence probability for these high velocity cluster mergers was obtained to be of the order of $10^{-11} \ldots 10^{-8}$ [41,42]. More recent and refined studies have found the occurrence probability to be higher, of the order of 10^{-4}, and have come to conclusion that the bullet-like cluster mergers do not present a challenge to the ΛCDM model [44,45]. In [22] it is noted that the observed shock velocity of $\sim 4500\,\mathrm{kms}^{-1}$ can be reached even with the infall velocity as low as $\sim 2600\,\mathrm{kms}^{-1}$, thus obsolescing the more extreme velocity searches.

Alongside with shock velocity differing from the infall velocity, the main confusion

in determining the compatibility of bullet clusters and ΛCDM comes from the way the bullet clusters are searched for in simulations, the chosen limits of the simulations, and the way the occurrence probability is defined. Earlier studies use the friends-of-friends (FOF) based algorithm which has a hard time distinguishing two haloes from each others at the moment of collision, which results in these events being neglected [39, 44]. More enhanced studies account for the high relative velocity of colliding haloes by probing the phase space. This method can easily distinguish these ongoing collisions as cluster mergers rather than a single halo [43, 45]. Also, in the earlier works, the occurrence probability is ill-defined, as it is roughly the number of extreme high velocity bullet clusters over the number of all colliding clusters. This makes the occurrence probability strongly dependent on the chosen parameters of the simulation, and it is not directly related to likelihood of observing such an object in the sky. For example, increasing the mass cut in the simulation results in less collisions in the system, but increases the probability, even though the lesser halo density in the system should reduce the number of seen bullet-like events [43].

This issue is well explained in [43], and the subject is investigated further in Refs. [46–50].

2.3 Dark matter genesis

This section, mostly following [51], briefly covers the most important production mechanisms that can yield the observed dark matter abundance. For more production mechanism variants see the aforementioned reference and references therein. The effort is to explain how the observed dark matter abundance can arise from the interplay of expansionary cooling of the universe and interactions between the dark and visible sectors. The visible sector consists of the standard model fields and the dark sector consists of fields beyond that, including dark matter. In the very early universe the Standard Model fields within the visible sector are in thermal equilibrium with each. The relevant production mechanism of dark matter is determined by the interaction strength between the dark matter and the visible sector heat bath, which either brings the dark matter into equilibrium with the visible sector or not. In the case that dark matter species reaches the thermal equilibrium with the visible sector but would never depart from it, its present day abundance would be absolutely negligible due to the Boltzmann suppression $n/s \sim (m/T)^{3/2} \exp(-m/T)$ [3].

The evolution of dark matter number density is governed by the Boltzmann equation [3]

$$\frac{dn}{dt} + 3Hn = \frac{g}{(2\pi)^3} \int C[f] \frac{\mathrm{d}^3 k}{E}\,, \tag{2.3.1}$$

which is here given in terms of number density n, but is introduced and discussed in its more general form in Appendix A. The $3Hn$ term accounts for the dilution effect from the expansion of the universe, and the right-hand side accounts for the interactions that change the total number of particles. The right-hand side is known as the collision term of the Boltzmann equation and its general form is reported only in Appendix A.

2.3.1 Freeze-out

If the coupling between the two sectors is strong enough, the dark sector will reach the thermodynamical equilibrium with the visible sector heat bath. The coalition follows the thermic behaviour of cooling universe until the interaction rate of the interactions that keep the dark sector and the visible sector equilibrated becomes dwarfed by the Hubble expansion rate. At that point the comoving number density of the relevant dark sector species freezes out to a constant value. Note that the dark sector can contain other fields besides the one reaching the equilibrium with the visible sector and these other fields are not necessarily in the equilibrium state.

The freeze-out mechanism requires roughly a weak scale coupling, $y \simeq \mathcal{O}(0.1)$ to yield the observed dark matter abundance [51]. This has caused the dark matter produced by the freeze-out mechanism to be called the WIMP (Weakly Interacting Massive Particle).

The simplest case of thermal freeze-out of dark matter, labeled χ, assumes a stable Majorana dark matter particle ($\overline{\chi} = \chi$) with no large self-interactions. In this scenario, the relevant processes are the annihilations $\chi\overline{\chi} \to f\overline{f}$ and the inverse annihilations $f\overline{f} \to \chi\overline{\chi}$ for some Standard Model fermion f, as they are the only processes that can change the particle number of χ in the comoving volume. For the case of asymmetric dark matter see [52–54], and for the case of dark matter with relevant self-interactions see [54–58].

The Boltzmann equation in this simple scenario is [3]

$$\frac{dn_\chi}{dt} + 3Hn_\chi = -\langle v\sigma_\chi \rangle \left[n_\chi^2 - (n_\chi^{\mathrm{eq}})^2 \right] , \tag{2.3.2}$$

where $\langle v\sigma_\chi \rangle$ is the thermal average of the total annihilation cross section times velocity [3,59], n_χ is the dark matter number density and n_χ^{eq} is the dark matter number density value at equilibrium.

Before solving the freeze-out equation (2.3.2), we can already deduce the behaviour dark matter number density at the high and low temperature limits. At temperatures well above the dark matter mass $T > m_\chi$ the equilibrium number density goes like $n_\chi^{\mathrm{eq}} \sim T^3$ and assuming most of the dark matter production to take place during the radiation dominated era when $H \sim T^2/M_{\mathrm{pl}}$, the Hubble term can be neglected. Then looking for a steady state by setting the derivative term to zero[3] we find that the number density is driven towards the equilibrium value $n_\chi \to n_\chi^{\mathrm{eq}}$.

[3] By this way we are looking for the steady state to which the dark matter number density is driven.

As the temperature cools below the dark matter mass $T < m_\chi$ the equilibrium number density becomes exponentially suppressed $n_\chi^{\rm eq} \sim \exp(-m_\chi/T)$ and also the thermally averaged cross section becomes less important. Then the collision term on the right hand side of Eq. (2.3.2) can be neglected, and the comoving number density freezes out to a constant value: $\dot{n}_\chi = -3Hn_\chi$, and $H = \dot{a}/a$ dominates the evolution resulting in expansionary dilution of the number density $n_\chi \sim a^{-3}$.

It is a common practice to recast Eq. (2.3.2) in terms of the dimensionless parameters $Y \equiv n_\chi/s$ and $x \equiv m_\chi/T$, where s and T are the entropy density and temperature of the visible sector. Y is called as the *yield*. Also, to get a rough picture, it is often sufficient to assume the relativistic degrees of freedom remain constant during the dark matter production. Then the freeze-out equation can be cast as [3]

$$\frac{x}{Y_{\rm eq}}\frac{dY}{dx} = -\frac{\Gamma}{H}\left[\left(\frac{Y}{Y_{\rm eq}}\right)^2 - 1\right], \tag{2.3.3}$$

where $\Gamma \equiv n_{\rm eq}\langle v\sigma_\chi\rangle$ is the effective interaction rate between the dark matter and thermal bath particles. The freeze-out process is depicted in the left panel of Fig. 2.7. There the yield Y goes through the same evolution as described for number density n above: in the region $H < \Gamma$ the dark sector rapidly equilibrates with the visible sector and $Y \simeq Y_{\rm eq}$, but at $H \simeq \Gamma$ the annihilations shut off and the dark matter abundance freezes out.

From Eq. (2.3.3) an approximate solution for the present-day dark matter abundance is [3]

$$\Omega_\chi h^2 \simeq 1.07\times 10^9 \frac{\sqrt{g_*}}{g_{*s}}\frac{(n+1)x_f {\rm GeV}^{-1}}{M_{Pl}\langle v\sigma_\chi\rangle}, \tag{2.3.4}$$

where g_* and g_{*s} are the effective numbers of relativistic degrees of freedom for the entropy and energy densities respectively, $M_{Pl} = 1/\sqrt{8\pi G}$ is the reduces Planck mass, and $(n+1)$ comes from the expansion of the thermally averaged cross section $\langle v\sigma_\chi\rangle \simeq \sigma_n x^{-n}$ and $n = 0$ for s-wave annihilation, $n = 1$ for p-wave annihilation etc. This approximation holds only if the dark matter is non-relativistic at the time of freeze-out x_f, which can be defined as the point where $|3Hn_\chi| \simeq \left|\langle v\sigma_\chi\rangle\left[n_\chi^2 - (n_\chi^{\rm eq})^2\right]\right|$.

At least five exceptions are known where the basic freeze-out calculation fails or needs more subtlety: the coannihilation, the annihilation into forbidden channels, and the annihilation near poles [60], the semi-annihilations [62–64], and the co-scatterings [65].

2.3.2 Freeze-in

In contrast to the freeze-out, in the freeze-in mechanisms the dark matter abundance is produced out-of equilibrium. The freeze-in production of dark matter occurs when the

This state is of course steady in a sense that it is rapidly stabilised right after the expansion has shaken the stability.

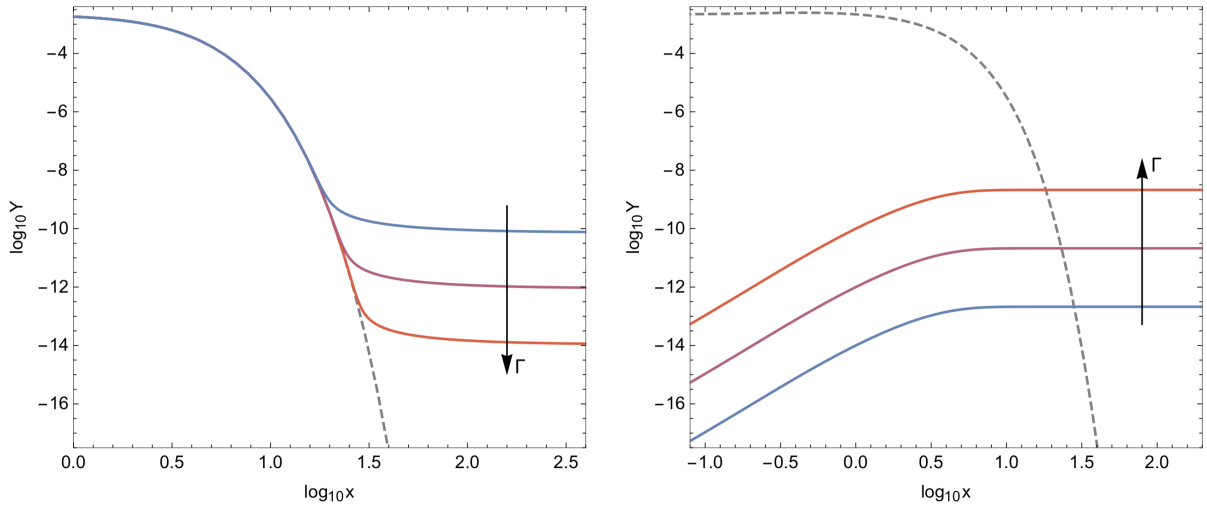

Figure 2.7: The freeze-out (on the left) and the freeze-in (on the right) production of dark matter for three different interaction strenghts Γ (coloured solid lines). The arrows indicate the effect of increasing the interaction rate Γ. In the left panel $x = m_\chi/T$ and gray dashed line is the equilibrium density of dark matter. In the right panel $x = m_\sigma/T$, where σ is the particle decaying into dark matter and gray dashed line is the equilibrium density of σ. Figure from [51].

interactions between the dark and visible sectors are too weak, typically $y \lesssim \mathcal{O}(10^{-7})$ [66, 67], to equilibrate the dark matter with the visible sector heat bath [68, 69]. The dark matter abundance generated this way is generally called as the FIMP (Feebly Interacting Massive Particle).

In the simplest case of non-thermal freeze-in, the initial number density of dark matter is negligible and the final abundance is produced by bath particle decays e.g. $\sigma \to \chi\chi$, where σ is a particle in the visible sector heat bath and χ is the dark matter particle [51, and references therein]. The freeze-in production is active until all σ particles have decayed or until the number density of σ becomes Boltzmann-suppressed, $n_\sigma \sim \exp(-m_\sigma/T)$. As the freeze-in production of dark matter shuts off, the comoving number density of dark matter freezes in to a constant value, as depicted in the right panel of Fig. 2.7.

In the case of dark matter production by decays of bath particles $\sigma \to \chi\chi$, the Boltzmann equation is

$$\frac{dn_\chi}{dt} + 3Hn_\chi = \int \mathrm{d}\Pi_\sigma \mathrm{d}\Pi_{\chi_1} \mathrm{d}\Pi_{\chi_2} (2\pi)^4 \delta^{(4)}(p_\sigma - p_{\chi_1} - p_{\chi_2}) \times \left[|\mathcal{M}|^2_{\sigma\to\chi\chi} f_\sigma \left(1 \pm f_{\chi_1}\right)\left(1 \pm f_{\chi_2}\right) - |\mathcal{M}|^2_{\chi\chi\to\sigma} f_{\chi_1} f_{\chi_2} \left(1 \pm f_\sigma\right) \right] , \quad (2.3.5)$$

where + (-) applies for bosons (fermions), the matrix element squared $|\mathcal{M}|^2$ is averaged over initial *and* final states, f_i is the phase space density of particle species i, and the phase space measure for the particle species i possessing g_i internal degrees of freedom

is denoted as

$$\mathrm{d}\Pi_i \equiv \frac{g_i \mathrm{d}^3 p_i}{(2\pi)^3 2E_i} \,. \tag{2.3.6}$$

Assuming the initial dark matter abundance to be negligible, so that we may set $f_\chi = 0$, and applying the definition of the particle decay width for the process $\sigma \to \chi\chi$:

$$\Gamma_{\sigma\to\chi\chi} \equiv \frac{g_\sigma}{2m_\sigma} \int \Pi_{\chi_1}\Pi_{\chi_2}(2\pi)^4\delta^{(4)}(p_\sigma - p_{\chi_1} - p_{\chi_2})|\mathcal{M}|^2_{\sigma\to\chi\chi} \,, \tag{2.3.7}$$

the Boltzmann equation (2.3.5) can be cast as

$$\frac{dn_\chi}{dt} + 3Hn_\chi = \frac{g_\sigma m_\sigma^2 \Gamma_{\sigma\to\chi\chi}}{2\pi^2} T K_1(m_\sigma/T) \,, \tag{2.3.8}$$

and its approximative solution for the relic abundance in this case is [69]

$$\Omega_\chi h^2 \approx \left(\frac{1.09\times 10^{27} g_\sigma}{g_{*s}\sqrt{g_*}} \frac{m_\chi \Gamma_{\sigma\to\chi\chi}}{m_\sigma^2} \right) \Big|_{T\simeq m_\sigma} \,. \tag{2.3.9}$$

To estimate the required coupling strength y between the σ and χ, we let $g_{*s} \simeq g_*$ and $\Gamma_{\sigma\to\chi\chi} \simeq y^2 m_\sigma/(8\pi)$, yielding [51]

$$y \simeq 10^{-12} \left(\frac{\Omega_\chi h^2}{0.12}\right)^{1/2} \left(\frac{g_*}{100}\right)^{3/4} \left(\frac{m_\sigma}{m_\chi}\right)^{1/2} \,, \tag{2.3.10}$$

which is in good concordance with the initial assumption that the dark sector never equilibrates with the visible sector due to the feeble interaction strength coupling them.

2.3.3 Dark freeze-out

The final abundance of dark matter is not solely determined by the initial freeze-in or freeze-out from the visible sector, but interactions within the dark sector can also play an important role [51, and Refs. therein].

If the interactions of dark matter within the dark sector are strong enough, they can produce a thermal equilibrium within the dark sector that differs from that of the visible sector. This can be relevant even if the dark sector consists only of the dark matter itself. The so-called dark freeze-out happens when the dark matter particles depart from the dark sector thermal equilibrium and their final abundance freezes out. Depending on the interactions within the dark equilibrium, the dark matter abundance after the dark freeze-out can differ significantly from the initially produced abundance by freezing in/out from the visible sector.

The number changing interactions of dark matter can alter its abundance and momentum distribution. Using the example from [51]: in the equilibrium the number changing processes $2 \to 4$ and $4 \to 2$ occur at the same rate, but when the dark matter becomes non-relativistic the $2 \to 4$ scatterings shut off while the $4 \to 2$ annihilations

maintain the dark matter number density in equilibrium value. This so-called cannibalisation of dark matter reduces its number density while increasing the average momentum i.e. the dark matter heats itself by transferring its momentum and rest-energy of the annihilating particles to lesser amount of particles.

In the above consideration, the entropy is conserved within the dark matter species, but having more than one particle species in the dark sector allows entropy transfer between the different species, making the structure more complicated. Then the final abundance depends on couplings and masses of dark sector species, as well as the couplings to the visible sector. An example and more details about the dark freeze-out are given in Chapter 5, where the results of our model are presented.

2.4 Summary of the chapter

In this chapter we constructed the dark matter hypothesis and discussed the observational evidence supporting it. We briefly reviewed the known discrepancies related to the dark matter hypothesis and noted that many of them may arise due to uncertainties or incompletion in numerical analysis. On the other hand the ΛCDM model might require modification to over come these issues. Then the basic production mechanisms of dark matter, the freeze-in and freeze-out, are presented. Also the dark freeze-out is shortly covered, but is discussed in more detail at Chapter 5 alongside with numerical results obtained from the model described in Chapter 3.

Chapter 3

STERILE NEUTRINO DARK MATTER FROM SINGLET SCALAR DECAYS

In this chapter we concentrate on a widely studied model of *warm* dark matter motivated by neutrino physics: a sterile neutrino ν_s with a keV-scale mass. This chapter is based on [71], which was the first to advance the study of dark matter in terms of momentum distribution functions. The topic was further expanded by the same authors with less stringent assumption in [72].

The intent of this chapter is to solve the momentum distribution function of sterile neutrino dark matter produced by the decays of singlet scalars. *This is done under an assumption of vanishing active-sterile mixing between the neutrinos.*

Allowing the active-sterile mixing would allow some sterile neutrino dark matter production also by non-resonant active-sterile transitions via the DW mechanism, as first proposed by [73–75] and applied to dark matter by Dodelson and Widrow [76]. The DW mechanism cannot act as the sole production mechanism for sterile neutrino dark matter, but it can cause at most a few percent modification to relic abundance of sterile neutrinos produced mainly by some other mechanism [51, 77]. Nevertheless, in the Shi-Fuller (SF) mechanism, it is possible to produce the correct relic abundance of sterile neutrino dark matter just by active-sterile transitions if the transitions are resonantly enhanced by the presence of a primordial lepton number asymmetry in the early universe. This resonant active-sterile mixing was first proposed by [78] and applied to dark matter by Shi and Fuller [79].

Although the SF mechanism can produce the correct relic abundance, it still requires a sizeable primordial lepton asymmetry between the particle and antiparticle number densities [80]:

$$\mathcal{L}_\alpha \equiv \frac{n_{\nu_\alpha} - n_{\overline{\nu}_\alpha}}{n_\gamma} = \mathcal{O}(10^{-4})\,, \tag{3.0.1}$$

where α is the flavour index and n_γ is the photon number density. Such a primordial lepton asymmetry has not been verified, as it remains much below the probe of current searches with light element abundances, which only see up to $\mathcal{L}_\alpha \sim 0.1$ [80]. The

lepton number asymmetry should also be much more extreme than measured (and still unexplained) baryon number asymmetry [81]

$$\eta_B \equiv \frac{n_B - n_{\overline{B}}}{n_\gamma} \approx (6.160 \pm 0.148) \times 10^{-10} \,. \tag{3.0.2}$$

On the grounds of above discussion, we will continue with the assumption of vanishing active-sterile neutrino mixing: as the SF mechanism is not fully excluded, it is threatened by big-bang nucleosynthesis [71], and the DW can only give minute corrections to sterile neutrino dark matter.

3.1 Setting up the model

In the general sense, our model contains the Standard Model visible sector augmented with the dark sector consisting of two new particles, a parent particle χ_P and an offspring decay product χ_O. Both particles in the dark sector can contribute to the final dark matter abundance, but in our framework the offspring particle χ_O is assumed to serve this purpose solely. Also both χ_P and χ_O can couple to some SM degree of freedom (DOF), denoted as $X_{\rm SM}$, resulting to following interaction processes[1]:

- $X_{\rm SM}X_{\rm SM} \leftrightarrow \chi_P\chi_P$: 2-to-2 scatterings of SM particles to DM parent particles and their reverse process.
- $X_{\rm SM}X_{\rm SM} \leftrightarrow \chi_O\chi_O$: 2-to-2 scatterings of SM particles to DM offspring particles and their reverse process.
- $X_{\rm SM} \leftrightarrow \chi_P\chi_P$: decays of SM particle into DM parent particles and their reverse process.
- $X_{\rm SM}X_{\rm SM} \leftrightarrow \chi_O$: decays of DM offspring particles into SM particles and their reverse process.
- $\chi_P \leftrightarrow \chi_O\chi_O$: decays within the dark sector from parent particle to offspring particles and their reverse process.
- $\chi_P\chi_P \leftrightarrow \chi_O\chi_O$: 2-to-2 scatterings within the dark sector between the parent particles and the offspring particles and their reverse process.

The dynamics of the SM DOF is governed by the effective number of entropy DOF, $g_{*s}(T)$, which contains the information of decouplings of SM species from the visible sector heat bath due the Hubble expansion.

[1] Possible number changing processes within the particle species (i.e. $\chi\chi\chi \to \chi\chi$), known as the cannibalisation, are not taken into account.

In our model, which is based on the model from [71], we assume the dark sector to consist of a real singlet scalar field S and a right-handed sterile neutrino field N. The visible and dark sector interact through the Higgs portal coupling λ between the singlet scalar S and the Higgs H via the most generic scalar potential under an assumed global $\mathbb{Z}_4$-symmetry:

$$V_{\text{scalar}} = -\mu_H^2 H^\dagger H - \frac{1}{2}\mu_S^2 S^2 + \lambda_H (H^\dagger H)^2 + \frac{\lambda_s}{4} S^4 + 2\lambda (H^\dagger H) S^2 \,, \tag{3.1.1}$$

and within the dark sector the scalar and the neutrino are coupled via the explicitly $\mathbb{Z}_2$-breaking Yukawa coupling y:

$$\mathcal{L} \supset -\frac{y}{2} S \overline{N^c} N + \text{h.c.} \tag{3.1.2}$$

For a non-zero vacuum expectation value (VEV) $\langle S \rangle$ of the scalar, the neutrino gets a Majorana mass $m_N = y \langle S \rangle$, and assuming the scalar VEV to be a rather large $\langle S \rangle \approx \mathcal{O}(\text{GeV}) - \mathcal{O}(\text{TeV})$ would require the Yukawa coupling to be $y \sim 10^{-9} - 10^{-5}$ in order to have a keV-scale sterile neutrino [71].

The complete Lagrangian of our model is

$$\mathcal{L} = \mathcal{L}_{\text{SM}} + \left[\frac{i}{2} \overline{N} \partial\!\!\!/ N + \frac{1}{2} (\partial_\mu S)(\partial^\mu S) - \frac{y}{2} S \overline{N^c} N + \text{h.c.} \right] - V_{\text{scalar}} + \mathcal{L}_\nu \,, \tag{3.1.3}$$

where $\mathcal{L}_\nu$ denotes the Lagrangian giving mass to active neutrinos. The same model is considered in [71,72] and similar models are considered in [82–84].

Furthermore, our model adds some constraints to the possible interaction processes mentioned in the beginning of this chapter, which we will now analyse. The singlet scalar acts now as the parent particle in the dark sector and the sterile neutrino as its offspring particle.

- Firstly, since the sterile neutrino is assumed to not be coupled to the SM heat bath, reaction terms $X_{\text{SM}} X_{\text{SM}} \leftrightarrow \chi_O \chi_O$ and $X_{\text{SM}} X_{\text{SM}} \leftrightarrow \chi_O$ are not present in our model. In general, any decay channel of the meant-to-be dark matter particle χ_O should be limited by the required stability of dark matter.

- Secondly, we assume the singlet scalar to be much more massive than the Higgs, $m_s \approx \mathcal{O}(\text{GeV}) - \mathcal{O}(\text{TeV})$, and the sterile neutrino to be in the keV scale. This shuts off the decay channel $X_{\text{SM}} \to \chi_P \chi_P$ and the scattering channel $\chi_O \chi_O \to \chi_P \chi_P$ due to mass hierarchy between the particles.

- Thirdly, the 2-to-2 processes $\chi_P \chi_P \leftrightarrow \chi_O \chi_O$ within the dark sector are absent since they are proportional to y^4 and hence suppressed by the smallness of the Yukawa coupling y.

- Lastly, due to heavily suppressed kinematics of the phase space of any 2-to-1 process, also $\chi_P \chi_P \to X_{\text{SM}}$ and $\chi_O \chi_O \to \chi_P$ are absent.

We have summarised the above discussion about the interaction processes of our model in the chart below.

Open channels	Closed channels
$HH \to SS$	$HH \leftrightarrow NN$
$S \to NN$	$H \to SS$
	$SS \leftrightarrow NN$
	$SS \to H$
	$NN \to S$

Without our underlying approximation of vanishing active-sterile mixing between the neutrinos, we would need to take other interaction channels into account as well.

3.2 Solving the Boltzmann equation for the particle spectra

We wish to solve the momentum distribution function f_i from the Boltzmann equation

$$\tilde{L}[f_i] = \tilde{C}[f_i]\,, \tag{3.2.1}$$

where $i = S, N$ labels the real singlet scalars S, and the right-handed sterile neutrinos N. The general form of the collision term $\tilde{C}[f_i]$ along with derivation of the Liouville term $\tilde{L}[f_i]$ are reported in Appendix A.

As shown in Appendix B, the change of variables to

$$\begin{cases} x \equiv \frac{p}{T}\,, \\ r \equiv \frac{m_s}{T}\,, \end{cases} \tag{3.2.2}$$

allows us to write the Liouville operator on the left-hand side of (3.2.1) as

$$\tilde{L} = \frac{\partial}{\partial t} - Hp\frac{\partial}{\partial p} = \frac{dr}{dT}\frac{dT}{dt}\frac{\partial}{\partial r}\,, \tag{3.2.3}$$

where we have assumed the both energy and entropy degrees of freedom to be constant. As discussed in the previous section, processes that affect to the spectra of scalars are $hh \to SS$, $SS \to hh$ and $S \to NN$, and the spectrum of neutrinos is affected only by the decays from scalars $S \to NN$. Equation (3.2.1) can now be written as

$$\begin{cases} \frac{dr}{dT}\frac{dT}{dt}\frac{\partial f_S}{\partial r} = C^S_{hh\to SS} + C^S_{SS\to hh} + C^S_{S\to NN}\,, \\ \\ \frac{dr}{dT}\frac{dT}{dt}\frac{\partial f_N}{\partial r} = C^N_{S\to NN}\,. \end{cases} \tag{3.2.4}$$

Note that using Eq. (3.2.2) and the time-temperature relation (g_* being constant) $\frac{dT}{dt} = -HT$, we get $\frac{dr}{dT}\frac{dT}{dt} = \frac{m_S}{M_0}T$, where use the same definition of M_0 as [71]:

$$M_0 \equiv \left(\frac{45M_{Pl}^2}{4\pi^3 g_*}\right)^{1/2} = 7.35 g_*^{-1/2} \times 10^{18}\mathrm{GeV}. \tag{3.2.5}$$

Explicit derivation of the collision terms in Eq. (3.2.4) are done in Appendix C.

For the scalar part of Eq. (3.2.4) we get the following integro-differential equation

$$\begin{aligned}\frac{\partial f_S(x,r)}{\partial r} = \frac{M_0}{m_S T}\Bigg[& T\frac{|\mathcal{M}|^2_{hh\to SS}}{256\pi^4}\frac{e^{-\sqrt{x^2+r^2}}}{\sqrt{x^2+r^2}}\cdot\mathcal{F}(x,r,\xi) \\ & - T\frac{|\mathcal{M}|^2_{SS\to hh}}{256\pi^4}\frac{f_S(x,r)}{\sqrt{x^2+r^2}}\int \mathrm{d}^3x'\,\mathcal{G}(x',x,\cos\theta,r,\xi)f_S(x',r) \\ & - T\frac{r^2}{\sqrt{x^2+r^2}}\frac{\Gamma_{S\to NN}}{m_S}f_S(x,r)\Bigg]\,, \end{aligned} \tag{3.2.6}$$

where the kinetic functions $\mathcal{F}(x,r,\xi)$ and $\mathcal{G}(x',x,\cos\theta,r,\xi)$, as well as the matrix elements $|\mathcal{M}|^2_{SS\to hh}$, $|\mathcal{M}|^2_{hh\to SS}$, and the decay width $\Gamma_{S\to NN}$ are given in Appendix C. Here θ is the angle between the two Higgs $h(x)$, $h(x')$, and $\xi \equiv m_h/m_s$.

For the neutrino part of Eq. (3.2.4) we get

$$\frac{\partial f_N(x,r)}{\partial r} = \frac{M_0}{m_S T}\left[\frac{2r\Gamma_{S\to NN}}{x^2}\int_{x'_{\min}}^{x'_{\max}}\mathrm{d}x'\frac{x'}{\sqrt{x'^2+r^2}}f_s(x',r)\right]\,, \tag{3.2.7}$$

where the integration limits are determined by energy conservation, which requires $\left|\frac{2E_pE_k-m_S^2}{2|\mathbf{p}||\mathbf{k}|}\right| \leq 1$, and where $\mathbf{p} = \mathbf{x}'T$ and $\mathbf{k} = \mathbf{x}T$ are the momenta of the scalar and the neutrino respectively.

Then we will introduce two new dimensionless auxiliary quantities which will span our parameter space:

$$\begin{cases} \mathcal{C}_{\mathrm{HP}} & \equiv \frac{M_0}{m_S}\frac{\lambda^2}{16\pi^3} \qquad \textit{(effective Higgs portal)}\,, \\ \mathcal{C}_{\Gamma} & \equiv \frac{M_0}{m_S}\frac{\Gamma}{m_S} \qquad \textit{(effective decay width)}\,. \end{cases} \tag{3.2.8}$$

In a more general picture, these new effective parameters can deviate from the Higgs portal coupling λ and the Yukawa coupling y (here $\Gamma \sim y^2$) due to depletion of energy degrees of freedom $g_*(T)$, but we assume this depletion to be negligible at the time of dark matter production. This sets M_0 to be constant, and hence the effective parameters inherit their values directly from the Lagrangian level parameters y and λ. Furthermore, we will now apply the assumed mass hierarchy i.e. we will employ our a-priori assumptions of a keV sterile neutrino and a heavy $\mathrm{GeV}-\mathrm{TeV}$ singlet scalar as:

$$m_N \ll m_h \ll m_S\,, \tag{3.2.9}$$

which leads to $\xi \ll 1$. Under these assumptions the scalar equation (3.2.6) becomes

$$\begin{aligned}&\frac{\partial f_S(x,r)}{\partial r} = \\ &\mathcal{C}_{\mathrm{HP}}\frac{e^{-\sqrt{x^2+r^2}}}{\sqrt{x^2+r^2}}rK_1(r) - \mathcal{C}_{\mathrm{HP}}\frac{f_S(x,r)}{\sqrt{x^2+r^2}}\int_0^\infty \mathrm{d}x'\frac{x'^2}{\sqrt{x'^2+r^2}}f_S(x',r) - \mathcal{C}_{\Gamma}\frac{r^2}{\sqrt{x^2+r^2}}f_S(x,r)\,,\end{aligned} \tag{3.2.10}$$

and the neutrino equation (3.2.7) becomes

$$\frac{\partial f_N(x,r)}{\partial r} = 2\mathcal{C}_\Gamma \frac{r^2}{x^2} \int\limits_{\left|x-\frac{r^2}{4x}\right|}^{\infty} \mathrm{d}x' \frac{x'}{\sqrt{x'^2+r^2}} f_S(x',r)\,. \tag{3.2.11}$$

Equations (3.2.10) and (3.2.11) are the culmination of our analytical reduction and numerical treatment is required for their precise solutions. Nevertheless, further analytical solutions can be achieved [71], but only in an approximative manner, and ultimately these only verify the behaviour of the numerical solution in a given region.

In general, Eqs. (3.2.10) and (3.2.11) form a system of non-linear partial integro-differential equations as, depending on the relevant collision terms, each equation can depend on the other's solution in a highly non-trivial manner. Fortunately, under our current assumptions, the two equations are decoupled in the sense that Eq. (3.2.10) depends solely on the scalar distribution function $f_S(x,r)$ and Eq. (3.2.11) does not depend on the neutrino distribution function $f_N(x,r)$ at all. This can be used to our benefit, as we may now solve (numerically) the scalar distribution function from Eq. (3.2.10) and then plug it into the integrated form of the neutrino equation [71]:

$$f_N(x,r) = \int\limits_0^r \mathrm{d}r'\, 2\mathcal{C}_\Gamma \frac{r'^2}{x^2} \int\limits_{\left|x-\frac{r'^2}{4x}\right|}^{\infty} \mathrm{d}x' \frac{x'}{\sqrt{x'^2+r'^2}} f_S(x',r')\,. \tag{3.2.12}$$

Although the form of Eq. (3.2.12) is very suggestive, we do not encourage its use: since in the more general situations, e.g. [72], one does not have such a luxury available, so it is more useful to *not* use it in here either. Instead, we implement Eqs. (3.2.10) and (3.2.11) in this (pseudo-) coupled form, in anticipation of future works.

3.3 Summary of the chapter

In this chapter, we have briefly motivated the model of sterile neutrino dark matter and discussed how it could have been produced in the early universe. We laid out our minimally-extended Standard Model Lagrangian with the Higgs portal coupling between the visible and the dark sector and discussed the arising phenomenology. Based on these considerations, we derive the system of Boltzmann equations to be solved numerically at the level of momentum distribution functions. The chapter concludes with the anticipative understanding of the numerical solutions presented in Chapter 5.

Up to now we have been busy describing our model and deriving the relevant equations i.e. Eqs. (3.2.10) and (3.2.11). The model, however, should concord with the observed universe, and to ensure this we must know how the different aspects of the formation of structure in various epochs of early universe relate to our model. Hence,

before going into results, we will discuss in the next chapter the different constraints invoked by cosmology and structure formation.

Chapter 4

CONSTRAINTS FROM COSMOLOGY

This chapter introduces various constraints on the parameters of the model $\{y, \lambda\}$ by including bounds from cosmology and structure formation. The parameter space of this model is discussed very thoroughly in Refs. [71, 72], so we will make use of this and fix the scalar mass to be $m_S = 1\,\mathrm{TeV}$ [1] in order to be able to rely on their discussion.

The approach is such that the parameter space is spanned by $(\mathcal{C}_{\mathrm{HP}}, \mathcal{C}_{\Gamma})$ and the allowed parameters are constrained by certain limits and observations. We will first discuss what these restrictions are, and then consider their effect on our parameter space.

4.1 Constraints in general

This section quickly skims through the most relevant constraints which will be used in the next section to narrow down the parameter space $(\mathcal{C}_{\mathrm{HP}}, \mathcal{C}_{\Gamma})$ of our model. A more thorough list of constraints can be found in the recent reviews [51, 80]. We name only the utmost critical ones here.

4.1.1 Abundance bound

The most obvious bound that the model must produce is the observed dark matter abundance in the universe measured by the Planck satellite [4]:

$$\Omega_{\mathrm{DM}} h^2 = 0.1188 \pm 0.0010\,. \tag{4.1.1}$$

[1] This guarantees the assumption $m_h \ll m_S$ made in Eq. (3.2.9), but other values satisfying this condition would be equally valid. The possibility of a light scalar $m_S \ll m_h$ is considered in [72], but in this case the more general form of the collision terms must be used (the ones where we have not yet assumed $m_h \ll m_S$).

From the theory we get the momentum distribution function $f_N(x, r)$ for the sterile neutrinos, from which we compute their number density as

$$n_N(r) = \frac{g_N}{2\pi^2} \int_0^\infty \mathrm{d}x \frac{\mathrm{d}p}{\mathrm{d}x} p^2(x) f_N(x, r) = \frac{g_N}{2\pi^2} \left(\frac{m_S}{r}\right)^3 \int_0^\infty \mathrm{d}x\, x^2 f_N(x, r)\,, \tag{4.1.2}$$

where $g_N = 2$ is the sterile neutrino spin DOF. This then gives the dark matter abundance as [72]

$$\Omega_{\mathrm{DM}} h^2 = \frac{s_0}{s(r_{\mathrm{prod}})} \frac{m_N n(r_{\mathrm{prod}})}{\rho_{\mathrm{crit}}/h^2}\,. \tag{4.1.3}$$

where $s_0 = 2891.2\,\mathrm{cm}^{-3}$ [9] and $s(r_{\mathrm{prod}})$ are the entropy densities today and at the time of production, $\rho/h^2 = 1.054 \times 10^{-2}\,\mathrm{MeV cm}^{-3}$ [9] is the critical density in units of the (squared) reduced Hubble constant h, and $n(r_{\mathrm{prod}})$ is the number density at the time of production.

The inclusion of the abundance bound is done by first solving the distribution function $f_N(x, r)$ at some parameter space point $(\mathcal{C}_{\mathrm{HP}}, \mathcal{C}_\Gamma)$ and then fixing the mass of the sterile neutrino m_N to be such that the right-hand side of Eq. (4.1.3) agrees with Eq. (4.1.1). We allow the mass of the sterile neutrino to be within the range of $0.5\,\mathrm{keV} < m_N \leq 100\,\mathrm{keV}$, as the low end of the mass scale is ultimately limited by the Tremaine-Gunn limit discussed in the next section, and the upper mass limit comes from the framework of keV-scale sterile neutrinos.

4.1.2 Tremaine-Gunn limit

The phase space of any fermion species is coarse-grained by Pauli blocking, and this can be used to derive a lower mass bound for sterile neutrino dark matter. Arising mass bound is known as the Tremaine-Gunn (TG) limit. In their original work, Tremaine and Gunn [85] argued that the massive galactic haloes cannot be composed of stable neutral leptons of mass $\lesssim 1\mathrm{MeV}$. Their argument relies on the assumed initial thermal distribution and the uniform distribution of the dark matter, whose maximum phase space density is then traced back to present day by the Vlavson equation (Boltzmann equation without collisions), which they then compare to observed quantities to derive the lower bound. Because of the assumed initial phase space density, this method is not very helpful in the non-thermal dark matter production schemes.

However, for fermionic dark matter, a similar but less stringent lower mass bound can be derived just by comparing the average phase space density of dark matter in given astrophysical object(s) to the that of a degenerate Fermi gas, resulting in the lower bound of [86]

$$m_{\mathrm{DM}} > 0.41\,\mathrm{keV}\,. \tag{4.1.4}$$

Other authours [51, 71, 72] cite a bit higher value: $m_{\mathrm{DM}} \geq 0.5\,\mathrm{keV}$ [87].

4.1.3 Collider bound

In the Higgs portal models, where the Higgs is coupled to some new particle in the dark sector, we could in theory derive collider bounds from the LHC data, but these bounds are currently too weak to give any meaningful constraints [71, 72]. Nevertheless, in the framework where the dark sector consists of a singlet scalar and a sterile neutrino, one can derive the *unitarity bound* by demanding that the Majorana mass of the sterile neutrino $m_N = y \langle S \rangle$ is generated by the VEV of the scalar [72]: following the reasoning in [88], Ref. [72] obtains an upper bound for the Yukawa coupling:

$$y \leq \frac{m_N}{m_S} \sqrt{\frac{16\pi}{3}} \,, \tag{4.1.5}$$

and an upper bound for the Higgs portal coupling:

$$\lambda \leq y \sin^{\max}(2\alpha) \frac{|m_S^2 - m_h^2|}{2 v_{\mathrm{EW}} m_N} \,, \tag{4.1.6}$$

where v_{EW} is the VEV of the SM-Higgs and α is the mixing angle between the Higgs and the singlet scalar.

4.1.4 Dark radiation bound

Because the expansion rate of the universe depends on the amount of radiation, expansion history is delicate to any excess radiation[2]. The amount of this excess radiation, also called as dark radiation, can be bounded by the light element abundances related to big bang nucleosynthesis (BBN) and separately from the CMB power spectrum [80].

The base amount of this additional radiation (besides photons) is caused by the standard model neutrinos, and the amount of dark radiation from these active neutrinos is encoded into the effective number of neutrino N_{eff} which has the value [89]

$$N_{\mathrm{eff}} = 3.046 \,. \tag{4.1.7}$$

Deviations from this base value, ΔN_{eff}, are then bounded as:

$$\begin{cases} \Delta N_{\mathrm{eff}}^{\mathrm{BBN}} < 1 \ @\, 95\%\,\mathrm{C.L}\ [90]\,; \quad < 0.93 \ @\, 95\%\,\mathrm{C.L}\ [91]\,; \quad < 0.85 \ @\, 95\%\,\mathrm{C.L}\ [93]\,, \\ \Delta N_{\mathrm{eff}}^{\mathrm{CMB}} < 0.32 \ @\, 95\%\,\mathrm{C.L}\ [4]\,. \end{cases} \tag{4.1.8}$$

4.1.5 Domain walls

The result of spontaneous symmetry breaking of discrete symmetries can lead to a multiple degenerate minima in which the universe can settle its ground state into. If

[2] Any highly relativistic particle species will be counted in the radiation degrees of freedom.

two different parts of the universe have their ground states in different minima, the hyper-surface separating them is called a domain wall. Domain walls have not been observed [92].

Since we have assumed a discrete $\mathbb{Z}_4$ symmetry for the scalar potential (3.1.1), it would be broken by the VEV $\langle S \rangle$ of the scalar and result in two degenerate minima, this could lead to a formation of domain walls. For resolutions on how to get rid of them and more discussion see [71, 83] and references therein.

4.1.6 Momentum spectrum bound: hot, warm or cold

The concept of temperature of dark matter is somewhat unfortunate, since some scenarios in the freeze-in production of dark matter can also result a non-thermal momentum distribution for the relic abundance – as we will soon see happening under our current framework. Since the non-thermal distribution may not be well described by its average momentum, it may not be associated with a definite temperature either. Nevertheless, since the majority of dark matter models assume production mechanisms where the relic abundance is thermic, the notion of temperature has become entrenched.

The simplest and most commonly used estimator addressing the validity of a given dark matter model is the *free-streaming length* $\lambda_{\rm fs}$ which is defined as the comoving distance travelled by a particle with average velocity $\langle v \rangle$ from the time of its production[3] until today [71, 87]

$$\lambda_{\rm fs} = \int_{t_{\rm prod}}^{t_0} \frac{\langle v(t) \rangle}{a(t)} {\rm d}t = \int_{T_{\rm prod}}^{T_0} \frac{\langle v(T) \rangle}{a(T)} \frac{{\rm d}t}{{\rm d}T} {\rm d}T \,. \tag{4.1.9}$$

The free-streaming length estimates the average length scale below which cosmic structures cannot form due to motion of dark matter. The Lyman-α forest data can be used to bound the free-streaming length [94, 95] and, in the case of a thermal relic whose momentum distribution is known, this bound can be converted into a mass bound of dark matter. This is roughly estimated as [80, Chapter 4.2 and Refs. therein]

$$\lambda_{\rm fs} \sim 1\,{\rm Mpc} \frac{\rm keV}{m_{\rm DM}} \frac{\langle p_{\rm DM} \rangle}{\langle p_\nu \rangle} \,, \tag{4.1.10}$$

where $\langle p_{\rm DM} \rangle$ is the average momentum of dark matter and $\langle p_\nu \rangle \sim 1\,{\rm keV}$ is the comoving momentum of active neutrinos at the time of thermal dark matter production.

Too large free-streaming length, implying light dark matter and therefore nominally hot, would produce less small scale structure than observed, and is thus ruled out [51, 71, 72, 80, 94]. The classification of as hot, warm and cold is rather arbitrary, and

[3] As noted in [71, 72], the production time is not a well-defined input, but its arbitrary choice does not alter the results significantly.

the following scheme is the most common [71, 96]:

$$\begin{aligned} \lambda_{\text{fs}} &> 0.10\,\text{Mpc} && \text{Hot Dark Matter (ruled out)}, \\ 0.01\,\text{Mpc} < \lambda_{\text{fs}} &< 0.10\,\text{Mpc} && \text{Warm Dark Matter (possible)}, \\ \lambda_{\text{fs}} &< 0.01\,\text{Mpc} && \text{Cold Dark Matter (allowed)}. \end{aligned}$$

Because the free-streaming length relies on the notion of thermal distributions, a more sophisticated method is needed to constrain non-thermal spectrums.

A more robust way was brought forward in Ref. [72], which uses the *squared transfer function* normalised to the cold dark matter spectra:

$$\mathcal{T}^2(k) \equiv \frac{P(k)}{P_{\text{CDM}}(k)}\,, \tag{4.1.11}$$

where $P(k)$ is the linear matter power spectrum containing the spectral information of the model, $P_{\text{CDM}}(k)$ is that of the cold dark matter model, and k characters the length scale. In this form the transfer function roughly conveys how strongly the structure is suppressed compared to a perfectly cold spectrum at the scale k.

The transfer function of the model can then be compared with the one derived from the Lyman-α forest data [72, 94, 97]. Unlike the free-streaming length, the transfer function does not require a thermal momentum distribution. Nevertheless, bounds obtained for the transfer function in the literature usually do assume a thermal distribution [72]. The ideal way would be to re-evaluate the Lyman-α data with the spectra obtained from the model, but this has never been done. Instead, Ref. [72] introduces the so-called half-mode analysis by which they determine if a given spectrum is ruled out by the Lyman-α data taken from [94]. This way they try to evade the problem of comparing non-thermal transfer functions with those derived using a thermal distribution.

4.2 The parameter space with constraints

In this section the parameter space is depicted in light of the above bounds. We have fixed the scalar mass to be $m_S = 1\,\text{TeV}$. This section mostly combines the work done in Refs. [71, 72] to see what parameters are allowed before going to the numerical solutions in the next section.

Let us start with the Tremaine-Gunn limit and the abundance bound shown in the figure 4.1. The Tremaine-Gunn limit is taken to be $m_N > 0.5\,\text{keV}$, i.e. only sterile neutrino masses above $0.5\,\text{keV}$ are allowed due to Pauli blocking. The dark coloured iso-mass-lines mark where the correct relic abundance is reached at the 3σ range from the Planck observation $\Omega_{\text{DM}}h^2 = 0.1188 \pm 0.0010$ [4] for different sterile neutrino masses $m_N = 1\,\text{keV} \ldots 100\,\text{keV}$, and neighbouring dimmer colours show where a sizeable but

incorrect relic abundance is obtained, thus leaving some room for other production mechanism e.g. by active-sterile mixing via DW-mechanism discussed in the beginning of Chapter 3. The grey area marks the region where the dark matter energy density becomes too dominant $\Omega_{\mathrm{DM}} \geq 1$ "overclosing" the universe so that the present state could not have been never attained. The exact overclosure bound depends on the mass of the sterile neutrino, but that given here is the largest one in the relevant mass range [71], and anyhow its region is already ruled out by the stricter Tremaine-Gunn limit. The Tremaine-Gunn limit also divides the parameter space into the freeze-in region on left-hand side and the freeze-out region on the right-hand side.

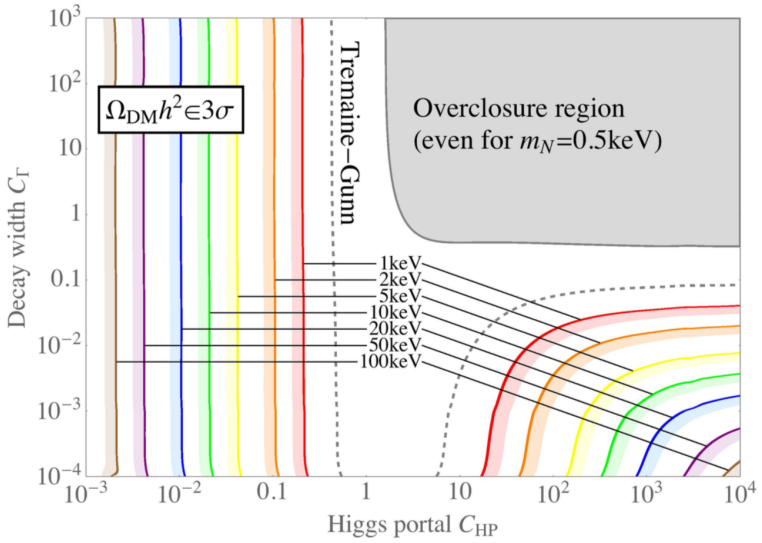

Figure 4.1: Parameter space showing the iso-mass-lines with the correct relic abundances in dark colours for different sterile neutrino masses and neighbouring dimmer lines corresponding to close-on abundance values. Dotted line shows the Tremaine-Gunn limit and the grey area marks the overclosure region. Here $m_S = 1\,\mathrm{TeV}$. Figure from [71].

Let us now move on to the momentum distribution bound. In the left panel of figure 4.2 the free-streaming length is used to estimate the structure formation. This wholly rules out the freeze-out regime on the right-hand-side as well as most of the freeze-in regime on the left-hand-side, leaving only a small section of warm sterile neutrinos produced (possibly non-thermally) by freeze-in as practicable. As discussed in the previous section, frozen-in dark matter can acquire highly non-thermal momentum distribution, so the naive free-streaming length is not able to account for its subtle features. Therefore we cannot really be sure if the warm regions in the left panel of figure 4.2 are truly allowed or not.

The same region evaluated with the half-mode analysis of squared transfer function can be seen in the right panel of figure 4.2, now expressed in terms of the Lagrangian

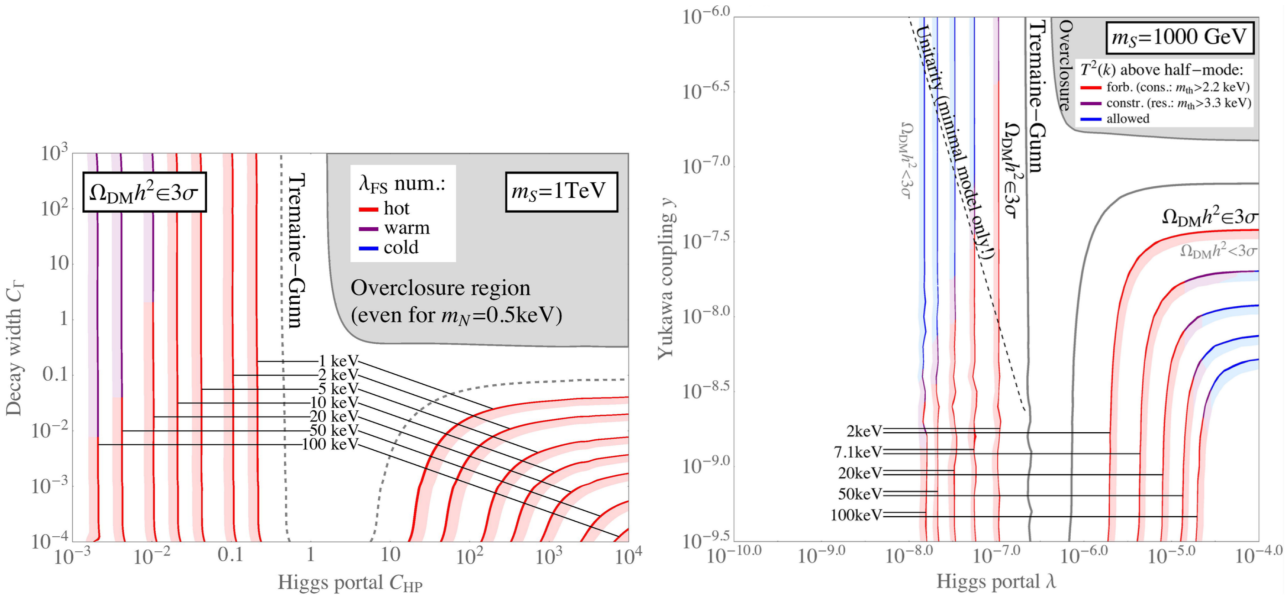

Figure 4.2: **On the left panel:** Same figure as Fig. 4.1 but now with the free-streaming length bounds. Figure from [71]. **On the right panel:** The same region as on the left but now with bounds from the half-mode analysis of squared transfer functions. Figure from [72].

parameters (λ, y). The axes are related through:

$$\begin{cases} \mathcal{C}_{\rm HP} = \frac{M_0}{m_S}\frac{\lambda^2}{16\pi^3} \\ \mathcal{C}_\Gamma = \frac{M_0}{m_S}\frac{\Gamma}{m_S} = \frac{M_0}{m_S}\frac{y^2}{16\pi} \end{cases} \Leftrightarrow \begin{cases} \lambda = \sqrt{\frac{m_S}{M_0}16\pi^3\mathcal{C}_{\rm HP}}\,, \\ y = \sqrt{\frac{m_S}{M_0}16\pi\mathcal{C}_\Gamma}\,, \end{cases} \tag{4.2.1}$$

where we used $\Gamma = y^2\frac{m_S}{16\pi}$. Now with $m_S = 1000\,\text{GeV}$, $M_0 = 7.35 g_*^{-1/2} \times 10^{18}\text{GeV}$ and $g_* = 106.5$, one can confirm that the axes do agree. Clearly the momentum distribution bound obtained from the transfer function allows big parts of regimes which the naive free-streaming length analysis ruled out. Even the freeze-out regime has an allowed part, and much of the allowed regions in general seem to be cold rather than warm – as the free-streaming length found no cold regimes at all.

The dashed line in the right panel of Fig. 4.2 marks the unitarity bound arising *if* the sterile neutrino generates a Majorana mass $m_N = y\,\langle S\rangle$ via VEV of the singlet scalar.

Finally, we consider the bounds obtained from excess (dark) radiation in the early universe. Ref. [71] found that the BBN bounds constrain the parameter space mildly, and that the CMB bound is essentially insignificant. However, in their later paper [72], the same authors note that a small error in the numerical computation of $\Delta N_{\rm eff}$ led to an overestimation of their impact. So the excluded area in the case of BBN is really larger than necessary, and in reality neither the BBN nor the CMB bound play a significant role since the relevant areas are already ruled out by the Lyman-α bound (right panel of Fig. 4.2).

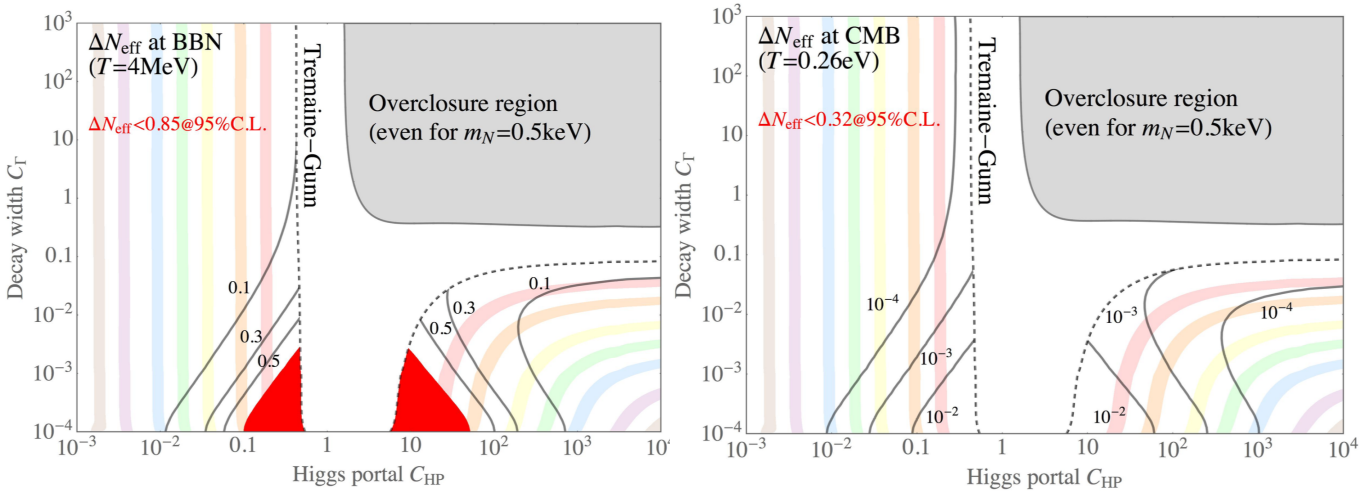

Figure 4.3: Solid grey lines mark the deviation iso-curves from the effective number of neutrinos at the time of BBN (left panel) and at the time of CMB formation (right panel) due to the excess radiation caused by solutions in that region. Red areas on the left panel are excluded by BBN and there is no significant restrictions from the CMB bounds. Both figures from [71].

4.3 The effect of assuming relativistic degrees of freedom to be constant

Even though Eq. (3.2.3) is implicitly independent of any assumption about the conservation of relativistic DOFs g_* and g_{*S}, in the very next step of using it we apply the time-temperature relation in the form $\frac{\mathrm{d}T}{\mathrm{d}t} = -HT$ which holds only at the limit of these DOF being constant.

If we allow the relativistic DOF to be dynamical, our Liouville operator (3.2.3) can be written as (see Appendix B for derivation):

$$L = \frac{H\tilde{r}}{1 + \frac{1}{3}\frac{1}{g_{*S}}\tilde{r}\frac{\mathrm{d}}{\mathrm{d}\tilde{r}}g_{*S} - \frac{1}{4}\frac{1}{g_*}\tilde{r}\frac{\mathrm{d}}{\mathrm{d}\tilde{r}}g_*}\frac{\partial}{\partial\tilde{r}}\,, \tag{4.3.1}$$

where we have defined

$$\tilde{r} \equiv \frac{m}{s^{1/3}}\,, \quad \tilde{x} \equiv \frac{a(t)}{a(t_0)}\frac{p}{s_0^{1/3}}\,. \tag{4.3.2}$$

To express Eq. (4.3.1) with our previous (cf. Eq. (3.2.2)) parameters $r = m_S/T$ and $x = p/T$[4], notice that

$$\tilde{r} = \left(\frac{2\pi^2}{45}g_{*S}\right)^{-1/3} r\,, \tag{4.3.3}$$

so that the Liouville operator becomes

$$L = \frac{Hr}{1 - \frac{1}{3}\frac{1}{g_{*S}}r\frac{\mathrm{d}}{\mathrm{d}r}g_{*S}}\frac{\partial}{\partial r}\,. \tag{4.3.4}$$

[4] x is not really needed in this

Thus by assuming the relativistic DOFs to be constant we are neglecting some contribution from those epochs where this is not valid. Nevertheless, unless there is a radical change in the relativistic DOFs (see the Fig. 4.4), the dark matter production happens so early that $\frac{1}{3}\frac{1}{g_{*S}}r \sim \frac{1}{T}$ is relatively small and the approximation of constant g_* and g_{*S} is not that bad[5]. Indeed, Ref. [71] found that the value of g_* deviates at most 20% from the assumed constant value $g_* = 106.75$ in the allowed production regimes of the parameter space, as depicted in the figure 4.5.

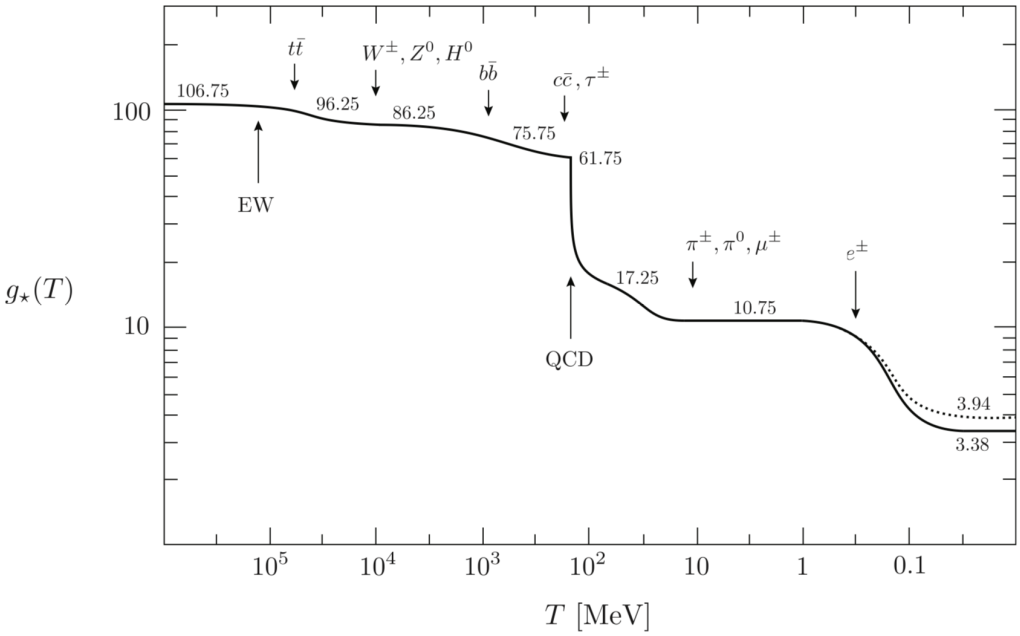

Figure 4.4: Evolution of relativistic degrees of freedom g_* (solid line) for SM particle content. Also the evolution of the effective entropy degrees of freedom g_{*S} is shown (dotted line) but it differs from the g_* only at late times. Various phase transitions causing the depletion of DOFs are also marked. Figure from [98].

[5] The relation between the change of the two DOF when the comoving entropy density is conserved $\mathrm{d}(sa^3) = 0$ is (see Appendix B):

$$\frac{1}{3}\frac{1}{g_{*S}}r\frac{\mathrm{d}}{\mathrm{d}r}g_{*S} = \frac{1}{4}\frac{1}{g_*}r\frac{\mathrm{d}}{\mathrm{d}r}g_* \,.$$

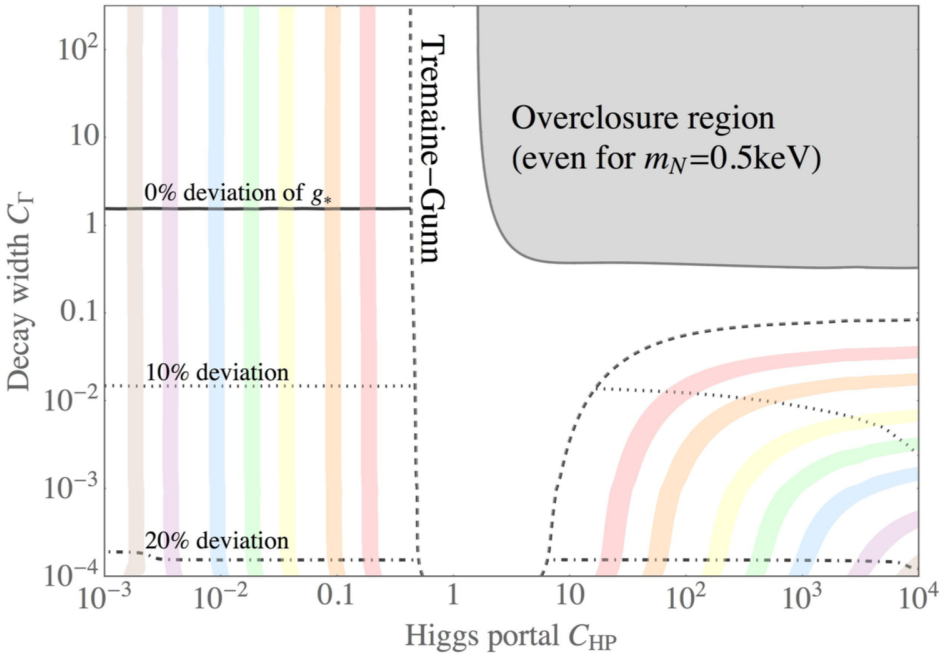

Figure 4.5: Deviation of the number of relativistic degrees of freedom from $g_* = 106.75$ at the time of sterile neutrino production. Comparing to Fig. 4.2, we see that in the allowed regimes the deviation is mild. Figure from [71].

4.4 Summary of the chapter

In this chapter, we introduced the most relevant observational constraints arising from structure formation. We motivated the robust way presented in Ref. [72] to gauge the "hotness" of dark matter by the squared transfer function $\mathcal{T}^2(k)$ and why it is a better measure for this than the usual free-streaming length $\lambda_{\rm fs}$. Then, we combined the work done in Refs. [71,72] to see the effect of these constraints for the parameter space $(\mathcal{C}_{\rm HP}, \mathcal{C}_\Gamma)$ and discussed the goodness of the $\frac{\rm d}{{\rm d}t} g_* = 0$ assumption. The most important constraints for the parameter space are found to be the Tremaine-Gunn limit, the abundance bound and the momentum distribution constraint ("hotness"). The unitarity bound arising from the assumption of the model to be minimal (in the sense that sterile neutrinos get mass via VEV of the singlet scalar) places mild restrictions, but the dark radiation bound has no significant effect.

Chapter 5

RESULTS AND NUMERICAL METHODS

5.1 The FIMP-regime

When the (effective) Higgs portal $\mathcal{C}_{\mathrm{HP}}$ is small enough, the singlet scalar never reaches thermal equilibrium with the visible sector. This happens for the Lagrangian level Higgs portal couplings $\lambda \ll 10^{-6}$ [51, 71, 72, 82, 83], or $\mathcal{C}_{\mathrm{HP}} \ll 1.4$. Hence, the FIMP-regime is the left side of the two regimes divided by the Tremaine-Gunn limit in Fig. 4.1.

In this case, the abundance of singlet scalars is gradually built via the freeze-in mechanism – we assume zero initial abundance – and all the scalars will then eventually decay to sterile neutrinos. As we do not expect a thermal distribution to arise even for the scalars, we are not expecting one for sterile neutrinos either. Due to this, the value of the (effective) decay width $\mathcal{C}_\Gamma$ is somewhat arbitrary, in the sense that, as long as all the scalars have decayed before our assumptions start to fail (at least before matter-radiation equality ($T \sim 0.8\,\mathrm{eV}$)), the correct relic abundance is obtained and the spectrum will anyhow be non-thermal. Nevertheless, if the decay from scalar to sterile neutrinos is prolonged by a small decay width, the sterile neutrinos will have less time to cool by the Hubble expansion, and thus smaller decay width values yield to a more energetic ("hotter") spectrum and are more likely to be ruled out by the structure formation.

Let us now show the obtained yields, $Y_i \equiv n_i/s$, and spectra $f_N(x,r)$, $f_S(x,r)$ for four different freeze-in scenarios. Chosen parameter values in the FIMP-regime are (for fixed $m_s = 1000\,\mathrm{GeV}$) listed in the table 5.1. The mass of the sterile neutrino is set to be to be $\sim 2\,\mathrm{keV}, 7\,\mathrm{keV}$ and $100\,\mathrm{keV}$ to depict the effect of light and massive sterile neutrino (within the keV-scale).

In figure 5.1 we show the yields for the singlet scalar, the sterile neutrino and for the thermal equilibrium distribution functions. As expected, the scalar never reaches

equilibrium with the visible sector due to its feeble interactions with the Higgs. In the panels (a), (b) of Fig. 5.1, the scalar starts to decay to sterile neutrinos long before it actually freezes in. In the panel (c) decays are so fast that all scalar will almost immediately decay to a very light ($\sim 2\,\mathrm{keV}$) sterile neutrinos, and this particular case is actually ruled out by the momentum bound. Also in Fig. 5.1, the panel (d) shows interesting behaviour, as when $T \sim m_S$ the scalar seems to be frozen in, when in reality it has also just started to decay to sterile neutrinos, so that we get a pseudo-frozen in state where the interactions with the Higgs provide just the right amount of new scalars to replace the decaying ones. This lasts until the Boltzmann suppression depletes the Higgs number density to negligible values and rest of the scalars decay off.

In figure 5.2 we show the momentum distribution functions for the singlet scalar. Following the colour coding from lighter colours to darker colours we can trace the time evolution. As we have assumed the initial abundance to be zero, we see that the distribution gradually builds up until the decays to sterile neutrinos start to tend the distribution back towards zero. In the panel (d) of Fig. 5.2 we see that the distribution is frozen to its peak value until it finally decays off, as described above.

In figure 5.3 we show the momentum distribution functions for the sterile neutrino. They start from zero (lighter colours) and build up to their final form (darkest line). In the panels (b) and (d) the distributions resemble the thermal distribution, whereas in the panels (a) and (c) the deviation from the thermal distribution are evident. This non-thermal behaviour is more extreme in the WIMP region, which we cover in the next section.

	Lagrangian parameters		*effective parameters* ($m_S = 1\,\mathrm{TeV}$)		
Figure label	λ	y	$\mathcal{C}_{\mathrm{HP}}$	$\mathcal{C}_{\Gamma}$	m_N
(a)	5.64×10^{-8}	3.43×10^{-6}	4.57×10^{-3}	1.67×10^{2}	$7\,\mathrm{keV}$
(b)	5.7×10^{-8}	1.12×10^{-7}	4.66×10^{-3}	1.78×10^{-1}	$7\,\mathrm{keV}$
(c)	8.1×10^{-8}	5.9×10^{-5}	9.5×10^{-3}	5×10^{4}	$\sim 2\,\mathrm{keV}$
(d)	1.44×10^{-8}	5.1×10^{-9}	2.98×10^{-4}	3.69×10^{-4}	$100\,\mathrm{keV}$

Table 5.1: List of parameters used in each figure in the FIMP-regime. The figure label points the given data to the correct panel in the figures 5.1, 5.2 and 5.3, which show yields and momentum distributions for the singlet scalar and the sterile neutrino respectively. The Lagrangian level parameters are taken from the right panel of Fig. 4.2 and transformed to effective parameters using Eq. (4.2.1). This causes small discrepancy, as the right panel in Fig. 4.2 accounts for the change in relativistic degrees of freedom while the left panel does not.

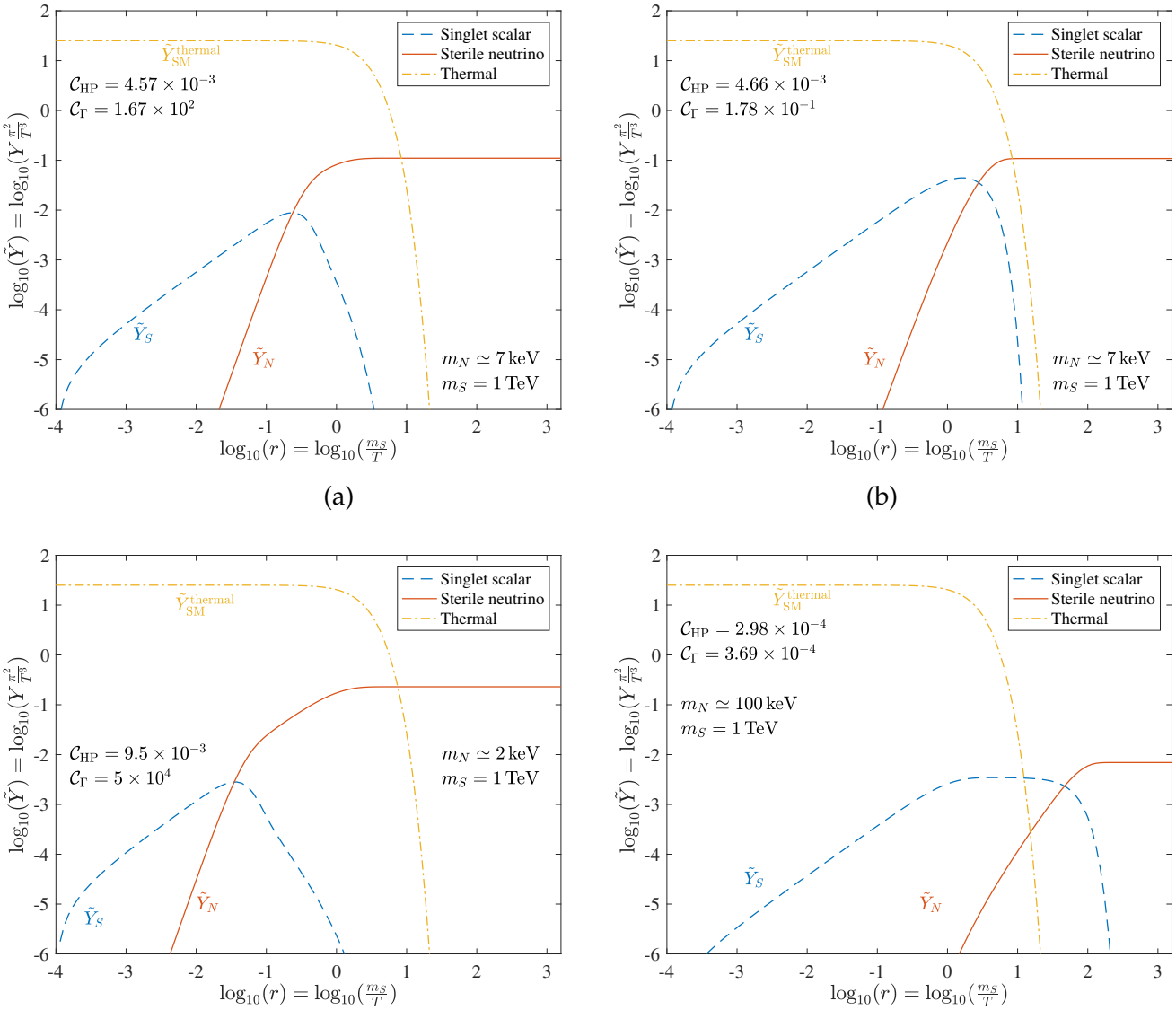

Figure 5.1: Yields for different points in the parameter space $(\mathcal{C}_{\rm HP}, \mathcal{C}_\Gamma)$ listed in the Table 5.1 for the singlet scalar (dashed blue line), sterile neutrino (solid red line), and thermal distribution (yellow dash-dotted line) in a log-log scale.

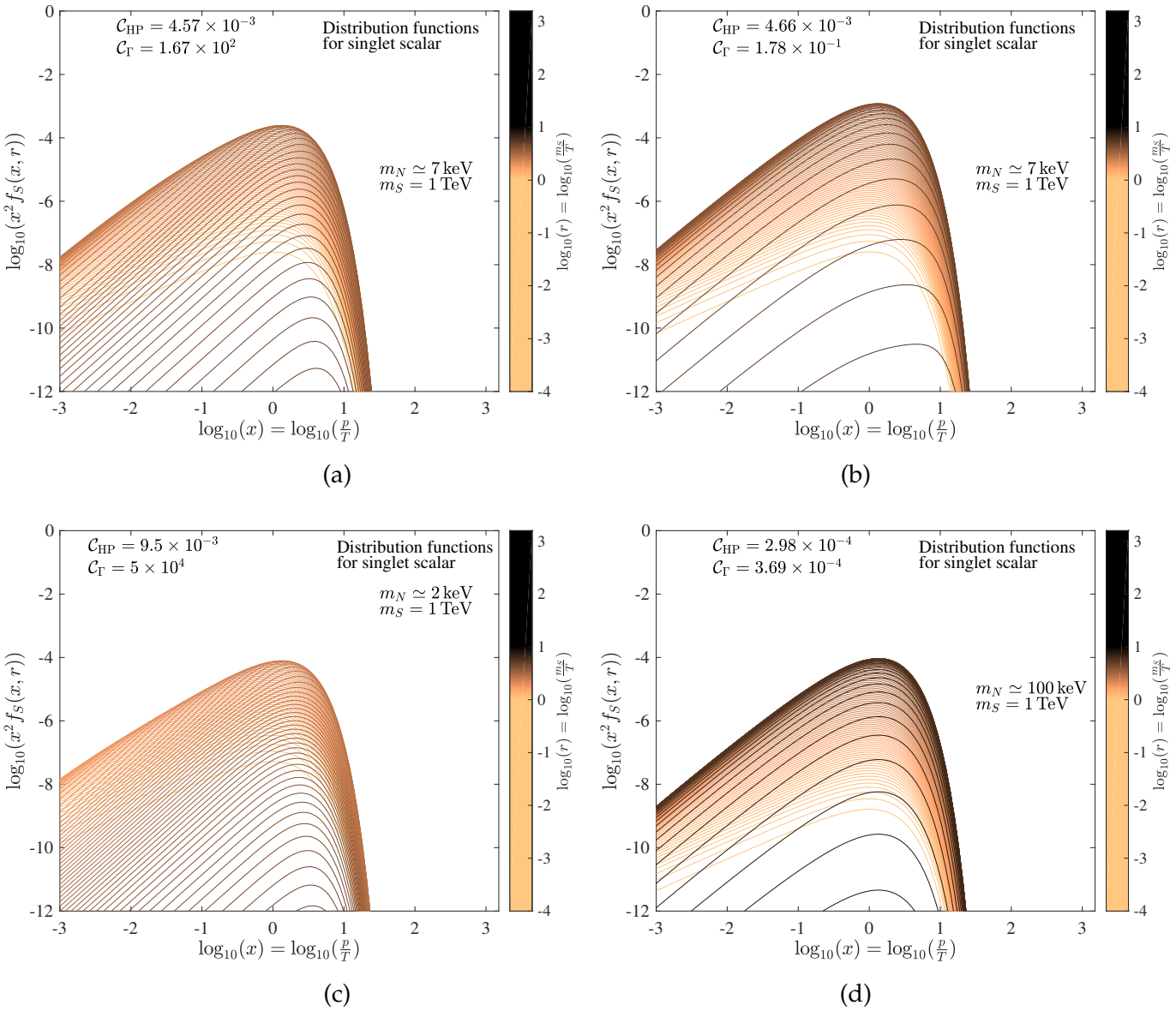

Figure 5.2: Singlet scalar distribution functions for different points in the parameter space $(\mathcal{C}_{\rm HP}, \mathcal{C}_\Gamma)$ listed in the Table 5.1. The colour bar shows the evolution of time, with lighter colours representing earlier times and dark colours later times.

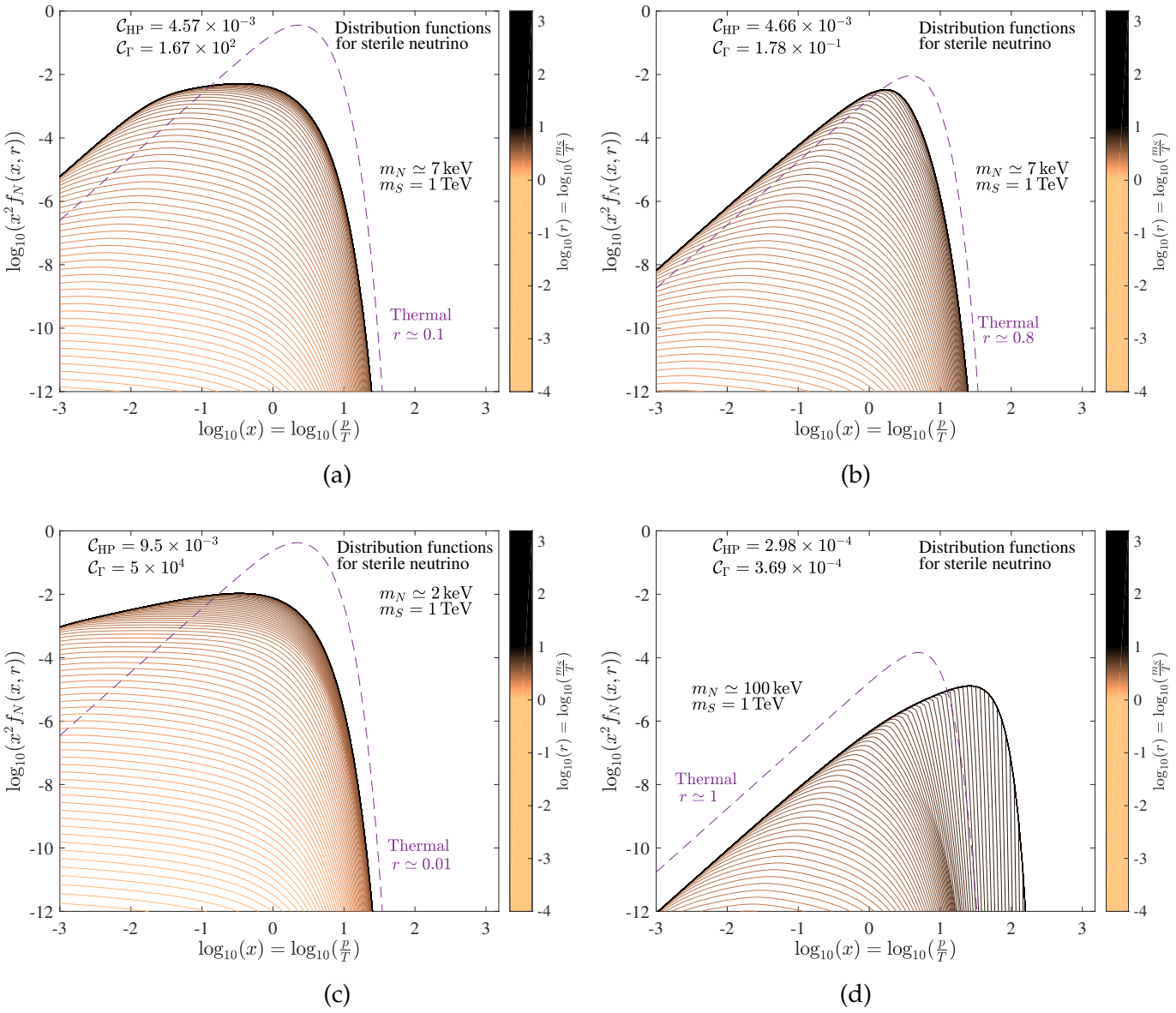

Figure 5.3: Sterile neutrino distribution functions for different points in the parameter space $(\mathcal{C}_{\rm HP}, \mathcal{C}_\Gamma)$ listed in the Table 5.1. The colour bar shows the evolution of time, with lighter colours representing earlier times and dark colours later times. A scaled thermal distribution (violet dashed line) is shown for comparison.

5.2 The WIMP-regime

For a large enough Higgs portal $\mathcal{C}_{\rm HP}$ the singlet scalar reaches thermal equilibrium with the visible sector. This happens for the Lagrangian level Higgs portal couplings $\lambda \gg 10^{-6}$ [51, 71, 72, 82, 83], or $\mathcal{C}_{\rm HP} \gg 1.4$. The WIMP-regime corresponds to the right side of the two allowed regimes in Fig. 4.1. The singlet scalar stays equilibrated until its interaction rate with the Higgs is dwarfed by the Hubble expansion and it freezes out. Depending on the decay width $\mathcal{C}_\Gamma$, sterile neutrinos are gradually accumulated from decays of scalars.

In the case of a large decay width, the sterile neutrinos are produced early on as soon as scalars become abundant. This scenario is depicted in the panel (a) of Fig. 5.4, which shows the obtained yields $Y \equiv n/s$ for the singlet scalar and sterile neutrino. The majority of sterile neutrinos are produced before the scalar freezes out from the standard model heat bath, and only a negligible abundance is produced from the left-over frozen out scalars. Corresponding momentum distributions for the singlet scalar and sterile neutrino are shown in the (a)-panels of Figs. 5.5 and 5.6, respectively. There the scalar distribution first becomes thermal and, upon freezing out (the more dense region of lines near the midway), diminishes to zero. The neutrino distribution on the other hand starts from zero and builds up as the momenta and the rest energy of singlet scalars are transferred to those of sterile neutrinos. The non-thermal statistics of sterile neutrinos is reflected in as the nascent second peak in the momentum distribution function.

In the case of an intermediate decay width, a large portion of sterile neutrinos is formed early on from decays of thermalised scalars, but there may also be a large abundance production from frozen out residue scalars. This is depicted in the panels (b) and (c) of Fig. 5.4. Corresponding momentum distributions for the singlet scalar and sterile neutrino are shown in the (a) and (b) -panels of Figs. 5.5 and 5.6, respectively. The coincidental shapes of scalar momentum distributions arise from their congruent equilibrium periods. The highly non-thermal statistics of sterile neutrinos is clearly evident in the panel (b) of Fig. 5.6. The panel(c) deviates only mildly from the thermal distribution.

In the case of a small decay width, a majority of sterile neutrinos are produced at late times after the scalar has frozen out. Because of this the dark matter relic abundance is determined by the interactions within the dark sector. This is typical in the dark freeze-out production mechanism which is depicted in the panel (d) of Fig. 5.4. There, most of the sterile neutrino abundance is produced at $\log_{10}\left(\frac{m_s}{T}\right) \gtrsim 2$. In dark freeze-out scenarios, the singlet scalar may also act as a dark matter together with the sterile neutrino. Nevertheless, for simplicity we have assumed the singlet scalar to be unstable i.e. that all relic scalars will eventually decay to sterile neutrinos. The final neutrino distribution function in the panel (d) of Fig. 5.6 is highly non-thermal so it is

hard to determine its suitability to the structure formation. Nevertheless, this particular case is determined to be too "hot" by the half-mode analysis.

	Lagrangian parameters		*effective parameters* ($m_S = 1\,\mathrm{TeV}$)		
Figure label	λ	y	$\mathcal{C}_{\mathrm{HP}}$	$\mathcal{C}_{\Gamma}$	m_N
(a)	5.1×10^{-5}	2.0×10^{-8}	3.7×10^{3}	5.7×10^{-3}	$7\,\mathrm{keV}$
(b)	1.0×10^{-4}	5.2×10^{-9}	1.4×10^{4}	3.8×10^{-4}	$100\,\mathrm{keV}$
(c)	2.4×10^{-5}	1.8×10^{-8}	8.3×10^{2}	4.6×10^{-3}	$100\,\mathrm{keV}$
(d)	8.35×10^{-5}	2.66×10^{-9}	1.0×10^{4}	1.0×10^{-4}	$> 100\,\mathrm{keV}$

Table 5.2: List of parameters used in each figure in the WIMP-regime. The figure label points the given data to the correct panel in the figures 5.4, 5.5 and 5.6, which show the yields and the momentum distributions for the singlet scalar and the sterile neutrino respectively. The Lagrangian level parameters are taken from the right panel of Fig. 5.2 and transformed to effective parameters using Eq. (4.2.1). This causes small discrepancy, as the right panel in Fig. 4.2 accounts for the change in relativistic degrees of freedom while the left panel does not.

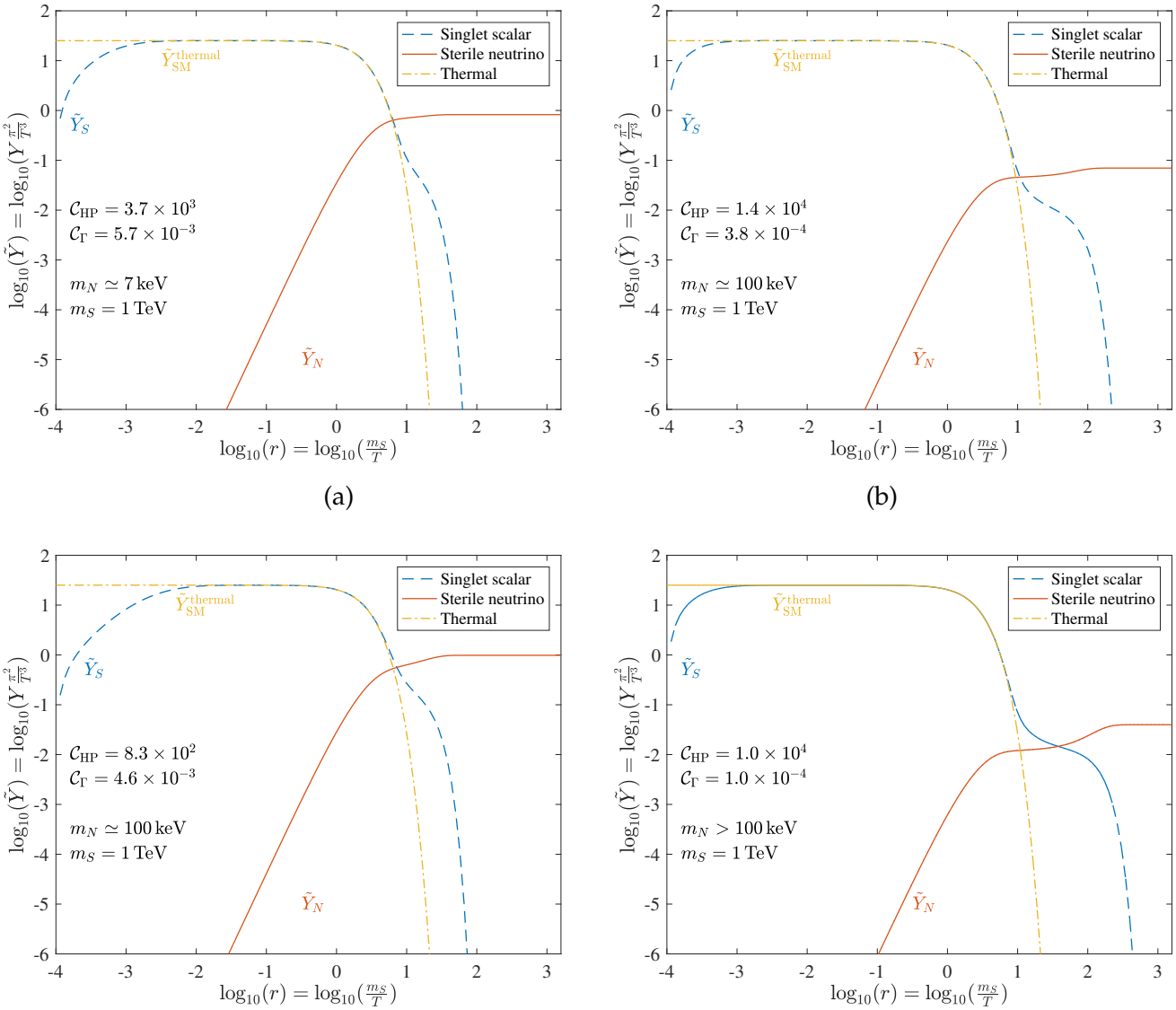

Figure 5.4: Yields for different points in the parameter space $(\mathcal{C}_{\rm HP}, \mathcal{C}_\Gamma)$ listed in the Table 5.2 for the singlet scalar (dashed blue line), sterile neutrino (solid red line), and thermal distribution (yellow dash-dotted line) in a log-log scale.

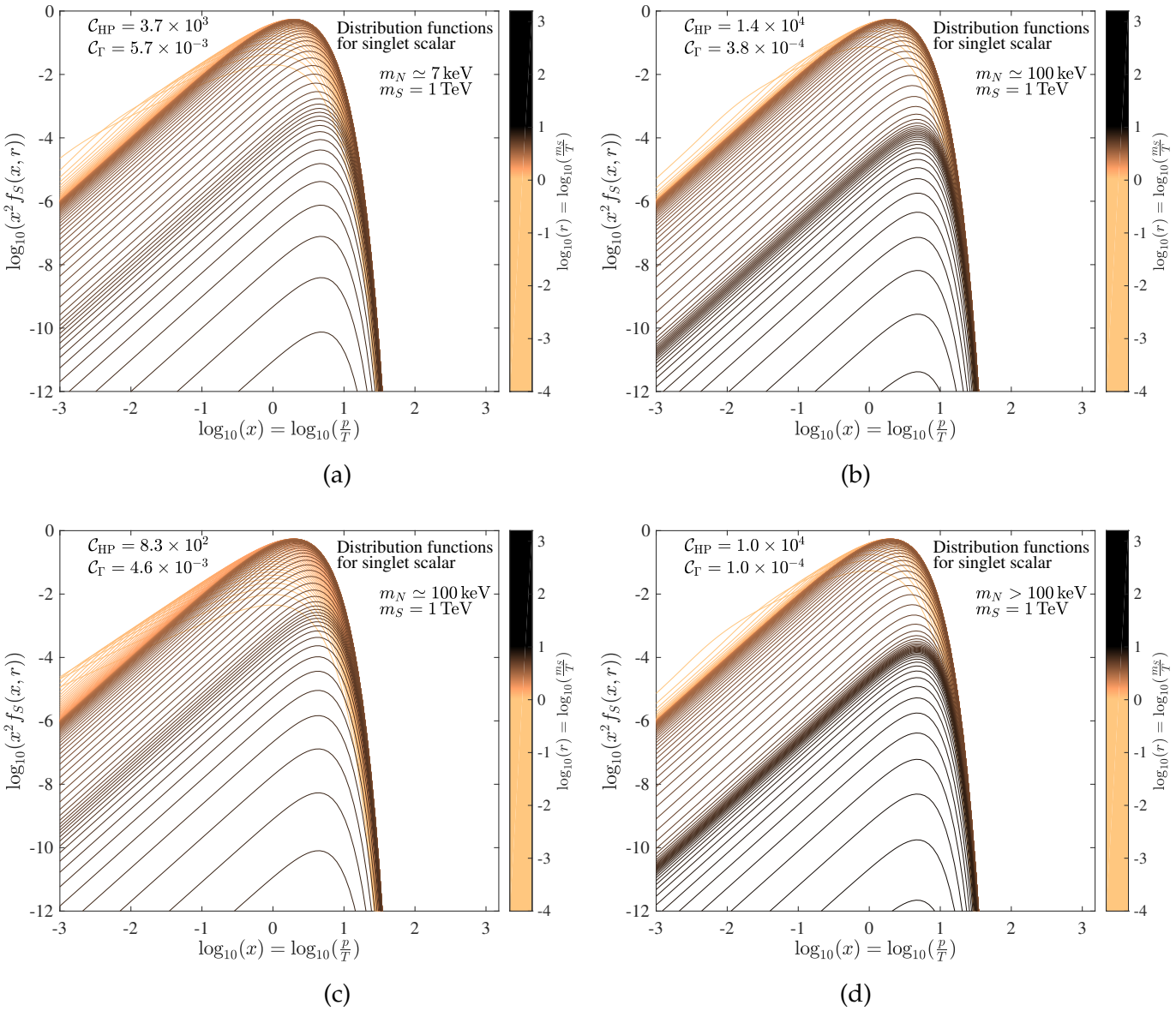

Figure 5.5: Singlet scalar distribution functions for different points in the parameter space $(\mathcal{C}_{\rm HP}, \mathcal{C}_\Gamma)$ listed in the Table 5.2. The colour bar shows the evolution of time, with lighter colours representing earlier times and dark colours later times.

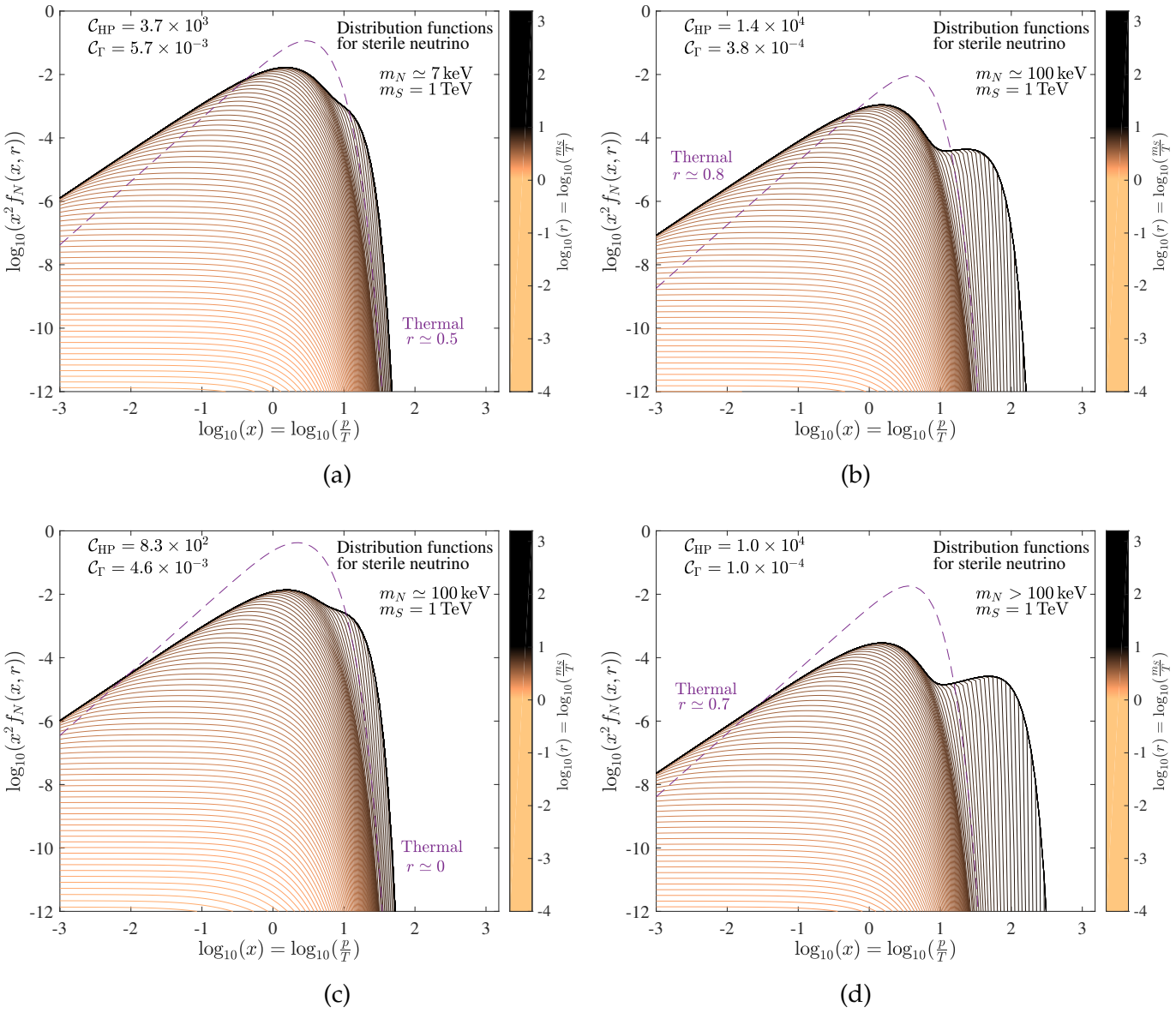

Figure 5.6: Sterile neutrino distribution functions for different points in the parameter space $(\mathcal{C}_{\rm HP}, \mathcal{C}_{\Gamma})$ listed in the Table 5.2. The colour bar shows the evolution of time, with lighter colours representing earlier times and dark colours later times. A scaled thermal distribution (violet dashed line) is shown for comparison.

5.3 Numerical methods

Rather than solving equations (3.2.10) and (3.2.11) separately, we treat them as a set of coupled non-linear partial intergo-differential equations. This way, our implementation also covers scenarios when the Boltzmann equations cannot be uncoupled. We use the similar method as described in the Ref. [72] and discretise the momentum variable $x \to x_i$ for $i \in \{1, \ldots, M\}$, where M is some sufficiently large momentum cut-off parameter. This way, the original integro-differential equations for $f_{S,N}(x, r)$ transform into a system of coupled modes of the same integro-differential equations $f^i_{S,N}(r)$:

$$\begin{cases} \frac{\mathrm{d}f^i_S(r)}{\mathrm{d}r} = \mathcal{C}_{\mathrm{HP}} \frac{e^{-\sqrt{x_i^2+r^2}}}{\sqrt{x_i^2+r^2}} r K_1(r) - \mathcal{C}_{\mathrm{HP}} \frac{f^i_S(r)}{\sqrt{x_i^2+r^2}} \left[\Delta x \sum_{j=1}^{M} \frac{x_j^2}{\sqrt{x_j^2+r^2}} f^j_S(r) \right] - \mathcal{C}_\Gamma \frac{r^2}{\sqrt{x_i^2+r^2}} f^i_S(r)\,, \\ \frac{\mathrm{d}f^i_N(r)}{\mathrm{d}r} = 2\mathcal{C}_\Gamma \frac{r^2}{x_i^2} \Delta x \sum_{j \in \mathcal{I}_i(r)} \frac{x_j}{\sqrt{x_j^2+r^2}} f^j_S(r)\,, \qquad \forall i \in \{1, \ldots, M\}, \end{cases} \tag{5.3.1}$$

where the index group $\mathcal{I}_i(r) \equiv \{k \in \mathbb{N} : \left| x_i - \frac{r^2}{4x_i} \right| \leq k \leq M\}$. Because the momentum integrals couple to every momentum mode, equation (5.3.1) must be solved with a fixed r for all modes x_i simultaneous. Furthermore, due to the stiffness (meaning rapid variation in its modes) of this system of equations, most ordinary differential equation (ODE) algorithms fail to perform in all parts of the parameter space.

MATLAB's built-in toolbox *ODE suite* [99] offers the *ode15s* solver for stiff problems, which we have used to solve the system (5.3.1). The full code with a brief description is given in the Appendix D.

5.4 Summary of the chapter

In this chapter the solutions of Eqs. (3.2.10) and (3.2.11) in the two regimes of Fig. 4.2 are presented. These regimes correspond to the FIMP production of the scalar on the left-hand side and the WIMP production of the scalar on the right-hand side of Fig. 4.2. For each regime the yields and momentum distribution functions for the singlet scalar and the sterile neutrino are solved in four differing points. The obtained solutions are presented in Figs. 5.1, 5.2 and 5.3 for the FIMP scenario, and in Figs. 5.4, 5.5 and 5.6 for the WIMP scenario. Also, the numerical methods are briefly described and the full MATLAB implementation is given in Appendix D.

A notable result, although not a new one (as it was first found in 2015 by Merle and Totzauer [71]) in this chapter is the recovery of the momentum distribution function for the sterile neutrino, which is demonstrated to be highly non-thermal in some cases.

Chapter 6

CONCLUSIONS AND OUTLOOK

In this work, we reviewed the evidence for dark matter, known discrepancies of the ΛCDM model, and the basic mechanisms for producing the observed dark matter abundance. We augmented the standard model with a dark sector consisting of a singlet scalar field and a right-handed sterile neutrino field, and hypothesised that the relic abundance of sterile neutrinos comprises the observed dark matter abundance. We constrained the Higgs portal coupling λ, acting between the singlet scalar and the SM Higgs, and the Yukawa coupling y, acting between the singlet scalar and the sterile neutrino, with observations from cosmology and structure formation. We found that the freeze-in, freeze-out, and their variant production mechanisms for the dark sector particles can originate from the constrained parameter space $\{\lambda, y\}$. We solved the momentum distribution function of sterile neutrinos from the system of Boltzmann equations, and, as a by-product, obtained the momentum distribution function for the singlet scalar. The distribution functions are solved in various points of the parameter space, which give rise to differing production mechanisms. We found that, in addition to offering a realistic dark matter candidate, the sterile neutrino can attain a highly non-thermal momentum distribution in the process.

The non-thermal nature of sterile neutrinos makes it hard to assess their suitability to structure formation, as all constraints currently found from literature assume thermal behaviour from the dark matter candidate. The obtained distribution functions could be used to reanalyse the structure formation constraints obtained from the Lyman-α data, but that has not yet been done.

We intent to build upon this work by including the back scatterings from sterile neutrinos to singlet scalars $NN \to S$ and $NN \leftrightarrow SS$, as well as the number changing processes within the particle species, such as $NNNN \to NN$. We also intent to revamp the dark sector to contain three right-handed sterile neutrinos and a singlet scalar. This is motivated by the *Neutrino Minimal Standard Model* (νMSM) [100–102] and models similar to it [103, 104]. The νMSM contains three sterile-neutrinos with masses below the electroweak scale, and can explain simultaneously the active neutrino oscillations, dark matter and baryon asymmetry of the universe [101]. In the νMSM the sterile

neutrinos are produced from their mixing with the active neutrinos. In the models including an additional singlet scalar, like [104], sterile neutrinos can be produced by decays of the scalar, and the methodology of this work is directly applicable.

Appendices

Appendix A

Covariant Boltzmann equation

The Boltzmann equation describes the evolution of the phase space distribution function $f_i = f_i(t, \mathbf{x}, \mathbf{p})$ and in its classical form is defined as:

$$L[f_i] = C[f_i]\,, \tag{A.0.1}$$

where the term on the left-hand side is the Liouville term defined as

$$L[f_i] = \frac{\mathrm{d}}{\mathrm{d}t} f_i = \left(\frac{\partial}{\partial t} + \frac{\mathrm{d}x_j}{\mathrm{d}t} \frac{\partial}{\partial x_j} + \frac{\mathrm{d}p_j}{\mathrm{d}t} \frac{\partial}{\partial p_j} \right) f_i\,, \tag{A.0.2}$$

and the term on the right-hand side is the collision term containing all the particle number changing interaction processes. In the relativistic theory we have $f_i = f_i(p^\alpha, x^\alpha)$ so that

$$\mathrm{d}f_i = \frac{\partial f_i}{\partial x^\alpha} \mathrm{d}x^\alpha + \frac{\partial f_i}{\partial p^\alpha} \mathrm{d}p^\alpha\,. \tag{A.0.3}$$

Choose the affine parameter λ so that on a curve $x^\mu(\lambda)$ we have $\frac{\mathrm{d}t}{\mathrm{d}\lambda} = m\gamma = E$, allowing us to write:

$$\frac{\mathrm{d}x^\alpha}{\mathrm{d}\lambda} = p^\alpha = (m\gamma, m\gamma v^i) = (E, p^i)\,, \tag{A.0.4}$$

and then the geodesic equation gives

$$\frac{\mathrm{d}^2 x^\alpha}{\mathrm{d}\lambda^2} = \frac{\mathrm{d}p^\alpha}{\mathrm{d}\lambda} = -\Gamma^\alpha{}_{\beta\gamma} \frac{\mathrm{d}x^\beta}{\mathrm{d}\lambda} \frac{\mathrm{d}x^\gamma}{\mathrm{d}\lambda} = -\Gamma^\alpha{}_{\beta\gamma} p^\beta p^\gamma\,. \tag{A.0.5}$$

Now the Liouville term can be written as

$$L[f_i] = \frac{\mathrm{d}f_i}{\mathrm{d}\lambda} = \left(p^\alpha \frac{\partial}{\partial x^\alpha} - \Gamma^\alpha{}_{\beta\gamma} p^\beta p^\gamma \frac{\partial}{\partial p^\alpha} \right) f_i \tag{A.0.6}$$

where Γ is the Christoffel symbol. In the FLRW universe the distribution function is homogeneous and isotropic

$$\frac{\partial f}{\partial x^j} = 0\,, \qquad \frac{\partial f}{\partial p^j} = 0\,, \tag{A.0.7}$$

and the Christoffel symbols are

$$\Gamma^0{}_{ij} = a\dot{a}\delta_{ij}\,, \qquad \Gamma^i{}_{0j} = \frac{\dot{a}}{a}\delta_{ij}\,. \tag{A.0.8}$$

The Liouville term in FLRW universe then becomes

$$\begin{aligned} L[f_i] &= \left(p^0 \frac{\partial}{\partial x^0} - \Gamma^0{}_{ij} p^i p^j \frac{\partial}{\partial p^0} \right) f_i \\ &= \left(E \frac{\partial}{\partial t} - a\dot{a} p^2 \frac{\partial}{\partial E} \right) f_i \\ &= \left(E \frac{\partial}{\partial t} - H p_{\mathrm{L}}^2 \frac{\partial}{\partial E} \right) f_i \\ &= E_i \left(\frac{\partial}{\partial t} - H p_{\mathrm{L}} \frac{\partial}{\partial p_{\mathrm{L}}} \right) f_i \,, \end{aligned} \tag{A.0.9}$$

where in the third line the *comoving* 3-momentum p is switched back to the *local* 3-momentum p_{L} by using $p_{\mathrm{covariant}} = p_{\mathrm{local}}/a$ and in the last line the usual dispersion $E^2 = p_{\mathrm{L}}^2 + m^2$ is applied. The usual convention is to divide the $E = E_i$ to be included into the collision terms in the right-hand side of the Boltzmann equation (A.0.1). This gives us the final form of the Liouville operator:

$$\boxed{\tilde{L}[f_i] \equiv \frac{L[f_i]}{E} = \left(\frac{\partial}{\partial t} - H p \frac{\partial}{\partial p} \right) f_i} \,. \tag{A.0.10}$$

The general form of the collision term for an event $\psi + a + b + \cdots \longrightarrow \alpha + \beta + \ldots$ is

$$\boxed{\begin{aligned} \tilde{C}[f_\psi] = \frac{1}{2E_\psi} \int \big[&(d\Pi_a d\Pi_b \ldots)(d\Pi_\alpha d\Pi_\beta \ldots)(2\pi)^4 \times \\ &\times \delta^{(4)}(p_\psi + p_a + p_b + \cdots - p_\alpha - p_\beta - \ldots) \times \\ &\times |\mathcal{M}|^2 f_\psi f_a f_b \ldots (1 \pm f_\alpha)(1 \pm f_\beta) \ldots \big] \,, \end{aligned}} \tag{A.0.11}$$

where $d\Pi_a \equiv \frac{g_a \mathrm{d}^3 p_a}{(2\pi)^3 2E_{p_a}}$ is the phase space measure and g_a is the number of internal degrees of freedom of particle species "a".

Appendix B

Liouville operator in new variables

Taking the Eq. (A.0.10) as a starting point, we have

$$\tilde{L} = \frac{\partial}{\partial t} - Hp\frac{\partial}{\partial p}\,. \tag{B.0.1}$$

In the radiation dominated universe the Hubble parameter $H = \frac{1}{2t}$. Combining this with the first Friedmann equation (1.1.5) along with the expressions (1.2.6) and (1.2.9) for energy- and entropy densities, we get

$$H = \frac{1}{2t} = \sqrt{\frac{8\pi G}{3}\frac{\pi^2}{30}}g_{*s}^{1/2}T^2\,. \tag{B.0.2}$$

Then define a change of variables from t and p to r and x such that

$$\begin{cases} r = r(t)\,, \\ x = x(t,p)\,, \end{cases} \quad \text{and explicitly, let} \quad \begin{cases} r \equiv \frac{m}{s^{1/3}}\,, \\ x \equiv \frac{a(t)}{a_0}\frac{p}{s_0^{1/3}}\,, \end{cases} \tag{B.0.3}$$

where we have chosen to use entropy as a basic variable instead of temperature ($s^{1/3} \sim T$), t_0 is some reference time and $a_0 = a(t_0)$, $s_0 = s(t_0)$. Using the chain rule we get

$$\begin{aligned} \tilde{L} &= \frac{\partial r}{\partial t}\frac{\partial}{\partial r} + \frac{\partial x}{\partial t}\frac{\partial}{\partial x} - Hp\left(\cancel{\frac{\partial r}{\partial p}\frac{\partial}{\partial r}}^{\,0} + \frac{\partial x}{\partial p}\frac{\partial}{\partial x}\right) \\ &= \frac{\partial r}{\partial t}\frac{\partial}{\partial r} + \underbrace{\left[\frac{\partial x}{\partial t} - Hp\frac{\partial x}{\partial p}\right]}_{\frac{a}{a_0}\frac{Hp}{s_0^{1/3}} - \frac{a}{a_0}\frac{Hp}{s_0^{1/3}} = 0}\frac{\partial}{\partial x} \\ &= \frac{\partial r}{\partial t}\frac{\partial}{\partial r}\,. \end{aligned} \tag{B.0.4}$$

Lets express this explicitly in terms of entropy and energy degrees of freedom. From (B.0.2) together with (1.2.9) we get the time-entropy relation

$$t = C\frac{g_{*s}^{2/3}}{g_*^{1/2}}s^{-2/3}\,, \tag{B.0.5}$$

where $C = \frac{1}{2}\left(\frac{\pi^2}{90}\right)^{-1/2}\left(\frac{2\pi^2}{45}\right)^{2/3}$. From this follows

$$\frac{\mathrm{d}s}{\mathrm{d}t} = \frac{3Hs}{s\frac{g'_{*s}}{g_{*s}} - \frac{3}{4}\frac{g'_*}{g_*} - 1}\,, \tag{B.0.6}$$

where the derivatives on the right hand side are with respect to s. Now using $\frac{\partial r}{\partial t} = -\frac{s^{-1}r}{3}\frac{\partial s}{\partial t}$ we find

$$\tilde{L} = \frac{Hr}{1 + \frac{1}{3}\frac{1}{g_{*s}}r\frac{\mathrm{d}}{\mathrm{d}r}g_{*s} - \frac{1}{4}\frac{1}{g_*}r\frac{\mathrm{d}}{\mathrm{d}r}g_*}\frac{\partial}{\partial r}\,. \tag{B.0.7}$$

To relate this with our earlier variable $\tilde{x} = p/T$ and $\tilde{r} = m/T$ notice that

$$r = \left(\frac{2\pi^2}{45}\right)^{-1/3} g_* s^{-1/3}\tilde{r}\,. \tag{B.0.8}$$

Before applying this to (B.0.7), notice that from the entropy conservation $d(sa^3) = 0$ follows $\frac{1}{3}\frac{1}{g_{*s}}r\frac{\mathrm{d}}{\mathrm{d}r}g_{*s} - \frac{1}{4}\frac{1}{g_*}r\frac{\mathrm{d}}{\mathrm{d}r}g_* = 0$. After simplifying the denominator and using the transformation (B.0.8), we get

$$\tilde{L} = \frac{H\tilde{r}}{1 - \frac{1}{3}\frac{1}{g_{*s}}\tilde{r}\frac{\mathrm{d}}{\mathrm{d}r}g_{*s}}\frac{\partial}{\partial\tilde{r}}\,. \tag{B.0.9}$$

Appendix C

Collision terms

This Appendix goes through the computation of collision terms showing very explicitly all intermediate steps.

C.1 $C^S_{hh\to SS}$

Starting from the (A.0.11) we have:

$$C^s_{h(q)h(q')\to s(p)s(p')}(p) = \frac{1}{2E_p}\int \frac{d^3p'}{(2\pi)^3 2E_{p'}}\frac{d^3q}{(2\pi)^3 2E_q}\frac{d^3q'}{(2\pi)^3 2E_{q'}}|\mathcal{M}|^2(2\pi)^4\times \\ \times\,\delta^{(4)}\big(q+q'-p-p'\big)f_h(q)f_h(q')\big(1\pm f_s(p)\big)\big(1\pm f_s(p')\big)\,. \quad \text{(C.1.1)}$$

Then we do following the approximations/assumptions:

- Neglect bosonic/fermionic structure (initially $f_s \ll 1$), i.e. $(1\pm f_s)\approx 1$.
- Assume Higgses to be in equilibrium, so that $f_h(q)f_h(q') = f_h^{\rm eq}(q)f_h^{\rm eq}(q') = e^{-(E_q+E_{q'})/T} = e^{-(E_p+E_{p'})/T} = f_s^{\rm eq}(q)f_s^{\rm eq}(q')$, where we have used energy conservation to express Higgs distributions in terms of scalar distributions at equilibrium.
- Matrix element $|\mathcal{M}|^2$ includes only tree-level diagrams and is constant.

Furthermore, we apply the known result for the (lorentz invariant) 2-body phase space integral[1]:

$$\int \frac{d^3q}{(2\pi)^3 2E_q}\frac{d^3q'}{(2\pi)^3 2E_{q'}}(2\pi)^4\delta\big(q+q'-p-p'\big) = \frac{1}{4\pi}\frac{P_{qq'}(s)}{\sqrt{s}} \\ = \frac{1}{4\pi}\frac{1}{\sqrt{s}}\frac{1}{2}\frac{\sqrt{\big[s-\cancel{(m_h-m_h)^2}\big]\big[s-(m_h+m_h)^2\big]}}{\sqrt{s}} \\ = \frac{1}{4\pi}\frac{1}{2}\sqrt{\frac{s-4m_h^2}{s}}\,. \quad \text{(C.1.2)}$$

[1]Note that this integral becomes available in Eq. (C.1.1) only after we have assumed equilibrium statistics for Higgses (phase space integrals will not operate on Higgs' distribution functions if we write them in terms of scalar distribution functions).

Here s is the Mandelstam variable $s \equiv (p^\mu + p'^\mu)^2 = (q^\mu + q'^\mu)^2$, which can be written in terms of initial or final parameters. After applying these considerations to Eq. (C.1.1) we end up to

$$\begin{aligned} \therefore \quad C^s_{h(q)h(q')\to s(p)s(p')}(p) &= \frac{|\mathcal{M}|^2}{2E_p}\int \frac{d^3p'}{(2\pi)^3 2E_{p'}}\frac{1}{4\pi}\frac{1}{2}\sqrt{\frac{s-4m_h^2}{s}} f_s^{\mathrm{eq}}(p) f_s^{\mathrm{eq}}(p') \\ &= \frac{|\mathcal{M}|^2}{2^4(2\pi)^4}\frac{e^{-E_p/T}}{E_p} 2\pi \int_{-1}^{1} \mathrm{d}(\cos\theta) \int_0^\infty \mathrm{d}p' \, \frac{p'^2}{E_{p'}}\sqrt{\frac{s-4m_h^2}{s}} e^{-E_{p'}/T} \,. \end{aligned} \tag{C.1.3}$$

Using the change of variables to

$$\begin{cases} x \equiv \frac{p}{T} & \left(x' \equiv \frac{p'}{T}\right) \,, \\ r \equiv \frac{m_s}{T} \,, \end{cases} \tag{C.1.4}$$

which has the following effect for terms in (C.1.3):

$$E_p = T\sqrt{x^2+r^2} \,, \tag{C.1.5}$$

$$s = (E_p + E_{p'})^2 - (\mathbf{p}+\mathbf{p}')^2 = T^2\left(\sqrt{x^2+r^2}+\sqrt{x'^2+r^2}\right)^2 - T^2(\mathbf{x}+\mathbf{x}')^2 \,, \tag{C.1.6}$$

$$\Rightarrow \sqrt{\frac{s-4m_h^2}{s}} = \sqrt{\frac{\left(\sqrt{x^2+r^2}+\sqrt{x'^2+r^2}\right)^2 - (\mathbf{x}+\mathbf{x}')^2 - 4\xi^2 r^2}{\left(\sqrt{x^2+r^2}+\sqrt{x'^2+r^2}\right)^2 - (\mathbf{x}+\mathbf{x}')^2}}, \qquad \text{where } \xi \equiv \frac{m_h}{m_s} \,, \tag{C.1.7}$$

$$\int_0^\infty \mathrm{d}p' \, p'^2 = T^3 \int_0^\infty \mathrm{d}x' \, x'^2 \,, \tag{C.1.8}$$

we establish[2]:

$$\begin{aligned} \therefore \quad C^s_{h(q)h(q')\to s(p)s(p')}(p) &= \frac{|\mathcal{M}|^2}{2^4(2\pi)^4}\frac{e^{-\sqrt{x^2+r^2}}}{\sqrt{x^2+r^2}} T \times \\ &\times \underbrace{2\pi \int_{-1}^{1} \mathrm{d}(\cos\theta) \int_0^\infty \mathrm{d}x' \, \frac{x'^2 e^{-\sqrt{x'^2+r^2}}}{\sqrt{x'^2+r^2}} \sqrt{\frac{\left(\sqrt{x^2+r^2}+\sqrt{x'^2+r^2}\right)^2 - (\mathbf{x}+\mathbf{x}')^2 - 4\xi^2 r^2}{\left(\sqrt{x^2+r^2}+\sqrt{x'^2+r^2}\right)^2 - (\mathbf{x}+\mathbf{x}')^2}}}_{\equiv \mathcal{F}(x,r,\xi)} \end{aligned} \tag{C.1.9}$$

$$= \frac{|\mathcal{M}|^2}{256\pi^4}\frac{e^{-\sqrt{x^2+r^2}}}{\sqrt{x^2+r^2}} T \cdot \mathcal{F}(x,r,\xi) \,. \tag{C.1.10}$$

Then we must sort out the outcome of the function $\mathcal{F}(x,r,\xi)$ as it is defined in Eq. (C.1.9). We will assume that the scalar mass exceeds the Higgs mass so that $\xi = \frac{m_h}{m_s} \ll 1$.

[2]Note that the parameter ξ in (C.1.7) arises due to forced cancellations of T^2 between numerator and denominator.

In this limit the function $\mathcal{F}$ is easy to compute, because then the last square root term in it simply becomes to unity. Lets now compute $\mathcal{F}$ in the above limit:

$$\begin{aligned}
\mathcal{F}(x, r, \xi \ll 1) &= 2\pi \int_{-1}^{1} \mathrm{d}(\cos\theta) \int_{0}^{\infty} \mathrm{d}x' \frac{x'^2 e^{-\sqrt{x'^2+r^2}}}{\sqrt{x'^2+r^2}} \sqrt{1} \\
&\quad \text{making the change of variables to } x'^2 + r^2 \equiv a^2 \Rightarrow \int_0^\infty \to \int_r^\infty \text{ and } \mathrm{d}x = \frac{\mathrm{d}a\, a}{\sqrt{a^2-r^2}} \\
&= 4\pi \int_r^\infty \mathrm{d}a (a^2 - r^2)^{1/2} e^{-a} \\
&\quad \text{and again, set } a \equiv tr \to \int_r^\infty \to \int_1^\infty \\
&= 4\pi r^2 \int_1^\infty \mathrm{d}t\, (t^2-1)^{1/2} e^{-tr} \\
&= 4\pi r \cdot K_1(r)\,. \qquad \text{(C.1.11)}
\end{aligned}$$

Where we've recognised the first modified Bessel function of the second kind

$$K_n(z) \equiv \frac{\sqrt{\pi}}{(n-\frac{1}{2})!} \left(\frac{1}{2}z\right)^n \int_1^\infty e^{-zx} (x^2-1)^{n-\frac{1}{2}}\, \mathrm{d}x\,. \qquad \text{(C.1.12)}$$

To conclude this section; our end result is

$$\boxed{C^s_{h(q)h(q')\to s(p)s(p')} = \frac{|\mathcal{M}|^2}{256\pi^4} \frac{e^{-\sqrt{x^2+r^2}}}{\sqrt{x^2+r^2}} T \cdot \mathcal{F}(x, r)}\,. \qquad \text{(C.1.13)}$$

where we've assumed $m_s \gg m_h$ and hence $\mathcal{F}(x, r) = \mathcal{F}(x, r, \xi \ll 1) = \mathcal{F}(r)$ is given by Eq. (C.1.11).

C.2 $C^S_{SS\to hh}$

With the knowledge of above section we may now quickly write down next collision term to be

$$C^s_{s(p)s(p')\to h(q)h(q')}(p) = -\frac{1}{2E_p}\int \frac{d^3p'}{(2\pi)^3 2E_{p'}} \overbrace{\frac{d^3q}{(2\pi)^3 2E_q}\frac{d^3q'}{(2\pi)^3 2E_{q'}}(2\pi)^4\delta^{(4)}\left(q+q'-p-p'\right)}^{\frac{1}{4\pi}\frac{1}{2}\sqrt{\frac{s-4m_h^2}{s}}} \times$$
$$\times \left|\mathcal{M}\right|^2 f_s(p) f_s(p') \underbrace{\left(1\pm f_h(q)\right)}_{\approx 1}\underbrace{\left(1\pm f_h(q')\right)}_{\approx 1}$$

$$= -\frac{\left|\mathcal{M}\right|^2}{4\pi 2^2}\frac{1}{(2\pi)^3 2}\frac{f_s(p)}{E_p}\cdot 2\pi\int_{-1}^{1}\mathrm{d}(\cos\theta)\int_0^\infty \mathrm{d}p'\,\frac{p'^2}{E_{p'}}\sqrt{\frac{s-4m_h^2}{s}}f_s(p')$$

change variables as in (C.1.4)

$$= -\frac{\left|\mathcal{M}\right|^2}{2^4(2\pi)^4}\frac{f_s(x,r)}{\sqrt{x^2+r^2}}T\times$$
$$\times 2\pi\int_{-1}^{1}\mathrm{d}(\cos\theta)\int_0^\infty \mathrm{d}x'\,\frac{x'^2}{\sqrt{x'^2+r^2}}\sqrt{\frac{\left(\sqrt{x^2+r^2}+\sqrt{x'^2+r^2}\right)^2-(\mathbf{x}+\mathbf{x}')^2-4\xi^2r^2}{\left(\sqrt{x^2+r^2}+\sqrt{x'^2+r^2}\right)^2-(\mathbf{x}+\mathbf{x}')^2}}f_s(x',r)$$
$$\equiv -\frac{\left|\mathcal{M}\right|^2}{256\pi^4}\frac{f_s(x,r)}{\sqrt{x^2+r^2}}T\int \mathrm{d}^3x'\,\mathcal{G}(x',x,r,\xi)f_s(x',r)\,, \tag{C.2.1}$$

where

$$\mathcal{G}(x',x,r,\xi) \equiv \frac{1}{\sqrt{x'^2+r^2}}\sqrt{\frac{\left(\sqrt{x^2+r^2}+\sqrt{x'^2+r^2}\right)^2-(\mathbf{x}+\mathbf{x}')^2-4\xi^2r^2}{\left(\sqrt{x^2+r^2}+\sqrt{x'^2+r^2}\right)^2-(\mathbf{x}+\mathbf{x}')^2}} \tag{C.2.2}$$

$$\Rightarrow \quad \mathcal{G}(x',x,r,\xi\ll 1) = \mathcal{G}(x',r) = \frac{1}{\sqrt{x'^2+r^2}}\,. \tag{C.2.3}$$

Thus our final result is

$$\boxed{C^s_{s(p)s(p')\to h(q)h(q')} = -\frac{\left|\mathcal{M}\right|^2}{256\pi^4}\frac{f_s(x,r)}{\sqrt{x^2+r^2}}T\int \mathrm{d}^3x'\,\mathcal{G}(x',r)f_s(x',r)}\,, \tag{C.2.4}$$

where we've assumed $m_s \gg m_h$ and hence $\mathcal{G}(x',r)$ is given by (C.2.3).

C.3 $C^S_{S\to NN}$

We have the usual definition for the decay width Γ

$$\Gamma(a\to b_1+b_2+\cdots+b_n) \equiv \frac{g_a}{2m_a}\left(\prod_{i=1}^n\int\frac{g_i\mathrm{d}^3p_i}{(2\pi)^3 2E_i}\right)(2\pi)^4\delta^{(4)}\left(p_a-\sum_{i=1}^n p_i\right)\left|\mathcal{M}\right|^2. \tag{C.3.1}$$

The collision term now looks like[3]

$$C^s_{s(p)\to N(k)N(k')}(p) =$$
$$-\frac{1}{2E_p}\int \frac{2d^3k}{(2\pi)^3 2E_k}\frac{2d^3k}{(2\pi)^3 2E_{k'}}|\mathcal{M}|^2(2\pi)^4\delta^{(4)}\left(p-k-k'\right)f_s(p)\underbrace{\left(1\pm f_N(k)\right)}_{\approx 1}\underbrace{\left(1\pm f_N(k')\right)}_{\approx 1}$$

using the equation (C.3.1)

$$= -f_s(p)\Gamma\frac{m_s}{E_p}\,. \tag{C.3.2}$$

Then we still want to express this in the language of parameters x and r. Since

$$\frac{m_s}{E_p} = \frac{m_s}{T\sqrt{x^2+r^2}} = \frac{T}{m_s}\left(\frac{m_s}{T}\right)^2\frac{1}{\sqrt{x^2+r^2}} = T\frac{r^2}{\sqrt{x^2+r^2}}\frac{1}{m_s}\,, \tag{C.3.3}$$

we get

$$\boxed{C^s_{s(p)\to N(k)N(k')}(p) = -T\frac{r^2}{\sqrt{x^2+r^2}}\frac{\Gamma}{m_s}f_s(x,r)}\,. \tag{C.3.4}$$

C.4 $C^N_{S\to NN}$

The matrix element for this process can be found to be

$$|\mathcal{M}|^2 = \frac{1}{2}y^2 k\cdot k' = \frac{1}{2}y^2 E_k E_{k'}\left[1-\frac{\mathbf{k}\cdot\mathbf{k}'}{E_k E_{k'}}\right]\,, \tag{C.4.1}$$

which should then be integrated over the phase space. This messy integral can be avoided by noticing that the *tree-level matrix element is constant* due to 4-momentum conservation:

$$\begin{aligned} p &= k+k' \\ \Rightarrow p^2 &= (k+k')^2 \\ \Leftrightarrow \underbrace{E_p^2-|\mathbf{p}|^2}_{m_s^2} &= \underbrace{E_k^2-|\mathbf{k}|^2}_{m_N^2}+\underbrace{E_{k'}^2-|\mathbf{k}'|^2}_{m_N^2}+2k\cdot k' \\ \Leftrightarrow k\cdot k' &= \frac{1}{2}\left(m_s^2-2m_N^2\right) = \text{constant}. \end{aligned}$$

Hence

$$\underline{|\mathcal{M}|^2 = \frac{1}{2}y^2 k\cdot k' = \frac{1}{4}y^2(m_s^2-2m_N^2) = \text{constant}.} \tag{C.4.2}$$

[3]The minus sign comes from the fact that we are tracking the scalar distribution and this process lessens the amount of scalars in the system. Also the factors of 2 in the integral measure are spin DOF of netrino.

Now the collision term is[4]

$$C^N_{s(p)\to N(k)N(k')}(k) =$$
$$2\times\frac{1}{2E_k}\int\frac{2\mathrm{d}^3k'}{(2\pi)^3 2E_{k'}}\frac{\mathrm{d}^3p}{(2\pi)^3 2E_p}2|\mathcal{M}|^2(2\pi)^4\delta^{(4)}\left(p-k-k'\right)f_s(p)\underbrace{\left(1\pm f_N(k)\right)}_{\approx 1}\underbrace{\left(1\pm f_N(k')\right)}_{\approx 1}$$
$$= 2\frac{2|\mathcal{M}|^2}{2E_k}\frac{(2\pi)^4}{(2\pi)^6 2}\int\frac{\mathrm{d}^3k'}{E_{k'}}\frac{\mathrm{d}^3p}{E_p}\delta\left(E_p-E_k-E_{k'}\right)\delta^{(3)}\left(\mathbf{p}-\mathbf{k}-\mathbf{k}'\right)f_s(p)$$

using d^3k' to the last delta function sets $\mathbf{k}'=\mathbf{p}-\mathbf{k}$

$$= 2\frac{2|\mathcal{M}|^2}{2E_k}\frac{(2\pi)^4}{(2\pi)^6 2}\int\frac{\mathrm{d}^3p}{E_pE_{|\mathbf{p}-\mathbf{k}|}}\delta\left(E_p-E_k-E_{|\mathbf{p}-\mathbf{k}|}\right)f_s(p)$$

using the delta function identity to write $\delta\left(E_p-E_k-E_{|\mathbf{p}-\mathbf{k}|}\right)=\delta\left(\cos\theta-\cos\theta_0\right)\frac{\left(E_{|\mathbf{p}-\mathbf{k}|}\right)_{|_{\theta=\theta_0}}}{|\mathbf{p}||\mathbf{k}|}$

where θ_0 denotes the root $\cos\theta_0=\frac{2E_pE_k-m_s^2}{2|\mathbf{p}||\mathbf{k}|}$ for the equation $E_p-E_k-E_{|\mathbf{p}-\mathbf{k}|}=0$,

i.e. θ is the angle between $\mathbf{p}$ and $\mathbf{k}$ and thus the same angle which now comes from opening d^3p.

$$= 2\frac{2|\mathcal{M}|^2}{2E_k}\frac{(2\pi)^4}{(2\pi)^6 2}2\pi\int_{-1}^{1}\mathrm{d}(\cos)\int_0^\infty\mathrm{d}p\frac{|\mathbf{p}|^2}{E_p|\mathbf{p}||\mathbf{k}|}\frac{\left(E_{|\mathbf{p}-\mathbf{k}|}\right)_{|_{\theta=\theta_0}}}{E_{|\mathbf{p}-\mathbf{k}|}}\delta\left(\cos\theta-\cos\theta_0\right)f_s(p)$$

noting that the integral over $\cos\theta$ gives zero unless $\cos\theta\in[-1,1]$, we can perform the integral over the delta function if we restrict the momentum p so that $\cos\theta$ is always in that interval.

$$= 2\frac{2|\mathcal{M}|^2}{2E_k}\frac{(2\pi)^4}{(2\pi)^6 2}2\pi\int_{p_{\min}}^{p_{\max}}\mathrm{d}p\frac{|\mathbf{p}|}{E_p|\mathbf{k}|}f_s(p)\,. \tag{C.4.3}$$

I have still left the integral limits of p implicit, but will add steps on how to compute them later. So far we have accomplished

$$C^N_{s(p)\to N(k)N(k')}(k)=\frac{2|\mathcal{M}|^2}{4\pi E_k|\mathbf{k}|}\int_{p_{\min}}^{p_{\max}}\mathrm{d}p\frac{|\mathbf{p}|}{E_p}f_s(p)\,. \tag{C.4.4}$$

Then change variables to

$$\begin{cases} x\equiv\frac{k}{T} & \left(x'\equiv\frac{p}{T}\right) \\ r\equiv\frac{m_s}{T} & \end{cases}, \tag{C.4.5}$$

[4]Number of neutrinos in the process is changed by 2 so thus the first factor of 2. Then there is a factor of 2 in the integral measure due to spin DOF of neutrino. The factor of 2 in-front of the matrix element is due to symmetric particles in the final state $S\to NN$ i.e. because the same decay width $\Gamma_{s\to NN}$ is used in (C.3.2) and (C.4.10), even though in the latter we integrate over just one of the final states.

and since our scalar is massive compared to Higgs, it is also massive compared to neutrinos, hence we can approximate

$$E_k = T\sqrt{x^2 + \left(\frac{m_N}{m_s}\right)^2 r^2} \approx Tx\,, \tag{C.4.6}$$

$$|\mathcal{M}|^2 = \frac{1}{4}y^2(m_s^2 - 2m_N^2) \approx \frac{y^2 m_s^2}{4}\,. \tag{C.4.7}$$

Furthermore, if we compute the decay width for this process using Eq. (C.3.1), where $|\mathcal{M}|^2$ is now given in Eq. (C.4.7), we get[5]

$$\Gamma = \frac{y^2 m_s}{16\pi}\,. \tag{C.4.8}$$

Thus we can express our matrix element (C.4.7) as

$$|\mathcal{M}|^2 = 4\pi m_s \Gamma\,. \tag{C.4.9}$$

So after applying the change of variables and taking above considerations into account, we end up to

$$C^N_{s(p)\to N(k)N(k')} = \frac{2r\Gamma}{x^2}\int_{x'_{\min}}^{x'_{\max}} \mathrm{d}x' \frac{x'}{\sqrt{x'^2 + r^2}} f_s(x', r)\,. \tag{C.4.10}$$

Because we still want to include *the effective decay width* $\mathcal{C}_\Gamma \equiv \frac{M_0}{m_s}\frac{\Gamma}{m_s}$ into this, we get our end result to be

$$\boxed{C^N_{s(p)\to N(k)N(k')} = \frac{Tm_s}{M_o} 2\mathcal{C}_\Gamma \frac{r^2}{x^2}\int_{x'_{\min}}^{x'_{\max}} \mathrm{d}x' \frac{x'}{\sqrt{x'^2 + r^2}} f_s(x', r)}\,, \tag{C.4.11}$$

where the quantity $\frac{Tm_s}{M_o}$ is later cancelled by $\frac{\mathrm{d}T}{\mathrm{d}r}\frac{\mathrm{d}t}{\mathrm{d}T} = \frac{M_0}{m_s}\frac{1}{T}$ coming from the left hand side of the Boltzmann equation.

Lets now address the question of integral limits for p in (C.4.3) which then gives the limits also for (C.4.11). So we must somehow employ condition $\cos\theta_0 \in [-1, 1]$ to the

[5]Note that one can apply Eq. (C.1.2) straight away here and use $s = E_p^2 = m_s^2$ and then $m_s \gg m_n$ makes the square root to become unity.

integral limits of p. From $E_p - E_k - E_{|\mathbf{p}-\mathbf{k}|} = 0$ we get

$$
\begin{aligned}
|\cos\theta_0| = \left|\frac{2E_pE_k - m_s^2}{2|\mathbf{p}||\mathbf{k}|}\right| &\leq 1 \\
\Rightarrow \qquad (2E_pE_k - m_s^2)^2 &\leq 4p^2k^2 \\
\Leftrightarrow \qquad -E_k^2 - 4\Big(\underbrace{\frac{m_N}{m_s}}_{\approx 0}\Big)^2 p^2 + E_kE_p - \frac{m_s^2}{4} &\geq 0 \\
\Leftrightarrow \qquad E_p &\geq \frac{4E_k^2 + m_s^2}{4E_k} \\
\Rightarrow \qquad p^2 &\geq \left(\frac{4E_k^2 - m_s^2}{4E_k}\right)^2 \\
\Rightarrow \qquad p &\geq \left|k - \frac{m_s^2}{4k}\right| \equiv p_{\min}\,,
\end{aligned}
\tag{C.4.12}
$$

where in the last step we've approximated $E_k = \sqrt{k^2 + m_n^2} \approx k$. This also gives us that $p_{\max} = \infty$. Thus the limits in Eq. (C.4.11) are

$$
\begin{cases}
x'_{\min} = \left|x - \frac{r^2}{4x}\right|\,, \\
x'_{\mathrm{mac}} = \infty\,.
\end{cases}
\tag{C.4.13}
$$

Appendix D

MATLAB implementation

- **main.m** defines used parameters ($\mathcal{C}_{\mathrm{HP}}, \mathcal{C}_{\Gamma}$, discretisation and initial conditions for f_S and f_N). After computing the distributions it computes the yields Y_S and Y_N and plots the obtained results. It has the following dependencies:
  - **Boltzmann.m** is the right-hand side of Eq. (5.3.1). It takes in the parameter values $\mathcal{C}_{\mathrm{HP}}$, $\mathcal{C}_{\Gamma}$ and the discretised vector x and its interval Δx as well as the fixed r value and the distributions $f_S^i(r)$ and $f_N^i(r)$ concatenated into vector $F = [f_S(r) \quad f_N(r)]^{\mathrm{T}} = \left[f_S^1(r), \ldots, f_S^M(r), f_N^{M+1}(r), \ldots, f_N^{M+M}(r)\right]^{\mathrm{T}}$. It has the following dependencies:
    - **hhTOss_s.m** is the function for $C^S_{hh\to SS}$
    - **ssTOhh_s.m** is the function for $C^S_{SS\to hh}$
    - **sTOnn_s.m** is the function for $C^S_{s\to NN}$
    - **sTOnn_n.m** is the function for $C^N_{s\to NN}$

D.1 main.m

keywordstyle

```
clear;
clc;
close all;
format long;
%
totalTimer = tic;
%% Solve distributions (in logarithmic scale)
solveTimer = tic;

hx = 0.06; % Discretisation interval for x
hr = 0.06; % Discretisation interval for r
x = -3.0:hx:3.2;     % [0,inf] -> [10^(-3), 10^3.2] = [0.001, 1585]
r = -4:hr:3.2;
```

```
Chp = 8.3*10^(2);    % Higgs portal
Cg = 4.6*10^(-3);    % Decay width

% Initial conditions ( assume zero initial abundance)
%FS0 = exp(-sqrt(10.^(2*x(:)) + 10^(2*r(1)))); % Uncomment for thermal
%initial abundance for scalar and comment the one below.
FS0 = zeros(numel(x),1);
FN0 = zeros(numel(x),1);
F0 = vertcat(FS0,FN0);

options = odeset('RelTol',1e-13,'AbsTol',1e-18,'NonNegative',1);
[r,F] = ode15s(@(r,F) Boltzmann(F,x,r,hx,Cg,Chp),r, F0,options);

FS = F(:,1:numel(x));
FN = F(:,numel(x)+1:end);

solveTime = toc(solveTimer);
disp(['Distributions solved in: ' num2str(solveTime) ' seconds'])
%% Figures
fig = figure;
figure(fig)
cmap = colormap(flipud(copper(length(r)))); % Define colormap:
%   copper,hot,summer,winter,autumn,spring are fine.
set(groot,'DefaultAxesColorOrder',cmap); % Set above colormap
%   to be the default one.
close(fig);

fig1 = figure;
figure(fig1);
hold on;
box on;
xlim([x(1),x(end)]) % Set range for x-axis in the plot.
ylim([-12,0]); % Set range for y-axis in the plot.
cmap = colormap(flipud(copper(length(r)))); % Define colormap:
%   copper,hot,summer,winter,autumn,spring are good.
set(groot,'DefaultAxesColorOrder',cmap); % Set above colormap
%   to be the default one.
cbar = colorbar; % Turn the colorbar on which shows the scaling
%   of the colors.
set(cbar, 'ylim', [r(1) r(end)]);%Define axis for the above colorbar.
ylabel(cbar, '$\log_{10}(r)=\log_{10}(\frac{m_S}{T})$',...
    'interpreter','latex','FontSize',16);
plot(x,log10(FS(:,:).*(10.^(2*x))));
title(['Chp = ' num2str(Chp,'%.e'), '       Cg = ' num2str(Cg,'%.e')]);
set(fig1,'name','Scalar distribution function','numbertitle','off');
xlabel('$\log_{10}(x)=\log_{10}(\frac{p}{T})$','interpreter','latex');
ylabel('$\log_{10}(x^2f_S(x,r))$','interpreter','latex');
set(gca,'FontSize',16,'FontName','Times');
```

```
hold off

fig2 = figure;
figure(fig2);
hold on;
box on;
xlim([x(1),x(end)]) % Set range for x-axis in the plot.
ylim([-12,0]); % Set range for y-axis in the plot.
cmap = colormap(flipud(copper(length(r)))); % Define colormap:
%   copper,hot,summer,winter,autumn,spring are good.
set(groot,'DefaultAxesColorOrder',cmap); % Set above colormap
%   to be the default one.
cbar = colorbar; % Turn the colorbar on which shows the scaling
%   of the colors.
set(cbar, 'ylim', [r(1) r(end)]); % Define axis for the above colorbar.
ylabel(cbar, '$\log_{10}(r)=\log_{10}(\frac{m_S}{T})$','interpreter', ...
    'latex','FontSize',16);
plot(x,log10(FN(1:end,:).*(10.^(2*x))));
title(['Chp = ' num2str(Chp,'%.e'), '       Cg = ' num2str(Cg,'%.e')]);
set(fig2,'name','Neutrino distribution function','numbertitle','off');
xlabel('$\log_{10}(x)=\log_{10}(\frac{p}{T})$','interpreter','latex');
ylabel('$\log_{10}(x^2f_N(x,r))$','interpreter','latex');
set(gca,'FontSize',16,'FontName','Times');
hold off

%% Compute yield
yieldTimer = tic;
YS = zeros(1,length(r));
YN = zeros(1,length(r));
Ythermal = zeros(1,length(r));
Fthermal = exp(-sqrt(10.^(2*x) + 10.^(2*r)));
% dont include i=1 values becuse for some reason FN(r,x) contains numerical
% inconsistency at r=r(1) values.
for i = 1:length(r)
    YS(i) = hx*sum(4.*pi.*10.^(2.*x(:)).*log(10).*10.^x(:).*FS(i,:)');

    YN(i) = hx*sum(4.*pi.*10.^(2.*x(:)).*log(10).*10.^x(:).*FN(i,:)');

    Ythermal(i) = ...
        hx*sum(4.*pi.*10.^(2.*x(:)).*log(10).*10.^x(:).*Fthermal(i,:)');
end
clear i;
yieldTime = toc(yieldTimer);
disp(['Yield computed in: ' num2str(yieldTime) ' seconds'])


% Reset color settings for the last plot
 co =[0 0.4470 0.7410;
```

```
      0.8500  0.3250  0.0980;
      0.9290  0.6940  0.1250;
      0.4940  0.1840  0.5560;
      0.4660  0.6740  0.1880;
      0.3010  0.7450  0.9330;
      0.6350  0.0780  0.1840];
 set(groot,'defaultAxesColorOrder',co)

fig3 = figure;
figure(fig3);
hold on;
box on;
xlim([r(1) r(end)]);
ylim([-6 2]);
plot(r,log10(YS),'--','LineWidth',1,'MarkerSize',1);
plot(r,log10(YN),'-','LineWidth',1);
plot(r,log10(Ythermal),'-.','LineWidth',1);
xlabel('$\log_{10}(r)=\log_{10}(\frac{m_S}{T})$','interpreter','latex');
ylabel('$\log_{10}(\tilde{Y}) = \log_{10}(Y\frac{\pi^2}{T^3})$',...
    'interpreter','latex');
legend('Singlet scalar','Sterile neutrino','Thermal');
set(gca,'FontSize',16,'FontName','Times');
hold off


totalTime = toc(totalTimer);
disp(['All computed. Total time: ' num2str(totalTime) ' seconds'])
```

D.2 Boltzmann.m

keywordstyle

```
function dF = Boltzmann( F,x,r,hx,Cg,Chp )
%BOLTZMANN contains the collision terms of the Botlzmann equation.
%   F = vector containing FS and FN

    FS = F(1:numel(x));
    %FN = F(numel(x)+1:end); %Uncomment for coupled equations

    %Scalar PDE
    dFS = (log(10).*10.^r).*(hhTOss_s( Chp,10.^x,10.^r ) ...
        + ssTOhh_s( Chp,10.^x,10.^r,FS,hx ) ...
        + sTOnn_s( Cg,10.^x,10.^r,FS ));

    %Neutrino PDE
    dFN = (log(10).*10.^r).*sTOnn_n( Cg,10.^x,10.^r,FS,hx );


```

```
    dF = vertcat(dFS,dFN);
end
```

D.3 hhTOss_s.m

keywordstyle

```
function output = hhTOss_s( Chp,x,r )
% 2-2 collision term from Higgs to scalar for the scalar distribution.
% Returns dim(x)-dim(r).

    output = Chp.*(exp(-sqrt(x'.^2+r.^2))./sqrt(x'.^2+r.^2)).*r.*besselk(1,r);

end
```

D.4 ssTOhh_s.m

keywordstyle

```
function output = ssTOhh_s( Chp,x,r,FS,hx )
% 2-2 collision term from scalar to Higgs for the scalar distribution.
% Returns dim(x)-dim(r).
%   FS should be dim(x)-dim(r)
%   x should be 1-dim(x)
    xp_integral = hx.*sum((log(10).*x'.*x'.^2.*FS)./sqrt(x'.^2+r.^2));
    output = -Chp.*(1./sqrt(x'.^2+r.^2)).*FS.*xp_integral;

end
```

D.5 sTOnn_s.m

keywordstyle

```
function output = sTOnn_s( Cg,x,r,FS )
% 1-2 collision term from scalar to neutrinos for the scalar distribution.
% Returns dim(x)-dim(r).
%   FS must be dim(x)-dim(r).
%   x must be 1-dim(x).
%   r assumed scalar.

    output = -Cg.*FS*r.^2./sqrt(x'.^2+r.^2);
end
```

D.6 sTOnn_n.m

keywordstyle

```
function output = sTOnn_n( Cg,x,r,FS,hx )
% 1-2 collision term from scalar to neutrinos for the neutrino distribution.
% Returns dim(x)-dim(r).
%   FS must be dim(x)-dim(r).
%   x must be 1-dim(x).
%   r assumed scalar.
    xp=x;
                                            % dimensions of this line V
    root = abs( (2.*x.*sqrt(xp'.^2+r.^2)-r.^2)./(2.*x.*xp') ); %xp-x
    theta = heaviside(1-root); %xp-x
    outer = r.^2./x.^2; % 1-x
    integrand = FS.*log(10).*x'.*x'./sqrt(x'.^2+r.^2); %xp-1
    inner = integrand.*theta; % xp-x
    inner = hx.*sum(inner,1); % 1-x

    output = 2.*Cg.*outer.*inner;
    output = output';
end
```

Bibliography

[1] S. M. Carroll. *Spacetime and Geometry: An introduction to general relativity.* Addison Wesley, 2004.

[2] D. H. Lyth, A. R. Liddle. *The primordial density perturbation: Cosmology, inflation and the origin of structure.* Cambridge university press, 2009.

[3] E. W. Kolb, M. S. Turner. *The early universe.* Addison-Wesley, 1993.

[4] **Planck Collaboration:** P. A. R. Ade et al. *Planck 2015 results. XIII. Cosmological parameters.* Astron. Astrophys **594** (2016) A13, arXiv:1502.01589.

[5] **The LIGO Scientific Collaboration and the Virgo Collaboration et al.** *A gravitational-wave standard siren measurement of the Hubble constant.* Nature **551:7678** (2017) 85-88, arXiv:1710.05835.

[6] A. Riess et al. *A 2.4% determination of the local value of the Hubble constant.* The Astrophys. J. **826** (2016) 56, arXiv:1604.01424.

[7] N. Tamanini. *Standard sirens: cosmology with gravitational waves.* HIP cosmology seminar, 30.11.2017. Available at HIP archives: link.

[8] G. Bertone, D. Hooper. *A History of Dark Matter.* FERMILAB-PUB-16-157-A arXiv:1605.04909.

[9] **Particle Data Group:** C. Patrignani et al. *Review of particle physics.* Chin. Phys. C. (2016) **40**, 100001.

[10] M. E. Peskin, D. V. Schroeder. *An introduction to quantum field theory.* Westview Press, 1995.

[11] K. G. Begeman, A. H. Broeils and R. H Sanders. *Extended rotation curves of spiral galaxies: dark haloes and modified dynamics.* Mon. Not. R. ast. Soc. (1991) **249**, 523-537.

[12] R. Narayan, M. Bartelmann. *Lectures on Gravitational Lensing.* 13th Jerusalem Winter School in Theoretical Physics, arXiv:astro-ph/9606001.

[13] R. S. Ellis. *Gravitational lensing: a unique probe of dark matter and dark energy.* Phil. Trans. R. Soc. A **368** (2010) 967-987.

[14] M. Bartelmann. *Gravitational lensing.* Class. Quantum Grav. **27** (2010) 23, arXiv:1010.3829.

[15] D. Clowe, M. Bradac, A. H. Gonzalez, M. Markevitch, S. W. Randall, C. Jones, D. Zaritsky. *A direct empirical proof of the existence of dark matter.* The Astrophys. J. **648** (2006) L109-L113, arXiv:astro-ph/0608407.

[16] B. Moore, S. Ghigna, F. Governato, G. Lake, T. Quinn, J. Stadel, P. Tozzi. *Dark matter substructure in galactic halos.* The Astrophys. J. **524** (1999) L19-L22, arXiv:astro-ph/9907411.

[17] A. A. Klypin, A. V. Kravtsov, O. Valenzuela, F. Prada. *Where are the missing galactic satellites?* The Astrophys. J. **522** (1999) 82-92, arXiv:astro-ph/9901240.

[18] L. E. Strigari, J. S. Bullock, M. Kaplinghat, J. Diemand, M. Kuhlen, P. Madau. *Redefining the Missing satellites problem.* The Astrophys. J. *669* (2007) 676-683, arXiv:0704.1817.

[19] **The DES Collaboration:** A. Drlica-Wagner et al. *Eight ultra-faint galaxy candidates discovered in year two of the dark energy survey.* The Astrophys. J. **813**, (2015) 109, arXiv:1508.03622.

[20] S. Y. Kim, A. H. G. Peter, J. R. Hargis. *There is no missing satellites problem.* arXiv:1711.06267.

[21] A. M. Brooks, M. Kuhlen, A. Zolotov, D. Hooper. *A baryonic solution to the missing satellites problem.* The Astrophy. J. **765** (2013) 22, arXiv:1209.5394.

[22] A. Fattahi, J. F. Navarro, T. Sawala, C. S. Frenk, L. V. Sales, K. Oman, M. Schaller, J. Wang. *The cold dark matter content of Galactic dwarf spheroidals: no cores, no failures, no problem.* arXiv:1607.06479.

[23] M. Boylan-Kolchin, J. S. Bullock, M. Kaplinghat. *Too big to fail? The puzzling darkness of massive Milky Way subhaloes.* Mon. Not. Roy. Astron. Soc. **415** (2011) L40, arXiv:1103.0007.

[24] E. Papastergis, R. Giovanelli, M. P. Haynes, F. Shankar. *Is there a "too big to fail" problem in the field?* A&A **547** (2015) A113, arXiv:1407.4665.

[25] M. Boylan-Kolchin, J. S. Bullock, M. Kaplinghat. *The Milky Way's bright satellites as an apparent failure of LCDM.* Mon. Not. Roy. Astron. Soc. **422** (2012) 1203-1218, arXiv:1111.2048.

[26] M. R. Lovell, V. Eke, C. S. Frenk, L. Gao, A. Jenkins, T. Theuns, J. Wang, S. D. M. White, A. Boyarsky, O. Ruchayskiy. *The haloes of bring satellite galaxies in a warm dark matter universe.* Mon. Not. Roy. Astron. Soc. **420** (2012) 2318-2324, arXiv:1104.2929.

[27] M. R. Lovell, V. Gonzalez-Perez, S. Bose, A. Boyarsky, S. Cole, C. S. Frenk, O. Ruchayskiy. *Addressing the too big to fail problem with baryon physics and sterile neutrino dark matter.* Mon. Not. Roy. Astron. Soc. **468** (2017) 2836-2849, arXiv:1611.00005.

[28] R. A. Flores, J. R. Primack *Observational and theoretical constraints on singular dark matter halos.* Astrophys. J. **427** (1994) L1-L4

[29] J. F. Navarro, V. R. Eke, C. S. Frenk. *The cores of dwarf galaxy haloes.* Mon. Not. Roy. Astron. Soc. **283** (1996) L72-L78, arXiv:astro-ph/9610187.

[30] J. F. Navarro, C. S. Frenk, S. D. M. White. *A universal density profile from hierarchical clustering.* Astrophys. J. **490** (1997) 493-508, arXiv:astro-ph/961107.

[31] W. J. G. de Blok. *The core-cusp problem.* Advances in Astronomy, **vol. 2010** (2010), Article ID 789293, arXiv:0910.3538.

[32] A. Pontzen, F. Governato. *How supernova feedback turns dark matter cusps into cores.* Mon. Not. Roy. Astron. Soc. **421** (2012) 3464-3471, arXiv:1106.0499.

[33] F. Governato, A. Zolotov, A. Pontzen, C. Christensen, S. H. Oh, A. M. Brooks, T. Quinn, S. Shen, J. Wadsley. *Cuspy no more: how outflows affect the central dark matter and baryon distribution in Lambda CDM galaxies.* Mon. Not. Roy. Astron. Soc. **422** (2012) 1231-1240, arXiv:1202.0554.

[34] A. Loeb, N. Weiner. *Cores in dwarf galaxies from dark matter with a Yukawa potential.* Phys. Re. Lett. **106** (2011) 171302, arXiv:1011.6374.

[35] D. N. Spergel, P. J. Steinhardt. *Observational evidence for self-interacting cold dark matter.* Phys. Rev. Lett. *84* (2000) 3760-3763, arXiv:astro-ph/9909386.

[36] S. Tulin. H-B Yu. *Dark matter self-interactions and small scale structure.* arXiv:1705.02358.

[37] F. Villaescusa-Navarro, N. Dalal. *Cores and cusps in warm dark matter halos.* JCAP 03 (2011) 024, arXiv:1010.3008.

[38] D. H. Weinberg, J. S. Bullock, F. Governato, R. Kuzio de Naray, A. H. G. Peter. *Cold dark matter: Controversies on small scales.* Proc. Natl. Acad. Sci. USA (2015) 112(40): 12249-12255, arXiv:1306.0913.

[39] G. W. Angus, S. S. McGaugh. *The collision velocity of the bullet cluster in conventional and modified dynamics.* Mon. Not. Roy. Astron. Soc. **383** (2007) 417-423, arXiv:0704.0381.

[40] V. Springel, G. Farrar. *The speed of the 'bullet' in the merging galaxy cluster 1E0657-56.* Mon. Not. Roy. Astron. Soc. **380** (2007) 911-925, arXiv:astro-ph/0703232.

[41] J. Lee, E. Komatsu. *Buller cluster: a challenge to LCDM cosmology.* APJ **718** (2010) 60-65, arXiv:1003.0939.

[42] R. Thompson, K. Nagamine. *Pairwise velocities of dark matter halos: a test for the Lambda Cold Dark Matter model using the bullet cluster.* Mon. Not. Roy. Astron. Soc. **419** (2012) 3560-3570, arXiv:1107.4645.

[43] D. Kraljic, S. Sarkar. *How rare is the bullet cluster (in a ΛCDM universe)?* JCAP 04 (2015) 050, arXiv:1412.7719.

[44] R. Thompson, R. Davé, K. Nagamine. *The rise and fall of a challenger: the bullet cluster in Λ Cold Dark Matter simulations.* Mon. Not. Roy. Astron. Soc. **452** (2015) 3030-3037, arXiv:1410.7438.

[45] S. M. Molnar, T. Broadhurst. *Multi-phenomena modeling of the new bullet cluster, ZwCI008.8+52, using N-body/hydrodynamical simulations.* Submitted to the APJ (2017), arXiv:1712.06887.

[46] R. Thompson, R. Davé, S. Huang, N. Katz. *Identifying mergers using non-parametric morphological classification at high redshifts.* arXiv:1508.01851.

[47] C. Zhang, Q. Yu, Y. Lu. *Simulating the galaxy cluster "El Gordo" and identifying the merger configuration.* APJ **813** (2015) 129, arXiv:1511.02578.

[48] P. Behroozi, A. Knebe, F. R. Pearce, P. Elahi, J. Han. H. Lux, Y.-Y. Mao, S. I. Muldrew, D. Potter, C. Srisawat. *Major mergers going notts: challenges for modern halo finders.* Mon. Not. Roy. Astron. Soc. **454** (2015) 3020-3029, arXiv:1506.01405.

[49] M. de los Rios, R. Domínguez, J. Mariano, D. Paz, M. Merchán. *The MeSsI (Merging Systems Identification) algorithm & catalogue.* Mon. Not. Roy. Astron. Soc. **458** (2016) 226-232, 1509.02524.

[50] S. Y. Kim, A. H. G. Peter, D. Wittman. *In the wake of dark giants: new signatures of dark matter self interactions in equal mass mergers of galaxy clusters.* Mon. Not. Roy. Astron. Soc. **469** (2017) 1414-1444, arXiv:1608.08630.

[51] N. Bernal, M. Heikinheimo, T. Tenkanen, K. Tuominen, V. Vaskonen. *The dawn of FIMP dark matter: a review of models and constraints.* Int. J. Mod. Phys. **A32** (2017) 1730023, arXiv:1706.07442.

[52] K. Petraki, R. R. Volkas. *Review of asymmetric dark matter.* Int. J. Mod. Phys. **A28** (2013) 1330028, arXiv:1305.4939.

[53] K. M. Zurek. *Asymmetric dark matter: theories, signatures, and constraints.* Phys. Rept. **537** (2014) 91-121, arXiv:1308.0338.

[54] I. Baldes, M. Cirelli, P. Panci, K. Petraki, F. Sala, M. Taoso. *Asymmetric dark matter: residual annihilations and self-interactions.* CERN-TH-2017-272; DESY 17-232, arXiv:1712.07489.

[55] E. D. Carlson, M. E. Machacek, L. J. Hall. *Self-interacting dark matter.* Astrophys. J. **398** (1992) 43-52.

[56] Y. Hochberg, E. Kuflik, T. Volansky, J. G. Wacker. *Mechanism for thermal relic dark matter of strongly interacting massive particles.* Phys. Rev. Lett. **113** (2014) 171301, arXiv:1402.5143.

[57] D. Pappadopulo, J. T. Ruderman, G. Trevisa. *Dark matter freeze-out in a nonrelativistic sector.* Phys. Rev. **D94** (2016) 035005, arXiv:1602.04219.

[58] M. Farina, D. Pappadopulo, J. T. Ruderman, G. Trevisan. *Phases of cannibal dark matter.* JHEP **12** (2016) 039, arXiv:1607.03108.

[59] P. Gondolo, G. Gelmini. *Cosmic abundances of stable particles: improved analysis.* Nucl. Phys. **B360** (1991) 145-179.

[60] K. Griest, D. Seckel. *Three exceptions in the calculation of relic abundances.* Phys. Rev. **D43** (1991) 3191-3203.

[61] J. Edsjö, P. Gondolo. *Neutralino relic density including coannihilations.* Phys. Rev. **D56** (1997) 1879-1894, arXiv:hep-ph/9704361.

[62] T. Hambye. *Hidden vector dark matter.* JHEP **01** (2009) 028, arXiv:0811.0172.

[63] F. D'Eramo, J. Thaler. *Semi-annihilation of dark matter.* JHEP **06** (2010) 109, arXiv:1003.5912.

[64] G. Belanger, K. Kannike, A. Pukhov, M. Raidal. *Impact of semi-annihilations on dark matter phenomenology – an example of $\mathbb{Z}_N$ symmetric scalar dark matter.* JCAP **1204** (2012) 010, arXiv:1202.2962.

[65] R. T. D'Agnolo, D. Pappadopulo, J. T. Ruderman. *A fourth exception in the calculation of relic abundances.* Phys. Rev. Lett. **119** (2017) 061102, arXiv:1705.08450.

[66] K. Enqvist, K. Kainulainen, I. Vilja. *Phase transitions in the singlet majoron model.* Nucl. Phys. **B403** (1993) 749-769.

[67] K. Enqvist, S. Nurmi, T. Tenkanen, K. Tuominen. *Standard Model with a real singlet scalar and inflation.* JCAP **1408** (2014) 035, arXiv:1407.0659.

[68] J. McDonald. *Thermally generated gauge singlet scalar as self-interacting dark matter.* Phys. Rev. Lett. **88** (2002) 091304, arXiv:hep-ph/0106249.

[69] L. J. Hall, K. Jedamzik, J. March-Russell, S. M. West. *Freeze-in production of FIMP dark matter.* JHEP **1003** (2010) 080, arXiv:0911.1120.

[70] M. Heikinheimo, T. Tenkanen, K. Tuominen, V. Vaskonen. *Observational constraints on decoupled hidden sectors.* Phys. Rev. **D94** (2016) 109902,arXiv:1604.02401.

[71] A. Merle, M. Totzauer. *keV sterile neutrino dark matter from singlet scalar decays: basic concepts and subtle features.* JCAP **06** (2015) 011, arXiv:1502.01011.

[72] J. König, A. Merle, M. Totzauer. *keV sterile neutrino dark matter from singlet scalar decays: the most general case.* JCAP **11** (2016) 038, arXiv:1609.01289.

[73] P. Langacker. *On the cosmological production of light sterile-neutrinos.* Report-No.: UPR-0401T (1989).

[74] K. Kainulainen. *Light singlet neutrinos and the primordial Nucleosynthesis.* Phys. Lett. **B244** (1990) 191-195.

[75] R. Barbieri, A. Dolgov. *Bounds on sterile-neutrinos from nucleosynthesis.* Phys. Lett. **B237** (1990) 440.

[76] S. Dodelson, L. M. Widrow. *Sterile neutrinos as dark matter.* Phys. Rev. Lett. **72** (1994) 17-20, arXiv:hep-ph/9303287.

[77] A. Merle, A. Schneider, M. Totzauer. *Dodelson-Widrow production of sterile neutrino dark matter with non-trivial initial abundance.* JCAP **1604** (2016) 003, arXiv:1512.05369.

[78] K. Enqvist, K. Kainulainen, J. Maalampi. *Resonant neutrino transitions and nucleosythesis.* Phys. Lett. **B249** (1990) 531-534.

[79] C.-D. Shi, G. M. Fuller. *A new dark matter candidate: nonthermal sterile neutrinos.* Phys. Rev. Lett. **82** (1999) 2832-2835, arXiv:astro-ph/9810076.

[80] M. Drewes et al. *A white paper on keV sterile neutrino dark matter.* JCAP **1701** (2017) 025, arXiv:1602.04816.

[81] **WMAP Collaboration:** E. Komatsu et. al. *Seven-year Wilkinson microwave anisotropy probe (WMAP) observations: cosmological interpretation.* J. Suppl. **192** (2011) 18, arXiv:1001.4538.

[82] K. Petraki, A. Kusenko. *Dark-matter sterile neutrinos in models with a gauge singlet in the Higgs sector.* Phys. Rev. **D77** (2008) 065014, arXiv:0711.4646.

[83] A. Merle, V. Niro, D. Schmidt. *New production mechanism for keV sterile neutrino dark matter by decays of frozen-in scalars.* JCAP **1403** (2014) 028, arXiv:1306.3996.

[84] A. Adulpravitchai, M. A. Schmidt. *A fresh look at keV sterile neutrino dark matter from frozen-in scalars.* JHEP **1501** (2015) 006, arXiv:1409.4330.

[85] S. Tremaine, J. E. Gunn. *Dynamical role of light neutral leptons in cosmology.* Phys. Rev. Lett. **42** (1979) 407-410.

[86] A. Boyarsky, O. Ruchayskiy, D. Iakubovskyi. *A lower bound on the mass of dark matter particles.* JCAP **03** (2009) 005, arXiv:0808.3902.

[87] A. Boyarsky, J. Lesgourgues, O. Ruchayskiy, M. Viel. *Lyman-alpha constraints on warm and on warm-plus-cold dark matter models.* JCAP **05** (2009) 012, arXiv:0812.0010.

[88] T. Robens, T. Steganiak. *Status of the Higgs singlet extension of the standard model after LHC run 1.* EPJC **75** (2015) 105, arXiv:1501.02234.

[89] G. Mangano, G. Miele, S. Pastor, T. Pinto, O. Pisanti, P. D. Serpico. *Relic neutrino decoupling including flavour oscillations-* Nucl. Phys. **B729** (2005) 221-234, arXiv:https://arxiv.org/abs/hep-ph/0506164.

[90] G. Mangano, P. D. Serpico. *A robust upper limit on N_eff from BBN, circa 2011.* Phys. Lett. **701** (2011) 296-299, arXiv:1103.1261.

[91] Y. I. Izotov, T. X. Thuan, N. G. Guseva. *A new determination of the primordial He abundance using the HeI 10830A emission line: cosmological implications.* Mon. Not. Roy. Astron. Soc. **445** (2014) 778-793, arXiv:1408.6953.

[92] B. M. Roberts et al. *Search for domain wall dark matter with atomic clocks on board global positioning system satellites.* Nature Communications **8** (2017) 1195, arXiv:1704.06844.

[93] R. Cooke, M. Pettini, R. A. Jorgenson, M. T. Murphy, C. C. Steidel. *Precision measures of the primordial abundance of deuterium.* Astrophys. J. **781** (2014) 31, arXiv:1308.3240.

[94] K. Markovič, M. Viel. *Lyman-α forest and cosmic weak lensing in a warm dark matter universe.* Publ. Astron. Soc. Aust. **31** (2014) e006, arXiv:1311.5223.

[95] V. Iršič et al. *New constraints on the free-streaming of warm dark matter from intermediate and small scale Lyman-α forest data.* Phys. Rev. **D 96** (2017) 023522, arXiv:1702.01764.

[96] P. Colin, V. Avila-Reese, O. Valenzuela. *Substructure and halo density profiles in a warm dark matter cosmology.* ApJ **542** (2000) 622-630, arXiv:astro-ph/0004115.

[97] A. Merle, A. Schneider. *Production of sterile neutrino dark matter and the 3.5 keV line.* Phys. Lett. **749** (2015) 283-288, arXiv:1409.6311.

[98] Cosmology lecture notes by Daniel Baumann: `http://www.damtp.cam.ac.uk/user/db275/Cosmology/Lectures.pdf`

[99] L. F. Shampine, M. W. Reichelt. *The MATLAB ODE suite.* SIAM J. Sci. Comput. **18** (1997) 1-22, MathWorks documentation.

[100] T. Asaka, S. Blanchet, M. Shaposhnikov. *The νMSM, dark matter and neutrino masses.* Phys. Lett. **B631** (2005) 151-156, arXiv:0503065.

[101] T. Asaka, M. Shaposhnikov. *The νMSM, dark matter and baryon asymmetry of the universe.* Phys. Lett. **B620** (2005) 17-26, arXiv:0505013.

[102] A. Boyarsky, O. Ruchayskiy, M. Shaposhnikov. *The role of sterile neutrinos in cosmology and astrophysics.* Ann. Rev. Nucl. Part. Sci. **59** (2009) 191-214, arXiv:0901.0011.

[103] K. Allison. *Dark matter, singlet extensions of the nuMSM, and symmetries.* JHEP **05** (2013) 009, arXiv:1210.6852.

[104] T. Alanne, A. Meroni, K. Tuominen. *Neutrino mass generation and leptogenesis via pseudo-Nambu-Goldstone Higgs portal.* Phys. Rev. **D96** (2017) 095015, arXiv:1706.10128.